

ALLOY DESIGN FOR THE DEVELOPMENT AND PRODUCTION OF
TITANIUM BASED BULK METALLIC GLASSES

A THESIS SUBMITTED TO
THE GRADUATE SCHOOL OF NATURAL AND APPLIED SCIENCES
OF
MIDDLE EAST TECHNICAL UNIVERSITY

BY

IRAZ BEGÜM DEMİR

IN PARTIAL FULFILLMENT OF THE REQUIREMENTS
FOR
THE DEGREE OF MASTER OF SCIENCE
IN
METALLURGICAL AND MATERIALS ENGINEERING

JULY 2019

Approval of the thesis:

**ALLOY DESIGN FOR THE DEVELOPMENT AND PRODUCTION OF
TITANIUM BASED BULK METALLIC GLASSES**

submitted by **IRAZ BEGÜM DEMİR** in partial fulfillment of the requirements for the degree of **Master of Science in Metallurgical and Materials Engineering Department, Middle East Technical University** by,

Prof. Dr. Halil Kalıpçılar
Dean, Graduate School of **Natural and Applied Sciences**

Prof. Dr. Hakan Gür
Head of Department, **Met. and Mat. Eng.**

Prof. Dr. Vedat Akdeniz
Supervisor, **Met. and Mat. Eng., METU**

Prof. Dr. Amdulla Mekhrabov
Co-Supervisor, **Met. And Mat. Eng, METU**

Examining Committee Members:

Prof. Dr. Ali Kalkanlı
Met. And Mat. Eng, METU

Prof. Dr. Vedat Akdeniz
Met. and Mat. Eng., METU

Prof. Dr. Amdulla Mekhrabov
Met. And Mat. Eng, METU

Assist. Prof. Dr. Simge Çınar
Met. And Mat. Eng, METU

Assist. Prof. Dr. Mehmet Yıldırım
Met. And Mat. Eng, KTUN

Date: 10.07.2019

I hereby declare that all information in this document has been obtained and presented in accordance with academic rules and ethical conduct. I also declare that, as required by these rules and conduct, I have fully cited and referenced all material and results that are not original to this work.

Name, Surname: Iraz Begüm Demir

Signature:

ABSTRACT

ALLOY DESIGN FOR THE DEVELOPMENT AND PRODUCTION OF TITANIUM BASED BULK METALLIC GLASSES

Demir, Iraz Begüm
Master of Science, Metallurgical and Materials Engineering
Supervisor: Prof. Dr. Vedat Akdeniz
Co-Supervisor: Prof. Dr. Amdulla Mekhrabov

July 2019, 83 pages

The bulk metallic glasses (BMGs) are quite new type of metallic alloys exhibiting many superior features like high yield strength, improved elastic behavior, high corrosion resistance and superior abrasion resistance by virtue of its irregular atomic structures. Due to the importance of today's reduced energy consumption, special attention is given to the light element-based bulk metallic glasses. Among these, Ti-based amorphous alloys have promising mechanical properties for use in engineering applications. Therefore, Ti-based bulk metallic glasses provides a hope as an advanced set of lightweight materials for use in medical applications, defense, automotive and aerospace industries. However, generally Ti-based bulk metallic glasses show poor bulk glass formation that restricts their potential application areas. Studies on this subject will provide an important involvement for the development of glass formation of the Ti based BMGs.

In the literature, there are many studies on theoretical and semi-empirical criteria for evaluation of glass forming ability (GFA) of the alloy systems. However, these criteria do not work on every alloy system while providing positive results for some system. Therefore, it is essential to systematically examine the effects of alloying elements for the development of cast metallic glass alloy systems.

In this thesis study, besides semi-empirical criteria, with the aim of improvement of the GFA, alloys were synthesized by alloying Ti-Cu binary system with potential candidate alloying elements derived from theoretical predictions by combining the electronic theory of alloys in the pseudopotential approximation which are the part of previous thesis study. As a starting point, Ni, Al and V were selected as alloying elements and correspondingly $\text{Ti}_{48}\text{Cu}_{30}\text{Ni}_{10}\text{Al}_7\text{V}_5$ alloy was produced. After that gradual Si addition was provided on this alloy and $\text{Ti}_{47}\text{Cu}_{30}\text{Ni}_{10}\text{Al}_7\text{V}_5\text{Si}_1$ and $(\text{Ti}_{48}\text{Cu}_{30}\text{Ni}_{10}\text{Al}_7\text{V}_5)_{97}\text{Si}_3$ alloys were fabricated to investigate effect of Si as a minor alloying element.

Samples of alloys were fabricated by arc melting device equipped with suction casting unit under controlled atmosphere. The effect of the potential alloying elements on the ability to create Ti based BMG was presented by structural and thermal characterization techniques. Atomic 1% of Si addition favored the formation of approximately 40 μm in thickness amorphous structure at the outer zone of the alloy composition $\text{Ti}_{47}\text{Cu}_{30}\text{Ni}_{10}\text{Al}_7\text{V}_5\text{Si}_1$. Further addition of Si has detrimental effects on glass formation ability. Even at non-equilibrium cooling condition amorphous structure was not observed and the crystallization could not be prevented by copper mold suction casting. .

Keywords: Ti based BMG, BGFA, Copper mold suction casting

ÖZ

TİTANYUM ESASLI HACİMLİ METALİK CAMLARIN GELİŞTİRİLMESİ VE ÜRETİMİ İÇİN ALAŞIM TASARIMI

Demir, Iraz Begüm
Yüksek Lisans, Metalurji ve Malzeme Mühendisliği
Tez Danışmanı: Prof. Dr. Vedat Akdeniz
Ortak Tez Danışmanı: Prof. Dr. Amdulla Mekhrabov

Temmuz 2019, 83 sayfa

Hacimli metalik camlar düzensiz atomik yapıları sayesinde yüksek akma dayanımı, gelişmiş elastik davranış, yüksek korozyon dayanımı ve üstün aşınma direnci gibi birçok benzersiz özelliğe sahip nispeten yeni bir metalik alaşım türüdür. Günümüzde enerji tüketiminin azaltılmasının önemi nedeniyle hafif element esaslı hacimli metalik camlara özel ilgi gösterilmektedir. Bunların arasında, yalnızca Ti esaslı alaşım sistemleri şu anda yapısal mühendislik uygulamalarında kullanılacak gerekli tokluğu göstermektedir. Bu nedenle, Ti esaslı hacimli metalik camlar; tıbbi uygulamalar, savunma, otomotiv ve havacılık endüstrilerinde kullanılmak üzere yeni hafif malzemeler sınıfı olarak umut vermektedir. Fakat bununla birlikte, Ti esaslı metalik camların çoğu, potansiyel uygulama alanlarını kısıtlayan zayıf hacimli metalik cam oluşturma kabiliyetine sahiptir ve bu konuda yapılacak çalışmalar bu alaşımların cam oluşturma kabiliyetlerinin geliştirilmesinde önemli katkılar sunacaktır.

Literatürde çok bileşenli alaşım sistemlerinin hacimli metalik cam oluşturma kabiliyetini değerlendirmek için bir takım yarı-ampirik ve teorik kriterler önerilmiştir. Fakat bu kriterler bazı sistemler için olumlu sonuçlar verirken bazı sistemlerde işe yaramamaktadır. Bu nedenle hacimli metalik cam alaşım sistemlerinin

geliştirilebilmesi için teorik hesaplamalardan yola çıkarak sistematik bir şekilde alaşım elementlerinin etkisinin incelenmesi şarttır.

Bu tez çalışması kapsamında yarı ampirik kriterlerin yanı sıra, daha önce yapılmış çalışmada yer alan, elektronik alaşım teorisinin psödopoterik yaklaşımda birleştirilmesiyle teorik olarak hesaplanmış kritik soğuma hızı ve karışım entalpisi verilerine dayanan hesaplamalar kullanılmıştır. Bu hesaplamalara göre cam yapma kabiliyetini arttırabileceği düşünülen aday alaşım elementlerinden Ni, Al, V ve Si'nin etkisinin incelenmesine karar verilmiştir. Bu kapsamda Ti-Cu ikili sistemine dayanan üç kompozisyon $Ti_{48}Cu_{30}Ni_{10}Al_7V_5$, $Ti_{47}Cu_{30}Ni_{10}Al_7V_5Si_1$ ve $(Ti_{48}Cu_{30}Ni_{10}Al_7V_5)_{97}Si_3$ olarak belirlemiştir

Alaşımalar kontrollü atmosfer altında emme döküm ünitesi ile donatılmış ark eritme ile üretilmiştir. Hacimli metalik cam oluşturma kabiliyeti üzerindeki potansiyel alaşım elementlerinin etkisi ve Ti-Cu ikili sistemi esas alınarak yapısal ve termal karakterizasyon teknikleri ile sunulmuştur. Atomik %1 Si ilavesi yaklaşık 40µm kalınlığında amorf fazın oluşmasını sağlamıştır. Artan Si ilavesi cam oluşturma kabiliyeti üzerinde olumsuz sonuçlar verdi. .

Anahtar Kelimeler: Ti esaslı hacimli camlar, hacimli cam oluşturma kabiliyeti, Bakır kalıba döküm

To My Dreams

ACKNOWLEDGMENTS

First and foremost, I would like to express my sincere appreciation and gratitude to my supervisors Prof. Dr. M. Vedat Akdeniz and Prof. Dr. Amdulla O. Mekhrabov for their guidance, wisdom, suggestions and endless understanding in preparation of this thesis.

Additionally, I would like to thank all my research group NOVALAB (Novel Alloys Design and Development Laboratory) mates, especially to Ali Fırat Dinler who never hesitate to share his time and knowledge with me. I also thank to Yusuf Yıldırım, Serkan Yılmaz, and Nilüfer Özel for their continuous help and understanding.

Finally, I am also grateful to my family for their patience and endless belief on me.

TABLE OF CONTENTS

ABSTRACT	v
ÖZ	vii
ACKNOWLEDGMENTS	x
TABLE OF CONTENTS	xi
LIST OF TABLES	xiv
LIST OF FIGURES	xv
CHAPTERS	
CHAPTER 1	1
1. INTRODUCTION	1
1.1. Aim and Motivation	1
CHAPTER 2	3
2. THEORETICAL REVIEW	3
2.1. Review on the Bulk Metallic Glasses.....	3
2.1.1. Historical Background	3
2.1.2. BMG's Properties and Applications	6
2.1.2.1. Mechanical Properties	6
2.1.2.2. Magnetic Properties	7
2.1.2.3. Formability	8
2.1.2.4. Corrosion Resistance.....	9
2.1.3. Origins of Glass Formation.....	11
2.1.3.1. Glass Formation in Thermodynamics Point of View.....	13
2.1.3.2. Glass Formation in Kinetics Point of View	14

2.1.3.3. Glass Formation in The Atomistic Point of View	15
2.1.4. Glass Forming Ability and Related Criteria for the Scope of This Thesis	16
2.1.4.1. Critical Cooling Rate (R_c).....	17
2.1.4.2. Inoue’s Empirical Rules	18
2.1.4.3. Reduced Glass transition Temperature (T_{rg}).....	20
2.1.4.4. Alloy Systems with Deep Eutectic	20
2.1.4.5. Solidification Behavior	21
2.2. Review on the Ti Based Bulk Metallic Glasses	22
2.2.1. Properties and Applications of Ti Based Bulk Metallic Glasses.....	25
2.3. Alloy Design of Ti-Based Bulk Metallic Glasses by Theoretical Study	29
2.3.1. Brief Explanation of Theory.....	29
CHAPTER 3	37
3. EXPERIMENTAL PROCEDURE	37
3.1. Raw Materials	37
3.2. Production of Alloys with Arc Melting	38
3.3. Metallographic Preparation.....	39
3.4. X-Ray Diffractometry	39
3.5. Scanning Electron Microscopy	39
3.6. Differential Scanning Calorimetry.....	40
3.7. Microhardness Measurement	40
CHAPTER 4	41
4. RESULTS AND DISCUSSION	41
4.1. Selection of Alloy Compositions	41

4.2. Characterization of Alloy 1 (Ti ₄₈ Cu ₃₀ Ni ₁₀ Al ₇ V ₅).....	46
4.2.1. Slow Cooling Part of the Alloy 1.....	46
4.2.2. Fast Cooling Part of the Alloy 1.....	50
4.3. Characterization of Alloy 2 (Ti ₄₇ Cu ₃₀ Ni ₁₀ Al ₇ V ₅ Si ₁).....	54
4.3.1. Slow Cooling Part of the Alloy 2.....	54
4.3.2. Fast Cooling Part of the Alloy 2.....	57
4.4. Characterization of Alloy 3 (Ti ₄₈ Cu ₃₀ Ni ₁₀ Al ₇ V ₅) ₉₇ Si ₃	61
4.4.1. Slow Cooling Part of the Alloy 3.....	61
4.4.2. Fast Cooling Part of the Alloy 3.....	68
CHAPTER 5.....	75
5. CONCLUSIONS AND FUTURE SUGGESTIONS.....	75
5.1. Conclusions.....	75
5.2. Future Suggestions.....	76
6. REFERENCES.....	77

LIST OF TABLES

TABLES

Table 2.1 Non-ferromagnetic and ferromagnetic amorphous systems together with the years when the alloy system was found (Ln = lanthanide metal, Tm = transition metal)[11].	5
Table 2.2 Some of the application fields of BMGs and related properties [22]......	10
Table 2.3 Some of the previously found Ti-based BMG compositions until 2019... 23	
Table 2.4 σ_y : Yield strength; σ_{max} : ultimate strength; σ_c : specific strength (σ_y /density); E: Young’s modulus.	25
Table 2.5 Ordering energy and interchange energy values for $Ti_{64}Cu_{35}X_1$ alloy (in SI units)[94]......	34
Table 2.6 ΔH^M , S^σ , ΔS^{ideal} , ΔS^M , $\Delta\eta/\eta_0$ and critical cooling rate for $Ti_{64}Cu_{35}X_1$ alloy (in SI units) [94]......	35
Table 3.1 Form and purity levels of elements.	37
Table 4.1 Eutectic reaction parameters for Ti-Cu binary and Ti-Cu-Ni ternary systems.	41
Table 4.2 Calculated data of ΔH_{mix} and R_c [99].	43
Table 4.3 Atomic radii values of selected elements [100]......	44
Table 4.4 Codification of samples.	45
Table 4.5 EDS analysis for SC Alloy 1.	47
Table 4.6 EDS analysis for SC Alloy 2.	56
Table 4.7 EDS analysis for SC Alloy 3.	64
Table 4.8 EDS analysis for FC Alloy 3.	69

LIST OF FIGURES

FIGURES

Figure 2.1. Relationship between tensile strength, Vickers hardness (Hv) and E for various bulk amorphous alloys [15].	7
Figure 2.2 A comparison of I–H hysteresis loop of the cast ring-shape Fe-based BMG and similar ring-shape alloy made by stacking the melt-spun ribbons [17].	8
Figure 2.3 A La ₅₅ Al ₂₅ Ni ₂₀ alloy (1) before deformation, (2) after deformation to 20,000% in the supercooled liquid region [19].	9
Figure 2.4 Current density curves related with the potential for different Mg-based amorphous alloys and Mg and AZ31 recorded in borate buffer solution with pH 8.4 (sr = 0.5 mV/s) [21].	10
Figure 2.5 Specific volume change related with temperature for a crystalline and a glass-forming material.	11
Figure 2.6 XRD pattern and TEM images of Cu ₅₀ Zr ₅₀ amorphous alloy [23].	12
Figure 2.7 Schematic diagram of a typical nose-shaped temperature–time-transformation for a hypothetical melt [34].	17
Figure 2.8 Effect of alloying element addition on TTT diagram [35].	18
Figure 2.9 Schematic cause and effect relationship of three empirical rules to obtain glass formation [15].	19
Figure 2.10 Schematic phase diagram of an eutectic system [30].	21
Figure 2.11 Schematic melting DSC curve of a hypothetical binary alloy including a sequence of eutectic and peritectic reactions upon heating [29].	21
Figure 2.12 The Ashby diagram of strength versus density for engineering materials [91].	26
Figure 2.13 Compressive stress-strain curves of Ti-Zr-Be-Cu-Ni bulk metallic glasses [87].	27
Figure 2.14 Current density versus potential curves of BMG and the Ti–6Al–4V alloy in (a) PBS, (b) 0.9 wt % NaCl, (c) 1 mol/L HCl, and (d) 1 mol/L NaOH solutions [81].	28

Figure 3.1. Edmund Bühler arc melting device equipped with water cooled copper mold suction casting unit and the copper mold.	38
Figure 3.2 Setaram Setsys–16/18 DSC used in the thermal analysis measurements.	40
Figure 4.1 Ti-Cu binary phase diagram [95].	42
Figure 4.2 Vertical section of the ternary Ti-Cu-Ni phase diagram [98].	43
Figure 4.3 Sample produced with copper mold suction casting (a) slow cooling part, (b) fast cooling part.	45
Figure 4.4 Optical microscope images of SC Alloy 1 with different scales (a) 200 μm , (b) 100 μm , (c) 50 μm , (d) 20 μm	46
Figure 4.5 FESEM images of SC Alloy 1 in different magnifications (a) 1000x, (b) 2000x, (c) 16000x, (d) 100000x.	48
Figure 4.6 XRD pattern of SC Alloy 1.	49
Figure 4.7 DSC heating curve of SC Alloy 1.	49
Figure 4.8 Optical microscope image of the FC Alloy 1.	50
Figure 4.9 FESEM images of the FC Alloy 1, (a) center zone of the sample and (b) outer zone of the sample.	51
Figure 4.10 (a) Secondary-Electron image (SEI), (b) Backscattered-Electron (BSE) image of FC Alloy 1.	51
Figure 4.11 XRD pattern of FC Alloy 1.	52
Figure 4.12 Comparative XRD pattern of FC Alloy 1 and SC Alloy 1.	52
Figure 4.13 Comparative DSC heating curves for FC Alloy 1 and SC Alloy1.	53
Figure 4.14 Optical microscope images of SC Alloy 2 with different scales (a) 200 μm , (b) 100 μm , (c) 50 μm , (d) 20 μm	54
Figure 4.15 FESEM images of SC Alloy 2 in different magnifications (a) 4000x, (b) 8000x, (c) 16000x, (d) 120000x.	55
Figure 4.16 XRD pattern of SC Alloy 2.	56
Figure 4.17 Optical microscope image of FC Alloy 2.	57
Figure 4.18 FESEM images of FC Alloy 2, (a) center zone of the sample and (b) outer zone of the sample.	58
Figure 4.19 XRD pattern of FC Alloy 2.	59

Figure 4.20 Comparative XRD pattern of FC Alloy 2 and SC Alloy 2.....	59
Figure 4.21 DSC heating curves for FC Alloy 2.....	60
Figure 4.22 Optical microscope images of SC Alloy 3 with different scales (a) 100 μm , (b) 50 μm , (c) 20 μm , (d) 10 μm	61
Figure 4.23 Chinese script structures found in SC Alloy 3.	62
Figure 4.24 FESEM images of SC Alloy 3 in different magnifications (a) 50 μm , (b) 20 μm , (c) 5 μm , (d) 2 μm	63
Figure 4.25 Secondary-Electron image (SEI), (b) Backscattered-Electron (BSE) image of SC Alloy 3.	64
Figure 4.26 Ti-Cu-Si ternary phase diagram isothermal section at 800°C [103].	65
Figure 4.27 EDS mapping analysis of SC Alloy 3 showing elemental distribution of, (a) Ti, (b) Cu, (c) Ni, (d) Al, (e) V, and (f) Si.....	66
Figure 4.28 XRD pattern of SC Alloy 3.	67
Figure 4.29 Optical microscope image of FC Alloy 3.	68
Figure 4.30 FESEM images of FC Alloy 3.....	69
Figure 4.31 XRD pattern of FC Alloy 3.	70
Figure 4.32 Comparative XRD pattern of fast cooling part of the Alloy 3 and Slow cooling part of the Alloy 3.	70
Figure 4.33 DSC Heating Curves for FC Alloy 3.....	71
Figure 4.34 Comparative XRD patterns of fast cooling part of the Alloy 1, Alloy 2, and Alloy 3.....	72
Figure 4.35 Comparative DSC heating curves of FC Alloy 1, Alloy 2, and Alloy 3.....	72
Figure 4.36 Micro-Hardness Comparison of Alloys.....	73

CHAPTER 1

INTRODUCTION

1.1. Aim and Motivation

BMGs have received huge interest due to their exclusive features compared with their crystalline counterparts. These properties make them potentially desirable for various industries, including great elastic limits, relatively high yield strengths, high hardness, good corrosion resistance, and excellent biocompatibility. However, many of the developed BMG systems exist in Fe, Ni, Pd, Cu, and, Zr systems. Due to requirement of reduced energy consumption, low-density engineering materials such as Ti, Al, and Mg which show superior specific strength, are the most fundamental component of studies on materials science. Among all low-density BMG systems, Ti-based BMGs show promising features on account of their improved elastic modulus, elevated specific strength, relatively low-cost, good biocompatibility, and resistance to corrosion. However, Ti-based BMGs have a relatively low GFA that limits their potential usage areas. For this reason, studies on the development of GFA of Ti-based BMGs are necessary.

Regarding this requirement, this thesis intends to examine the effects of the candidate alloying elements on GFA of Ti-based BMGs. During the alloy design processes, besides the semi-empirical criteria, related GFA parameters which were calculated in the context of previous thesis study were used.

The stages of these study are listed below:

- Determination of possible Ti-based binary system to be alloyed with regards to semi-empirical rules
- Selection of candidate alloying element based on a literature review and using of theoretical calculations of glass formation parameters with regards to empirical rules
- Preparation of the samples by water-cooled copper mold suction casting
- Investigation of thermal and crystallization behavior of samples using differential scanning calorimetry (DSC) and investigation of structural properties using scanning electron microscope (SEM) and X-ray diffractometry (XRD).

CHAPTER 2

LITERATURE REVIEW

2.1. Review on the Bulk Metallic Glasses

2.1.1. Historical Background

The first amorphous metallic alloy was produced in 1960 and after that it was understood that a disordered atomic arrangement as in the liquid phase can be conserved if the metallic liquid is cooled down below the room temperature by using extremely high cooling rates at about 10^6 K s^{-1} . Consequently, $\text{Au}_{75}\text{Si}_{25}$, obtained by Duwez in 1960, was introduced into the literature as the first amorphous metallic alloy [1]. Since this discovery, numerous investigations on the properties, characterization, and production of metallic amorphous alloys were performed by applying rapid solidification on metallic liquids. After Duwez's pioneering work, ternary amorphous alloys were produced in Pd–Si– (Ag, Cu, Au) system [2]. Alloy composition of $\text{Pd}_{77.5}\text{Cu}_6\text{Si}_{16.5}$ could be produced with an amorphous structure of 0.5 mm in diameter of and the observable glass transition event. Also, in some ternary Pd–Si– (Ag, Cu, Au) alloys, the temperature range between the glass transition and first crystallization which referred to as the supercooled liquid range was found to extend up to 40 K. These Pd-based ternary systems allowed a detailed study of the crystallization behavior of amorphous metallic alloys. Additionally, systematic investigations on Pd– (Ni, Co, Fe)–P alloys were made in 1974 and an amorphous structure with the maximum castability thickness of 1 mm were able to obtained in this alloy system [3]. In 1982, $\text{Au}_{55}\text{Pb}_{22.5}\text{Sb}_{22.5}$ system was able to produce with an extended castability thickness [4]. Afterwards, Pd–Ni–P system was restudied by the Turnbull group in the 1980s and amorphous blocks with a diameter of 5mm in the alloy composition $\text{Pd}_{40}\text{Ni}_{40}\text{P}_{20}$ were achieved to fabricate. In 1984, critical casting thickness of this alloy

was extended to 1 cm in diameter by applying boron oxide flux to the liquid melt.[5].As a result, this 1 cm ternary alloy can be regarded as the first manufactured metallic glass system.

During the 1980s, glass forming ability of rare-earth elements with the addition of Al and Fe, Ni, Co metals were investigated by the Inoue's group. While studying in these systems with rapid solidification, outstanding GFA were found in the La–Al–Ni and La–Al–Cu alloy systems [6]. Production of the fully amorphous cylindrical samples with diameters of up to 5 mm were achieved by Cu mold casting of $\text{La}_{55}\text{Al}_{25}\text{Ni}_{20}$. In 1991, Mg–Cu–Y and Mg–Ni–Y systems were studied and the $\text{Mg}_{65}\text{Cu}_{25}\text{Y}_{10}$ alloy was developed having excellent glass-forming ability [7]. Meanwhile, a group of Zr-based Zr–Al–Ni–Cu alloys with a high thermal stability (liquid region ranged to 127 K) and good glass forming ability (critical casting thickness reached up to 15mm) were acquired by the Inoue's group [8].

Interest on bulk metallic glass increased after the improvements of these alloy systems and studies started by Johnson and Caltech for BMGs to be used in engineering applications. A quinary alloy ($\text{Zr}_{41.2}\text{Ti}_{13.8}\text{Cu}_{12.5}\text{Ni}_{10}\text{Be}_{22.5}$) with a maximum castability thickness of several centimeters, named as Vitreloy 1 (Vit1), was developed by Peker and Johnson in 1993 [9]. Production of the Vitreloy 1 can be considered as the initial point for the utilization of the bulk metallic glasses in structural applications. Thereafter, the $\text{Pd}_{40}\text{Ni}_{40}\text{P}_{20}$ alloy was reproduced with the addition 30% Cu instead of same percentage of Ni by the Inoue group. Development of the maximum castability thickness of this alloy up to 72mm was achieved as a result of this study [10]. This is the highest maximum castability thickness was obtained so far.

Table 2.1 *Non-ferromagnetic and ferromagnetic amorphous systems together with the years when the alloy system was found (Ln = lanthanide metal, Tm = transition metal)[11].*

1. Non-ferromagnetic alloy systems	Year	2. Ferromagnetic alloy systems	Year
Mg–Ln– (Zn, Cu, Ni)	1988	Fe– (Nb, Mo)–(Al, Ga)–(P, B, Si)	1995
Ln–Ga–Tm	1989	Fe– (Ga, Al) – (Ge, Si, B, C, Pb)	1995
Ln–Al– (Cu, Ni, Co, Fe)	1989	Co– (Ga, Al)– (Si, B, Pb)	1996
Zr–Al–Tm	1990	Fe– (Nb, Hf, Zr)–B	1996
Zr–Ln–Al–Tm	1992	Co– (Nb, Hf, Zr)–B	1996
Zr–Ti–Tm–Be	1993	Fe–Co–Ln–B	1998
Ti–Zr–Tm	1993	Fe–Ga– (Mo, Cr)–(B,C,P)	1999
Zr– (Pd, Nb, Ni)–Al–Tm	1995	Ni– (Mo, Cr, Nb)–(P, B)	1999
Pd–Ni–Fe–P	1996	Fe– (Mo, Cr)– (C, B)	1999
Pd–Cu–Ni–P	1996	Co–Ta–B	1999
Ti–Ni–Cu–Sn	1998	Fe–Ga–(B, P)	2000
Ca–Cu–Ag–Mg	2000	Ni–Zr–Ti–Sn–Si	2001
Cu– (Hf, Zr)–Ti	2001	Ni–(Ta, Nb)–Zr–Ti	2002
Cu–Zr, Cu–Hf	2001	Co–Fe–Si–B–Nb	2002
Cu– (Zr, Hf)–Al	2003	Fe–Si–B–Nb	2002
Ti–Cu– (Hf, Zr)– (Ni, Co)	2004	Co–Fe–Ta–B–Si	2003
Pt–Cu–Ni–P	2004	Ni–Nb–Sn	2003
Cu– (Hf, Zr)–Al– (Pd, Ag)	2004	Fe– (Mo, Cr)– (C, B)– (Tm, Er, Y)	2004
Au–Ag–Pd–Cu–Si	2005	Ni–Pd–P	2004
Cu– (Hf, Zr)–Ag	2005	Co– (Mo, Cr)–(B,C)– (Y, Tm)	2005
Ce–Cu–Al–Si–Fe	2005	Ni– (Ta, Nb)–Ti–Zr–Pd	2006
Zr–Cu–Al–Ag–Pd	2007	Fe–(Cr, Nb)–(Si, B, P)	2010
Ti–Zr–Cu–Pd–Sn	2007		
Ti–Zr–Cu–Pd	2007		

After these developments, most studies which relate to metallic glass changed towards producing alloys with the bulk dimensions usually larger than 1 mm in diameter. Until this time, lots of amorphous alloys have been discovered which could be produced as bulk forms. As a result, various commercial applications for bulk metallic glasses are available today, such as sporting goods, biomedical implants, springs, optical devices, and cell phone. After several faults in the bulk metallic glasses were located, researches were focused on the improvement mechanism of the mechanical properties. These researches fundamentally centered on the possible ways to alleviate the brittle nature of BMGs. This situation created a new research area as the bulk metallic glass matrix composites (BMGMCs), which is basically an amorphous matrix with the addition of crystalline phases in it [12].

2.1.2. BMG's Properties and Applications

Bulk metallic glasses (BMGs) mechanically and chemically offer exceptional features, such as lower elastic modulus, high yield strength, large elastic limit, advantageous wear and corrosion resistance related with their amorphous atomic structure. These properties hardly acquired in conventional crystalline systems. Therefore, BMGs are appealing as new a group of structural and functional materials.

2.1.2.1. Mechanical Properties

Because of the nonexistence of crystalline structure, the yield strength and hardness of the BMGs are much higher compared to the conventional metallic alloys by virtue of the absence of the crystalline defects such as dislocations and grain boundaries. For example yield strength can go up to 2 GPa for Cu-based BMGs [13] and so much as 6 GPa for Co-BMGs [14]. In addition, unlikely to the conventional oxide glasses, they are less brittle, and they have more elastic strain and fracture toughness. Figure 2.1 gives the tensile strength values relative to the Young's modulus for different bulk metallic glasses to compare them with the currently used crystalline alloys. It is evident from the figure that the BMGs have superior mechanical properties in comparison of crystalline alloys. So that the BMGs present higher tensile strength

while any conventional crystalline alloys show fewer. Tensile strength of the BMGs ranges between 800-2150 MPa combined with elastic modulus of 45-112 GPa depending on the alloy system[15].

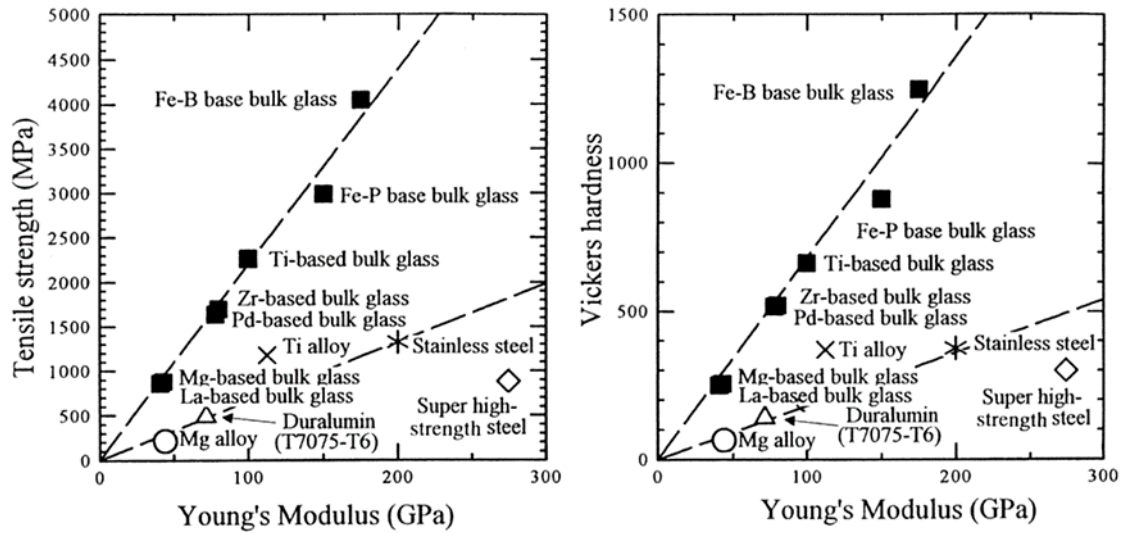


Figure 2.1. Relationship between tensile strength, Vickers hardness (Hv) and E for various bulk amorphous alloys [15].

2.1.2.2. Magnetic Properties

Magnetic properties have essential significance in the field of electrical and electronic industries. Accordingly, Co-, Ni-, and Fe-based amorphous metallic alloys are being widely investigated as a part of BMGs research, especially owing to their outstanding soft magnetic properties. Their superior soft-magnetic features are provided by the lack of structural inhomogeneities which prevent the domain wall motion during magnetization. Therefore, outstanding soft magnetic properties with the high magnetic permeability and low coercive force can be obtained. Soft magnetic properties have been exploited for applications in various areas for instance cores, transformers, microwave devices, magnetic shielding, transformers, cantilevers, and sensors [16].

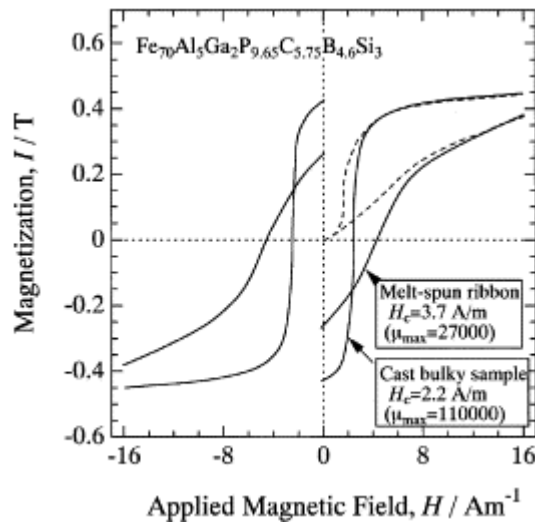


Figure 2.2 A comparison of I-H hysteresis loop of the cast ring-shape Fe-based BMG and similar ring-shape alloy made by stacking the melt-spun ribbons [17].

Mainly Fe- and Co-based BMG systems are used for magnetic applications [18]. It is also worth mentioning that, ferromagnetic metallic glasses have superior magnetic properties compared to the BMGs, to be used for electronic applications. It is still work in progress to achieve excellent soft magnetic properties at BMG. To give an example for that, Figure 2.2 shows a comparative I-H hysteresis loop of the Fe-based BMG and melt-spun ribbons with the similar alloy composition [17]. It can be seen that the melt-spun ribbon has a higher initial maximum permeability and lower coercive force with a value of 2.2 A/m.

2.1.2.3. Formability

Bulk metallic glasses show extraordinarily large elongation when they deformed at temperatures close or higher than the glass transition temperature. An example given in Figure 2.3, that belongs a deformed sample to 20,000% of La₅₅Al₂₅Ni₂₀ alloy in the supercooled liquid region, can be given as a visual example of the extent to which cast metallic glasses can be shaped [19]. For that reason, BMGs can be beneficial in the field of near-net-shape production.

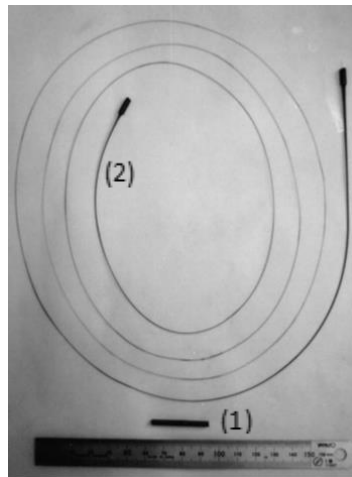


Figure 2.3 A La₅₅Al₂₅Ni₂₀ alloy (1) before deformation, (2) after deformation to 20,000% in the supercooled liquid region [19].

2.1.2.4. Corrosion Resistance

The amorphous structure has a valuable effect on corrosion resistance. This prospect of BMGs is basically clarified with the absence of crystal defects like dislocations or grain boundaries which could behave the initial point of the localized corrosion. Also, the optimized composition and the chemical homogeneity of the metallic glass can be given as the reason behind their excellent corrosion resistance [20]. To give an example of the great corrosion behavior of BMGs of Mg-based BMGs could be explored. This study conducted by Gebert et al. [21] revealed that the Mg-based BMGs has enhanced corrosion resistance compared to that of conventional alloy AZ31 and pure Mg, Figure 2.4.

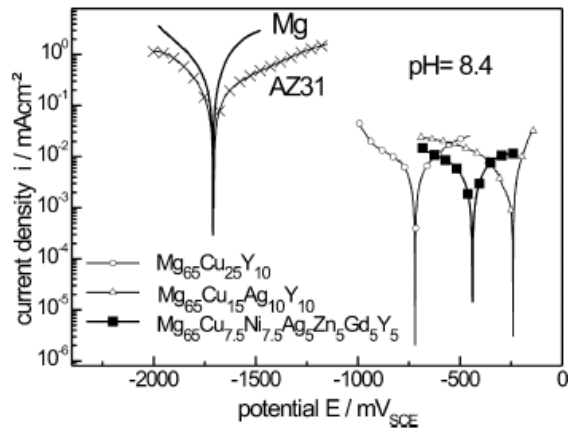


Figure 2.4 Current density curves related with the potential for different Mg-based amorphous alloys and Mg and AZ31 recorded in borate buffer solution with pH=8.4 ($\nu = 0.5$ mV/s) [21].

Table 2.2 Some of the application fields of BMGs and related properties [22].

Properties	Application area
High impact fracture energy	Tool materials
High strength	Machinery structural materials
High fracture toughness	Die materials
High hardness	Cutting materials
High fatigue strength	Bonding materials
High corrosion resistance	Corrosion resistance materials
High elastic energy	Sporting goods materials
High reflection ratio	Optical precision materials
High viscous flowability	Composite materials
Good soft magnetism	Soft magnetic materials
High wear resistance and manufacturability	Medical devices materials

2.1.3. Origins of Glass Formation

When the liquid metal is cooled down up to the melting point T_m , its volume generally decreases. At the melting point, specific volume of the metal shows a steep decrease until it gets the standard volume of the crystalline solid. depending on metal's thermal expansion coefficient, additional fall of the temperature, namely below T_m , cause a slow decrease of the volume, Figure 2.5. Even though the specific volume decreases rapidly at the T_m , the liquid normally undercools to overcome activation energy barrier to initiate the crystallization process. On the contrary, this situation is quite different for glass-forming systems. The glass-forming liquid can be considerably undercooled, by applying a high cooling rate. Systems volume continues to decrease and its viscosity increases. The viscosity gets too high when some specific point is reached, the liquid structure is preserved, and this structure can be referred as glassy structure.

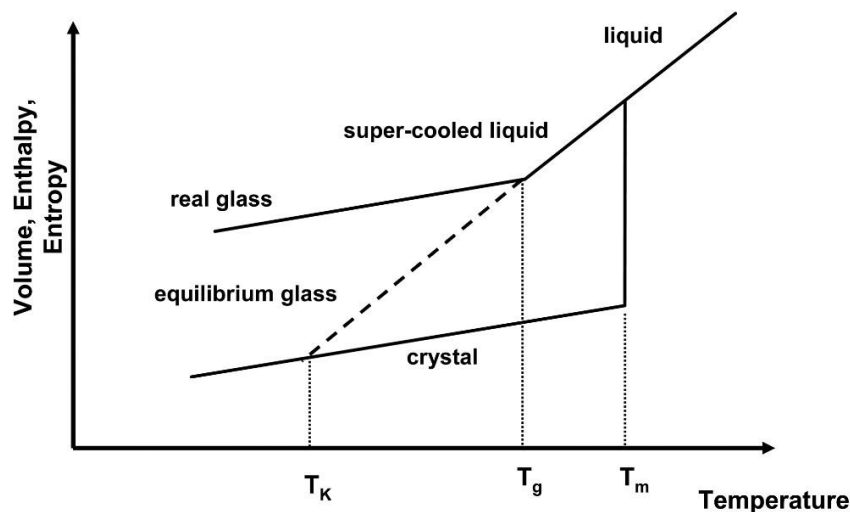


Figure 2.5 Specific volume change related with temperature for a crystalline and a glass-forming material.

The amount of undercooling is a very important aspect to acquire an amorphous structure and it usually depends on some parameters such as the liquid phase viscosity,

the amount of undercooling, the level of viscosity increase with decreasing temperature, the volume density of heterogeneous nucleating sites, the interfacial energy between liquid and crystal and most importantly the rate of cooling.

With the help of the differential scanning calorimetry (DSC), scanning electron microscopy (SEM), X-ray diffraction (XRD), and transmission electron microscopy (TEM) the amorphous nature of the metallic alloy can be verified. The characteristic XRD pattern of an amorphous solid shows a broad bump rather than sharp Bragg diffraction peaks as in crystals, Figure 2.6. Amorphous structures can also be identified with a transmission electron microscopy (TEM).

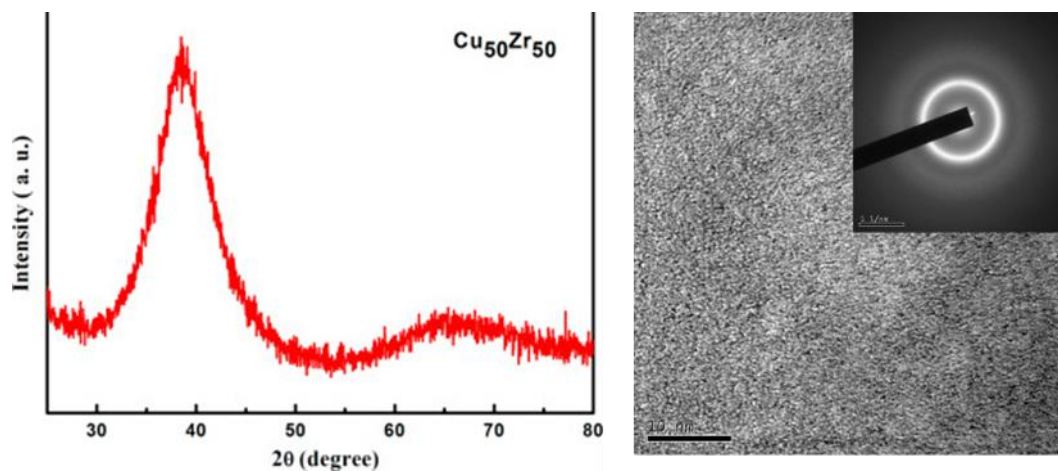


Figure 2.6 XRD pattern and TEM images of $\text{Cu}_{50}\text{Zr}_{50}$ amorphous alloy [23].

2.1.3.1. Glass Formation in Thermodynamics Point of View

Thermodynamic properties of a system are key factor for evaluating the stability of liquid and crystalline phases. System's thermodynamic stability is verified by Gibbs free energy (G) using classical thermodynamic laws. Gibbs free energy of a system can be represented by the following equation using absolute temperature (T), enthalpy (H), and entropy (S).

$$G=H-TS \quad (2.1)$$

Thermodynamically, if the system has the lowest value of the G, this indicates that the system is in their stable state at given temperature and pressure. Additionally, transformations are possible which will cause a reduction in G. Thus, a required condition phase transformation:

$$\Delta G=G_{\text{amorphous}}-G_{\text{crystalline}}=\Delta H_f-T\Delta S_f \quad (2.2)$$

ΔG denotes the change in G upon transformation where ΔS_f stands for the entropy of fusion while ΔH_f denotes enthalpy of fusion. When ΔG is negative the system is in a stable state. Which means that the final state of a transformation should has the less G than initial state. A decrease in ΔG can be achieved by changing the value of ΔH_f or ΔS_f . The entropy value gets higher as the number of components in the alloy system increases because entropy is a degree of the different microscopic arrangement of the atoms. Therefore, the free energy will decrease as a result of the increasement in the entropy value when the alloy system contains many constituents.

In addition, decrease in the free energy of the system can also be achieved by obtaining low chemical potential as a result of the increased interface energy between the liquid and solid phases. However, it is very challenging to manage these parameters in a system. Therefore, the easiest way to reduce G is to increase ΔS_f by designing a system with multiple components. That is the reason why it is much easier to synthesize amorphous structures in complex alloy systems. Increase in ΔS_f , also

improves the packing of the atoms, which can result in a decrease of ΔH_f value and subsequently a rise in the interface energy between solid and liquid [24].

2.1.3.2. Glass Formation in Kinetics Point of View

Simply stated that the metallic alloy liquid can be transferred into the amorphous structure, only when solidification into crystal structure could be prevented. Thus, the glass formation can be evaluated basically from a kinetics point of view. So, if enough cooling rate could be applied to avoid any crystallization, amorphous structure could be obtained. Thus, formation of the glass is correlated with the rate of the cooling and the kinetic constants. The crystallization kinetics studied by Turnbull [25] by using the given statements:

1. Nucleation transient events are insignificant.
2. The formed crystals and the liquid have the same composition.
3. Transformation of the liquid phase into the crystalline phase results in the change of the G. ΔG_v , is given as, $\Delta G_v = \Delta H_f^* \Delta T_r$, where $\Delta T_r = (T_m - T)/T_m$.

I, which expresses the homogeneous nucleation rate for the forming of crystal cores from a supercooled melt, can be calculated as follows [25]:

$$I = \frac{k_n}{\eta(T)} \exp \left[- \frac{b\alpha^3\beta}{T_r(\Delta T_r)^2} \right] \quad (2.3)$$

$$\alpha = \frac{(N_A \bar{V}^2)^{1/3} \sigma}{\Delta H_f} \quad (2.4)$$

$$\beta = \frac{\Delta S_f}{R} \quad (2.5)$$

Where

b is a shape factor ($= 16\pi/3$ for a spherical nucleus), k_n is a kinetic constant, $\eta(T)$ is the shear viscosity of the liquid at temperature T , T_r is the reduced temperature ($T_r = T/T_m$), ΔT_r is the reduced supercooling ($\Delta T_r = 1 - T_r$), N_A is Avogadro's number, \bar{V} is the molar volume of the crystal, and R is the universal gas constant

It is clear from equation for I that, the nucleation rate decreases as $\alpha^3\beta$ increases for a given ηT (viscosity at temperature T). Since α and β are related with the ΔS_f and ΔH_f , any increment in β and α means a decrease in ΔH_f and an increase in ΔS_f . This kinetic explanation of the crystallization is completely compatible with the thermodynamic approach explained previously.

2.1.3.3. Glass Formation in The Atomistic Point of View

Many of the criteria described previously require a knowledge of the specific transformation temperatures like T_g , T_x , T_m , etc. of the systems to predict the GFA of alloys. However, it is hard to find these temperatures using only phase diagrams especially for the multicomponent alloy systems. That is why, the alloy should be produced first then transformation temperatures should be determined in order to assess GFA of the system. Then it can be said that whether the alloy system has a high GFA or not. In order to reduce the number of experiments to be done, theoretical modelling and computer simulation studies are a key scientific topic in the metallic glass investigations. With the significant advances in the computer power, prediction of the GFA of an alloy without doing excessive number of experiments can be possible. In this context, some theoretical modelling and computer simulations offer an alternative and effective approach to study materials from the atomic level [26].

The atomic interactions among all of the atoms of a defined system are defined by the interatomic potentials. Therefore, when the potential is known, basic structural, energetic and dynamical behavior of the interacting atoms could be computed via different simulation methods. For this process the first step is to define empirical (Lennard-Jones, Morse, Born-Mayer) or semi-empirical potentials (Embedded Atom

Method (EAM), Finnis–Sinclair, Glue Model, n-body potentials) to describe the force field. Once the interatomic potential of the metal system is developed, the interatomic interactions and physical behaviors could be iteratively determined through numerical algorithms implemented on a computer by using the relevant simulation (Statics, Monte–Carlo, Molecular–Dynamics, and Lattice–Dynamics) [27].

2.1.4. Glass Forming Ability and Related Criteria for the Scope of This Thesis

The term glass forming ability (GFA) mainly means the easiness in the formation of amorphous structure deriving out of a liquid phase and high endurance to crystallization of the liquid. From the most general aspect, if the liquid phase structure can be conserved during cooling and the precipitation of the crystallization process gets more difficult, subsequently the glass formation could be obtained. Thus, GFA parameters principally involve two components:

- Resistance to crystallization
- Stability of the liquid phase

Liquid structure stability can be associated with the thermodynamic factors which are composed of ΔH_{mix} and ΔS_{mix} . On the other hand, resistance to crystallization depends on kinetic factors which are identify with the characteristic temperatures (T_x , T_g and T_m). Up to now many empirical rules concerning these factors have been developed such as the amount of negative heat of mixing [28], solidification model [29], deep eutectic rule [30], a reduced transition temperature T_{rg} [25] ($= T_g/T_m$, where T_m is the liquidus temperature in this case), a supercooled liquid range ΔT_{xg} [31] ($= T_x - T_g$, where T_x is the onset crystallization temperature), and $T_x/(T_g + T_m)$, $\alpha=T_x/T_m$ [32], $\gamma=T_x/T_g+T_m$ [33] and Inoue’s three empirical rules [15].

In the following section parameters considered in the scope of this thesis are going to explain.

2.1.4.1. Critical Cooling Rate (R_c)

Critical cooling rate (R_c) which denotes the least possible cooling rate needed to obtain an amorphous structure, is the most basic and commonly used parameter for defining GFA of a metallic system. Generally speaking, alloy system which has good GFA should possess low R_c and it is mostly dependent on the composition and type of the alloy system. That is the reason why metallic glasses (MGs) which are composed of two different metals have higher critical cooling rate relative to bulk metallic glasses (BMGs) which are typically multicomponent systems. For MGs, the value of R_c is in the range between 10^4 – 10^6 K s^{-1} . When the number of constituents increases, the R_c value decreases further, and as a result for multi-component alloys, R_c will typically be about 10^2 K s^{-1} or less [34]. A representative TTT diagram can be useful to understand the effects of the critical cooling rate on glass formation, Figure 2.7.

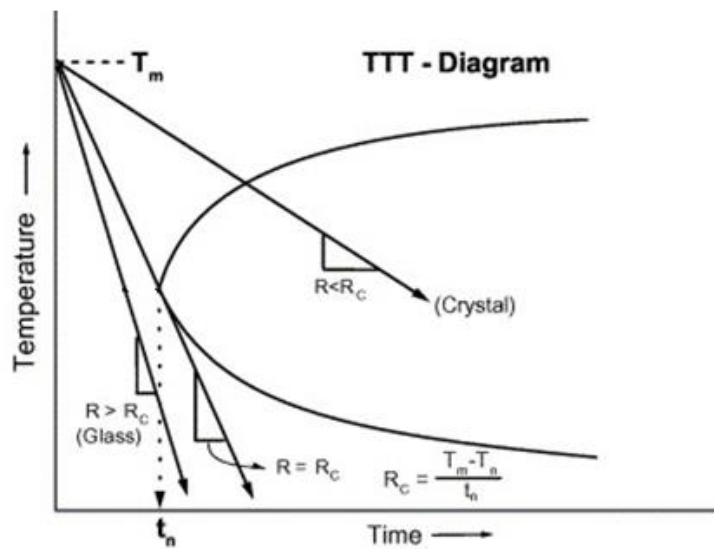


Figure 2.7 Schematic diagram of a typical nose-shaped temperature–time–transformation for a hypothetical melt [34].

As the liquid phase is cooled down below the T_m , solidification starts at T_m and consequently crystalline solid is obtained as the final structure. On the other hand, if the same liquid composition is cooled at a rate faster than the R_c , the liquid will be in the undercooled state down below the T_m , and when temperature reaches to the T_g , liquid phase structure is conserved and consequently an amorphous structure is formed. Generally speaking, formation of glass in pure metals is more difficult and requires an extremely high R_c . Conversely, R_c for multicomponent alloys is relatively less, Figure 2.8 [35]. Because BMGs are typically multi-component systems, production of them in the bulk form is possible at reasonably lower critical temperatures.

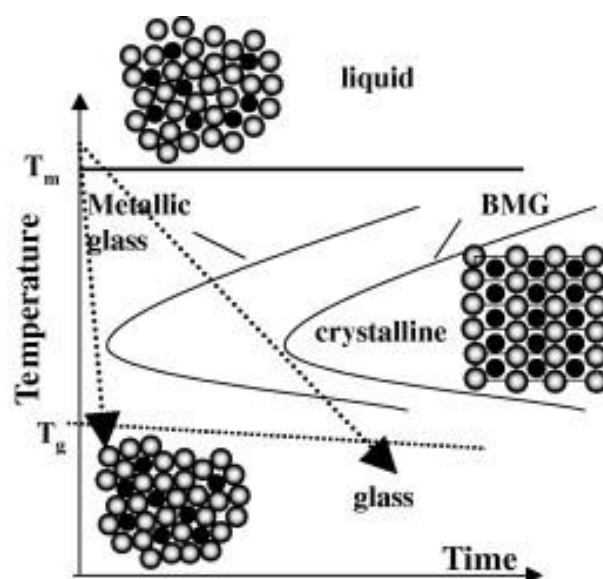


Figure 2.8 Effect of alloying element addition on TTT diagram [35].

2.1.4.2. Inoue's Empirical Rules

Due to the fact that metallic glass liquid is not stable at temperatures below the liquid melting point, it can solidify directly in the crystal phases. Therefore, in 2000 Inoue worked on many bulk metallic glass systems which have high supercooled liquid

region and tried to find the common concepts involved in these systems. These concepts were formulated as three main guidelines empirically for the formation of the BMG. These guidelines can be summarized as follows [15]:

1. To make the formation of amorphous structure easier, the alloy system should consist of minimum three constituent elements.
2. To obtain efficiently packed atomic structure in the liquid state, atomic size difference between the major components contained in the system should be minimum 12%.
3. Negative heat of mixing between the main components in the alloy system is required.

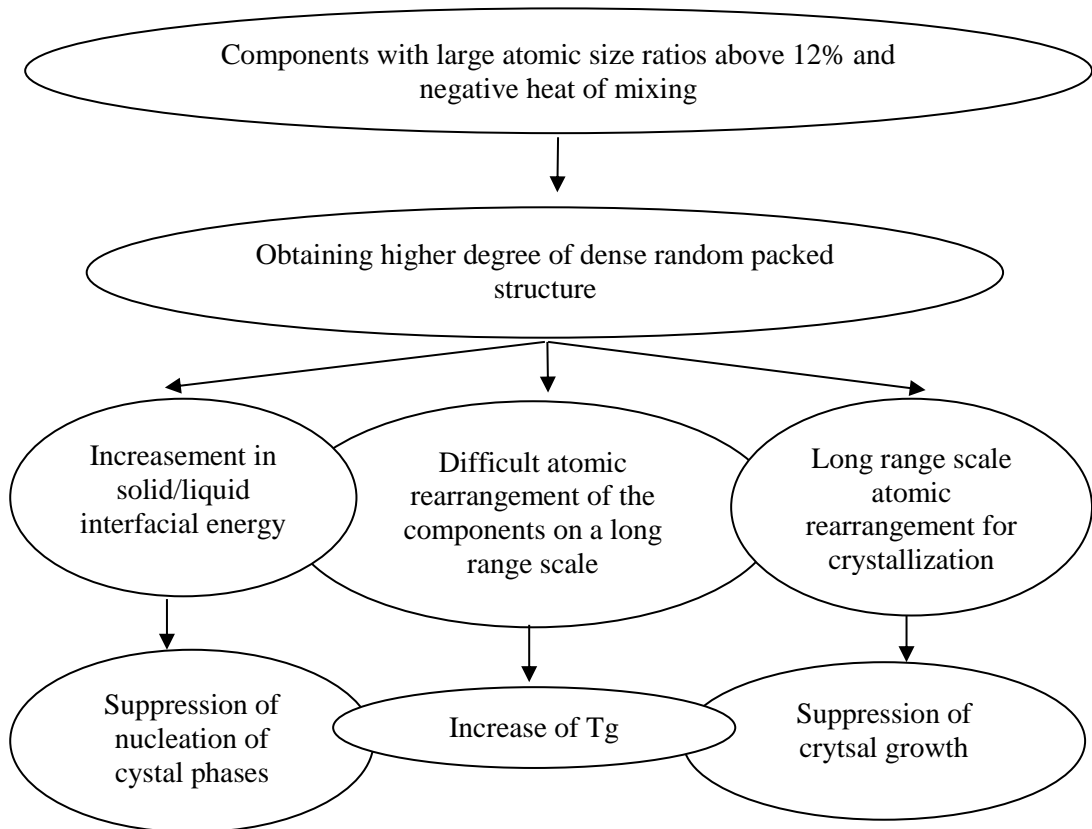


Figure 2.9 Schematic cause and effect relationship of three empirical rules to obtain glass formation [15].

2.1.4.3. Reduced Glass transition Temperature (T_{rg})

Glass formation in the pure kinetics point of view, Turnbull suggested that crystal nucleation depends on the viscosity of liquid. For that reason, the ratio T_g and T_m should be a good indicator for high GFA. The higher this ratio means the higher viscosity value and therefore the alloy liquid can readily solidify in glassy state at much lower critical cooling rates. To put it another way, high T_g value and a low T_m value will favor the amorphous structure formation. This ratio is introduced as the reduced glass transition temperature, T_{rg} , and is expressed as follows [25]:

$$T_{rg} = \frac{T_g}{T_m} \quad (2.6)$$

2.1.4.4. Alloy Systems with Deep Eutectic

It is known that as the solute content increases the liquidus temperature (T_l) value generally decreases. But in the case of a system with eutectic melting point, eutectic composition exhibits significantly lower melting point. As the eutectic point is approached, the liquidus temperature decreases, Figure 2.10. In such cases, stability of liquid phases would be possible even at lower temperatures. Consequently, it would be easy to obtain amorphous structure in eutectic alloy composition.

System which have eutectic point support glass formation at near or lying to the eutectic composition in the following ways [30]:

1. by increasing the glass transition temperature (T_g)
2. by increasing the stability of the liquid state relative to the crystal at the same composition
3. by decreasing the rate of crystal growth

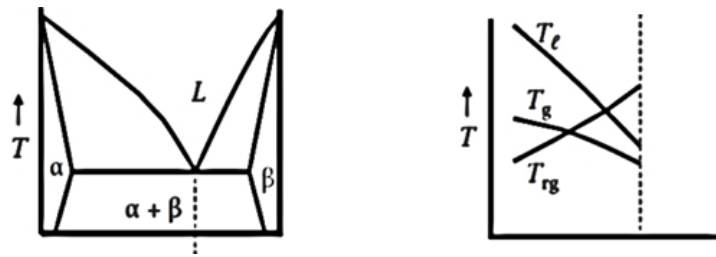


Figure 2.10 Schematic phase diagram of an eutectic system [30].

2.1.4.5. Solidification Behavior

As it mentioned before, glass formation can be possible when crystalline phases are resistant to crystallization. Accordingly, the systems having phases with higher level of complexity of crystallization like intermetallics could be useful for finding alloys with high GFA. Additionally, systems with sequential peritectic and eutectic transformations on cooling increase the glass making ability by making the crystallization process more difficult [29]. Figure 2.11 shows the melting reactions throughout the sequence of peritectic and eutectic reactions.

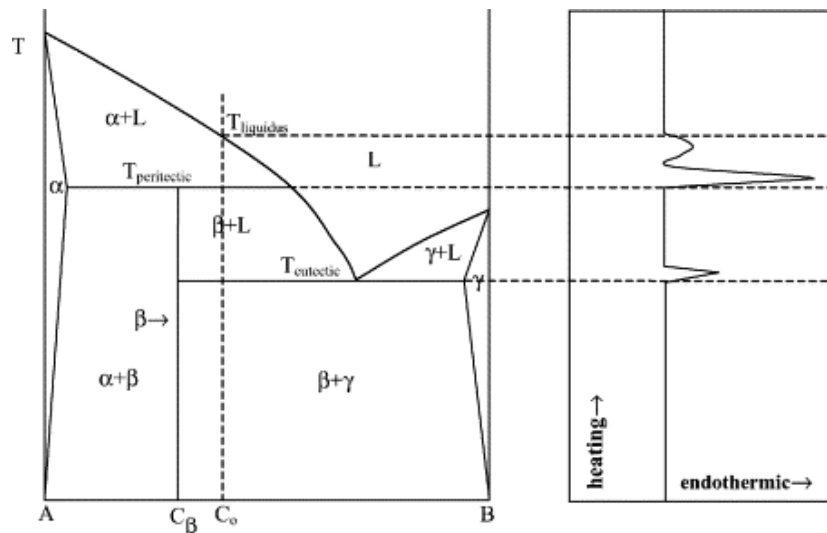


Figure 2.11 Schematic melting DSC curve of a hypothetical binary alloy including a sequence of eutectic and peritectic reactions upon heating [29].

2.2. Review on the Ti Based Bulk Metallic Glasses

By the all of the BMG systems, exclusively Ti-based BMG systems have received great interest because of superior properties they have, especially high specific strength, improved biocompatibility, good corrosion resistance, , and reasonable elastic modulus to be used in various engineering applications [12]. Additionally, being easily accessible and its low cost extended the potential usage area of Ti-based BMGs. For that reason, in the last three decades, Ti-based BMGs have been studying extensively. Therefore, many studies have been conducted in this field and since the first reported Ti-based amorphous alloy system developed by Tanner in Ti–Be–Zr ternary [36], numerous Ti-based BMG systems have been developed.

A Ti-based alloy system (Ti–Zr–Be–Ni) exhibiting a large supercooled liquid region extending to 45 K was reported by Peker in 1994 [37]. Since the wide supercooled liquid region leads to a high thermal stability against crystallization, these Ti–Zr–Be–Ni alloy system could be predicted as a prospective bulk metallic glass former. The first Ti-based BMG was synthesized successfully in a Ti–Cu–Ni–Sn alloy system by using copper mold casting in 1998 [38]. Thanks to this success, a number of Ti-based BMGs, such as Ti–Ni–Cu–Zr–Sn [39, 40], Ti–Cu–Ni [41, 42], Ti–Zr–Be [43, 44], Ti–Zr–Cu–Ni–Be [45], Ti–Cu–Zr–Fe–Sn–Si–(Ag, Sc) [46-48], Ti–Zr–Hf–Cu–Ni–Si–Sn [49], and Ti–Zr–Cu–Pd–(Si, Sn, Nb) [50], have been developed. Up to now, the largest known maximum castability thickness for Ti-based BMGs is over 50 mm in diameter, and this value is obtained in the Ti–Zr–Cu–Ni–Be [51] and Ti–Zr–Cu–Fe–Be [52] systems. Some of the previously found Ti-based BMG compositions until 2019 were given in Table 2.3 with their references.

Table 2.3 Some of the previously found Ti-based BMG compositions until 2019.

Alloy Composition	Year	Reference
Ti ₅₀ Be ₄₀ Zr ₁₀	1997	[36]
Ti ₅₀ Ni ₂₀ Cu ₂₅ Sn ₅	1998	[38]
Ti ₅₀ Cu ₂₀ Ni ₂₄ Si ₄ B ₂	1999	[53]
Ti ₅₀ Ni ₂₄ Cu ₂₀ B ₁ Si ₂ Sn ₃	2001	[54]
Ti ₄₅ Cu ₂₅ Ni ₁₅ Sn ₃ Be ₇ Zr ₅	2003	[55]
Ti _{41.5} Zr _{2.5} Hf ₅ Cu _{42.5} Ni _{7.5} Si ₁	2004	[56]
Ti ₅₃ Cu ₁₅ Ni _{18.5} Al ₇ Zr ₃ Si ₃ B _{0.5}	2004	[57]
Ti ₄₀ Zr ₂₅ Ni ₃ Cu ₁₂ Be ₂₀	2005	[58]
Ti _{41.3} Cu _{43.7} Hf _{13.9} Si _{1.1}	2005	[59]
Ti ₅₃ Cu ₁₅ Ni _{18.5} Al ₇ Sc ₃ Si ₃ B _{0.5}	2005	[60]
Ti ₅₃ Cu ₂₇ Ni ₁₂ Zr ₃ Al ₇ Si ₃ B ₁	2005	[61]
(Ti ₄₀ Zr ₂₅ Be ₂₀ Cu ₁₂ Ni ₃) _{99.5} Y _{0.5}	2006	[62]
Ti _{41.5} Zr _{2.5} Hf ₅ Cu _{37.5} Ni _{7.5} Si ₁ Sn ₅	2007	[49]
Ti ₄₁ Zr ₂₅ Be ₂₈ Fe ₆	2007	[63]
Ti ₅₀ Cu ₂₀ Ni ₂₄ Si ₄ B ₂	2008	[64]
Ti ₄₀ Zr ₁₀ Cu ₃₆ Pd ₁₄	2008	[65]
Ti ₅₀ Cu ₄₃ Ni ₇	2008	[42]
Ti ₅₀ Cu ₄₂ Ni ₈	2008	[41]
Ti ₄₀ Zr ₁₀ Cu ₃₄ Pd ₁₄ Sn ₂	2008	[66]
Ti ₄₁ Zr ₂₅ Be ₃₄	2010	[67]
Ti _{32.8} Zr _{30.2} Cu ₉ Fe _{5.3} Be _{22.7}	2010	[51]
Ti _{43.15} Zr _{9.59} Cu _{36.24} Ni _{9.06} Sn _{1.96}	2010	[40]
Ti ₄₅ Cu ₂₅ Ni ₁₅ Sn ₃ Be ₇ Zr ₅	2010	[68]
Ti _{42.5} Zr ₁₀ Cu _{42.5} Ni ₅	2010	[69]
Ti _{41.3} Cu _{43.7} Hf _{13.9} Si _{1.1}	2010	[69]
Ti _{32.38} Cu _{42.34} Ni _{9.28} Zr _{7.6} Hf _{8.4}	2011	[70]
Ti ₄₀ Zr ₂₆ Be ₂₈ Fe ₆	2012	[71]

Ti ₄₁ Zr ₂₅ Be ₂₈ Ag ₆	2012	[72]
Ti ₅₀ Ni ₂₄ Cu ₂₀ B ₁ Si ₂ Sn ₃	2012	[73]
(Ti ₄₁ Zr ₂₅ Be ₃₄) ₉₂ Fe ₈	2013	[74]
Ti ₄₁ Zr ₂₅ Be ₂₈ Al ₆	2013	[75]
(Ti ₄₁ Zr ₂₅ Be ₂₉ Al ₅) ₉₁ Cu ₉	2013	[76]
Ti ₅₀ Ni ₁₅ Cu ₂₅ Sn ₃ Be ₇	2013	[77]
(Ti ₄₁ Zr ₂₅ Be ₂₈ Fe ₆) ₉₁ Cu ₉	2013	[78]
Ti _{41.5} Zr _{2.5} Hf ₅ Cu _{42.5} Ni _{7.5} Si ₁	2014	[79]
Ti ₄₁ Zr ₂₅ Be ₂₈ Cu ₆	2014	[80]
Ti ₄₅ Cu ₄₀ Zr _{7.5} Fe _{2.5} Sn ₂ Si ₁ Sc ₂	2015	[47]
Ti ₄₄ Cu ₄₀ Zr _{7.5} Fe _{2.5} Sn ₂ Si ₁ Sc ₃	2015	[47]
Ti ₄₆ Cu _{27.5} Zr _{11.5} Co ₇ Sn ₃ Si ₁ Ag ₄	2015	[81]
Ti ₅₀ Zr ₁₆ Be ₂₄ Ni ₁₀	2015	[82]
Ti ₄₇ Zr _{7.5} Cu ₄₀ Fe _{2.5} Sn ₂ Si ₁	2016	[46]
Ti ₄₅ Cu ₄₀ Zr _{7.5} Fe _{2.5} Sn ₂ Si ₁ Sc ₂	2016	[48]
Ti ₄₄ Cu ₄₀ Zr _{7.5} Fe _{2.5} Sn ₂ Si ₁ Sc ₃	2016	[48]
Ti ₅₀ Cu ₂₀ Ni ₂₄ Si ₄ B ₂	2016	[83]
(Ti ₅₅ Zr ₁₅ Be ₂₀ Ni ₁₀) ₉₆ Fe ₄	2018	[84]
Ti ₅₀ Zr ₂₅ Cu ₁₇ S ₈	2019	[85]

2.2.1. Properties and Applications of Ti Based Bulk Metallic Glasses

Unquestionably, Ti-based BMGs are the most suitable low-density BMG systems to be used in structural engineering applications. Their promising properties such as excellent corrosion resistance, outstanding biocompatibility, high specific strength, high hardness, and large elastic elongation enable the use of Ti-based BMGs in medical applications, aerospace engineering, and structural engineering areas.

These alloys have the same density values as crystalline Ti alloys, in the range between 4.5 and 7 g/cm³. Accordingly, they have very high specific strengths. As can be seen in Table 2.4, Ti-based BMGs exhibit high yield strengths of 1900–2390 MPa, which is much higher than that of other light metal-based BMGs and in the same level as that of Zr-based BMGs.

Table 2.4 σ_y : Yield strength; σ_{max} : ultimate strength; σ_c : specific strength (σ_y /density); E : Young's modulus.

Composition (atom %)	Density (g/mm ³)	σ_y (MPa)	σ_{max} (MPa)	σ_c (N·m/kg)	E (GPa)	Ref.
Ti ₅₀ Cu ₄₃ Ni ₇			2050			[42]
Ti ₄₁ Zr ₂₅ Be ₃₄	4.88	1891	2238	3.88×10^5		[67]
Ti ₆₅ Cu ₉ Ni ₈ Be ₁₈	4.84	2383	2250	4.51×10^5	110	[86]
Ti ₆₀ Zr ₅ Cu ₉ Ni ₈ Be ₁₈	4.98	2383	2250	4.3×10^5	98	[86]
Ti ₄₇ Cu ₃₈ Zr _{7.5} Fe _{2.5} Sn ₂ Si ₁ Ag ₂	6.30	2010	2080	3.20×10^5	100	[47]
Ti ₄₅ Zr ₁₆ Be ₂₀ Cu ₁₀ Ni ₉	5.32		2105			[87]
Ti ₄₄ Cu ₄₀ Zr _{7.5} Fe _{2.5} Sn ₂ Si ₁ Sc ₃	6.20	1963	2042	3.20×10^5	95.4	[48]
Zr _{52.5} Cu _{17.9} Ni _{14.6} Al ₁₀ Ti ₅	6.55	1850	1900	2.82×10^5	87.2	[88]
Mg ₅₇ Cu ₃₁ Y _{6.6} Nd _{5.4}	3.81	1126	1188	1.39×10^5	92.9	[89]
Al ₈₆ Ni ₇ Y _{4.5} Co ₁ La _{1.5}	3.14	1050		3.34×10^5		[90]
Ti–6Al–4V	4.40	729	954	1.66×10^5	110- 114	

To give an example to compare, the yield strength of the commercially widely used titanium alloy, Ti-6Al-4V, is in the range 835–885 MPa, which is almost half that of the Ti-based BMGs. Even though the density of the Ti-based BMGs is relatively higher than that of the other light metal-based BMGs (Al- and Mg-based), Ti-based BMGs have significantly superior properties with the specific strength above 4×10^5 N·m/kg and the density values below 5 g/cm^3 [91].

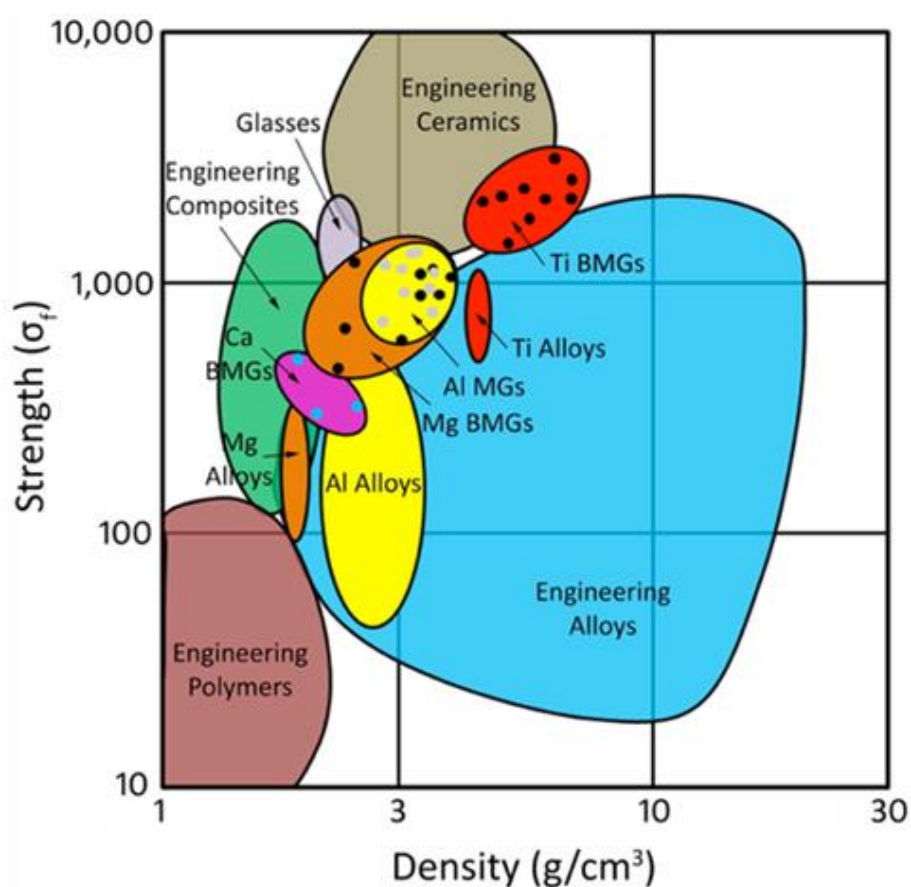


Figure 2.12 The Ashby diagram of strength versus density for engineering materials [91].

Figure 2.12 shows the Ashby diagram for various engineering materials [91]. It is clear from the Figure that Ti-based BMGs have a higher strength with the relatively low densities which means that they have higher specific strength compare to that of other

engineering materials. For example, Ti-based bulk metallic glass in the composition $\text{Ti}_{40}\text{Zr}_{29}\text{Be}_{14}\text{Cu}_9\text{Ni}_8$ with a large plastic strain of $\sim 7\%$, was reported by Park et al., (Figure 2.13) [87].

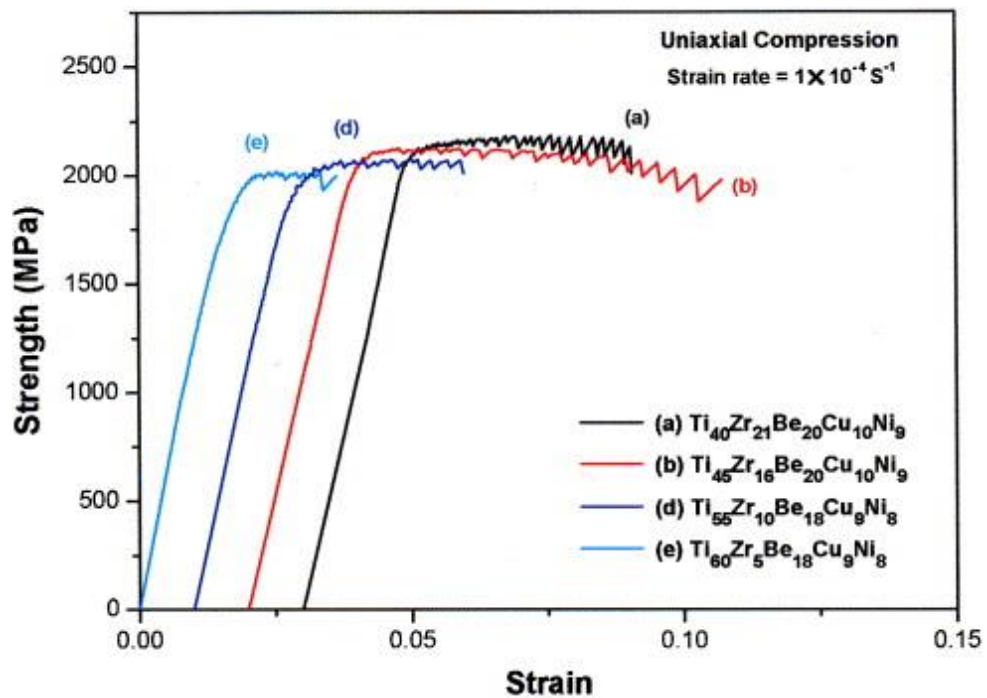


Figure 2.13 Compressive stress-strain curves of Ti-Zr-Be-Cu-Ni bulk metallic glasses [87].

Ti-based metallic glasses also exhibit superior corrosion resistance. In Figure 2.14 potentiodynamic polarization curves in Phosphate-Buffered Saline solution (PBS), 1 mol/L HCl, 0.9 wt. % NaCl, and 1 mol/L NaOH for a Ti-based BMG ($\text{Ti}_{46}\text{Cu}_{27.5}\text{Zr}_{11.5}\text{Co}_7\text{Sn}_3\text{Si}_1\text{Ag}_4$) and a conventional Ti alloy (Ti-6Al-4V), are given [81]. Compared to the conventional Ti alloy, Ti-based BMG was found to have a lower corrosion current density and a higher corrosion potential which providing a higher corrosion resistance.

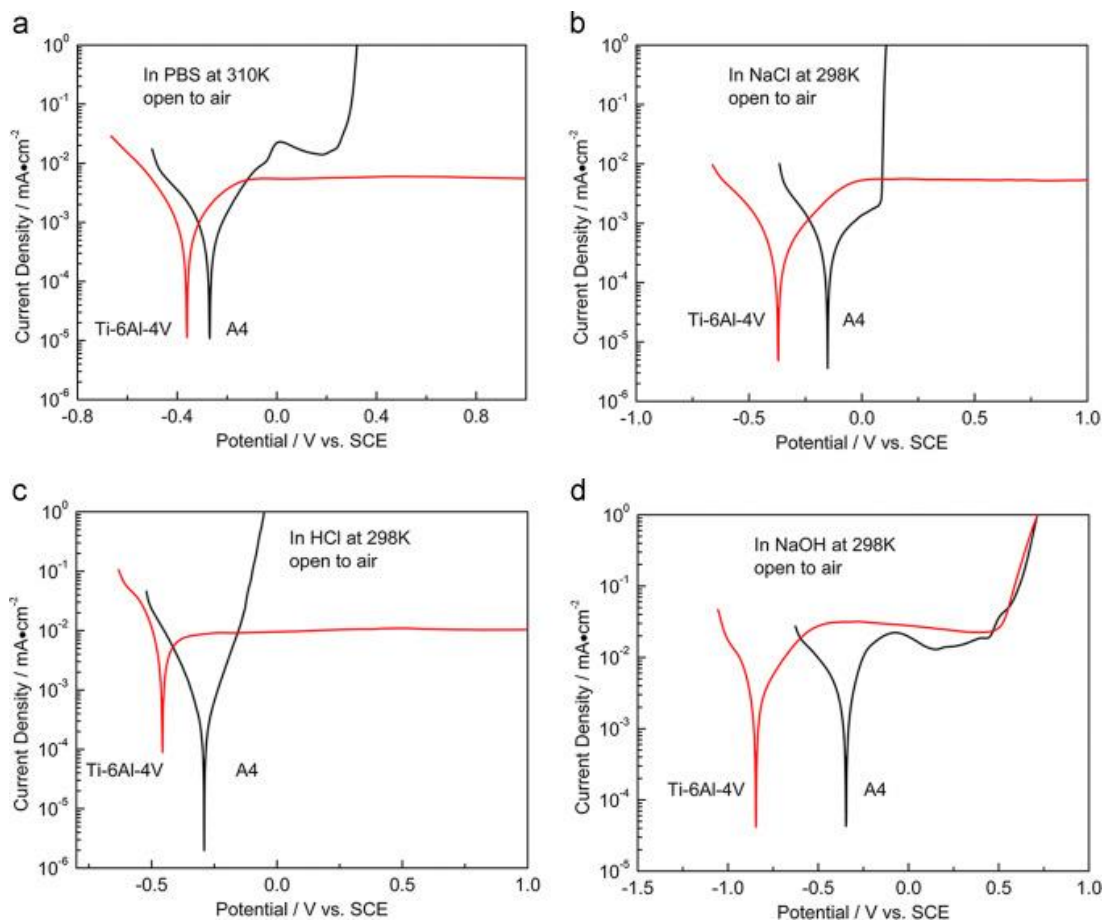


Figure 2.14 Current density versus potential curves of BMG and the Ti–6Al–4V alloy in (a) PBS, (b) 0.9 wt % NaCl, (c) 1 mol/L HCl, and (d) 1 mol/L NaOH solutions [81].

It is known that the Ti and its alloys are considered as well-suited materials to be used in biomedical applications. But beyond that, Ti-based BMGs have more satisfactory properties for this application area than conventional Ti alloys such as, lower elastic modulus, improved wear resistance and loadbearing capability, excellent thermoplastic formability, and great corrosion resistance [92, 93].

2.3. Alloy Design of Ti-Based Bulk Metallic Glasses by Theoretical Study

As previously mentioned, the prediction of the GFA of an alloy without doing an excessive number of experiments can be possible by using the power of theoretical modeling and computer simulations. In this context, GFA of Ti–Cu–X multicomponent alloy system was assessed via a theoretical study conducted by Suer, S., et al. [94]. For performing this assessment electronic theory of alloys in the pseudopotential approximation combined together with the statistical thermodynamical theory of liquid alloys was used.

The key thermodynamic parameters in determining GFA, such as enthalpy, Gibbs free energy of mixing, entropy, critical cooling rate, and viscosity were calculated using the value of atomic ordering energies which is the result of theoretical calculations to evaluate the potential alloying elements for Ti-Cu-X system.

2.3.1. Brief Explanation of Theory

As mentioned previously, thermodynamic parameters (i.e. entropy of mixing, ΔS_f , and enthalpy of mixing, ΔH_f) of a system provide a useful tool to evaluate GFA of a system. To be specific, if the change in free energy of the system, formulated as $\Delta G = G_{\text{amorphous}} - G_{\text{crystalline}} = \Delta H_f - T\Delta S_f$, has a negative value that indicates the amorphous structure has a lower free energy, that is, the stable structure in the system after cooling will be the amorphous structure. So, this could be achieved by an increase ΔS_f and a decreasing ΔH_f . These thermodynamic parameters are directly affected by the ordering energies between the components of the system. That is, the increase in the ordering energy of the system leads to an increase in entropy and enthalpy of mixing, as well as a reduction in R_c , which is the most important factor in determining GFA. As a result, when these interaction energies are calculated and used for the calculation of the thermodynamic parameters, the GFA of the systems becomes substantially assessable. For the purpose of ordering energy calculations, FORTRAN programs written by Prof. Dr. Amdulla Mekhrabov were used and the partial ordering energies

between the atoms of compound elements $Ti_{64}Cu_{35}X_1$ ternary system were calculated for numerous X elements using the following equations [94]:

$$W_{\alpha\alpha'}(R1) = \frac{\overline{\Omega}_0}{\pi^2} \int_0^{\infty} F_{\alpha\alpha'}(q) \frac{\sin(qR1)}{qR1} q^2 dq \quad (2.7)$$

Where

$$F_{\alpha\alpha'}(q) = \frac{\overline{\Omega}_0}{8\pi} |\omega_{\alpha}^0(q) - \omega_{\alpha'}^0(q)|^2 q^2 \frac{\varepsilon(q) - 1}{\varepsilon^*(q)} + \frac{2\pi}{\overline{\Omega}_0 q^2} |Z_{\alpha}^* - Z_{\alpha'}^*|^2 \exp\left(-\frac{q^2}{4\zeta}\right) \quad (2.8)$$

In Eqs. (2.7) and (2.8) $\overline{\Omega}_0$ is the average atomic volume of the ternary alloy; $\varepsilon(q)$ is the dielectric constant in the Hartree approximation; $\varepsilon^*(q)$ is the modified dielectric constant which takes into account the correlation and exchange effects; $\omega_{\alpha}^0(q)$ and $\omega_{\alpha'}^0(q)$ are the form-factors of unscreened pseudopotentials of a and a' component ions, respectively; Z_{α}^* ($Z_{\alpha'}^*$) is the effective valency of the a(a') component atoms and ζ is the Ewald parameter.

The calculated ordering energies have been used for the calculation of thermodynamic parameters (i.e. entropy of mixing, enthalpy of mixing, and Gibbs free energy of mixing) and some kinetic parameters (i.e. critical cooling rate and viscosity) of the Ti–Cu–X systems using the listed equations:

$$\Delta G_M = \Delta H_M - T\Delta S_M \quad (2.9)$$

where ΔG_M is free energy of mixing, ΔS_M is entropy of mixing, and ΔH_M is enthalpy of mixing. ΔS_M in terms of the mismatch term of entropy S_σ and ideal configurational entropy ΔS^{ideal} is defined as:

$$\Delta S_M = \Delta S^{ideal} + S_\sigma \quad (2.10)$$

$$\Delta S^{ideal} = -R \sum_{i=1}^N (c_i \ln c_i) \quad (2.11)$$

$$S_\sigma = k_B \left\{ \frac{3}{2} (\zeta^2 - 1) y_1 + \frac{3}{2} (\zeta - 1)^2 y_2 - \left[\frac{1}{2} (\zeta - 1)(\zeta - 3) + \ln \zeta \right] (1 - y_3) \right\} \quad (2.12)$$

where ζ is defined as $\zeta=1/(1-v)$, using packing fraction v . y_1 , y_2 and y_3 are parameters having a relation of $y_1+y_2+y_3=1$, and are defined as:

$$y_1 = \frac{1}{\sigma^3} \sum_{j>i=1}^n (d_i + d_j)(d_i - d_j)^2 c_i c_j \quad (2.13)$$

$$y_2 = \frac{\sigma^2}{(\sigma^3)^2} \sum_{j>i=1}^n d_i d_j (d_i - d_j)^2 c_i c_j \quad (2.14)$$

$$y_3 = \frac{(\sigma^2)^3}{(\sigma^3)^2} \quad (2.15)$$

$$\sigma^k = \sum_{j>i=1}^n c_i d_i^k \quad (2.16)$$

where d_i is the atomic diameter of i^{th} element and $k=2, 3$.

ΔH_M value of a multicomponent system including N elements can be calculated using following equation:

$$\Delta H_M = \sum_{i=1, i \neq j}^N \gamma_{ij} c_i c_j \quad (2.17)$$

$$\gamma_{ij} = \frac{ZW}{2} \quad (2.18)$$

where γ_{ij} is the regular solution interaction parameter between i and j elements which can be defines as Eq. 2.18 where, Z is the coordination number, W is the ordering energy and C_i and C_j are the atomic fractions of the elements..

Calculations of these key thermodynamic parameters allow critical cooling rate value to be calculated by using following equation:

$$R_c = \psi \frac{k_B T_m^2}{a^3 \eta_{T=T_m}} \exp \left[f_1 \left(\frac{\Delta H - T_m \Delta S^{ideal}}{300R} \right) - f_2 \left(\frac{T_m S_\sigma}{300R} \right) \right] \quad (2.19)$$

where ψ is a constant (2×10^{-6}), k_B is the Boltzmann constant, T_m is the melting temperature, a is the interatomic distance, $\eta_{T=T_m}$ is the viscosity at the melting temperature, and f_1 and f_2 are the fitting parameters. f_1 and f_2 were calculated as 0.75 and 1.2, respectively, by using the method of least-squares for 300 K. $\eta_{T=T_m}$ the value of viscosity at the melting temperature was calculated as following:

$$\eta(T_m) = c_A \frac{\sqrt{AT_m}}{V^{2/3}} \quad (2.20)$$

C_A is a constant of $1.85 \times 10^{-7} \text{ (J/K mol}^{1/3})^{1/2}$, A is the atomic weight, and V is the molar volume at T_m .

The calculated ordering energy and interchange energy and ΔH^M , S^σ , ΔS^{ideal} , ΔS^M , $\Delta\eta/\eta_0$ and critical cooling rate values for $\text{Ti}_{64}\text{Cu}_{35}\text{X}_1$ alloy are tabulated in Table 2.5 and Table 2.6 respectively.

The candidate alloying elements likely to increase the GFA of the Ti-Cu-X system were examined by considering two different effects of the elements, one of which causes a decrease in R_c and the other which causes an increase in the negative ΔH_{mix} . Candidate alloying elements are listed relatedly with their effects. Consequently, Ni, Al, V and Si were selected as alloying elements for Ti-Cu binary system based on the calculated candidate alloying elements list and literature review.

Alloying elements which cause a decrease in R_c	Alloying elements which cause both a decrease in R_c and an increase in negative ΔH_{mix}
Y, Sn, La, Be, Mg, Te, Mn, Cr, Co, Pt, Ni, In, Fe	Ag, Zn, Au, Al, P, Ga, Li, Hg, Si, Ge, Cd, Sc, V.

Table 2.5 Ordering energy and interchange energy values for $Ti_{64}Cu_{35}X_1$ alloy (in SI units)[94].

X	W_{Ti-Cu} J/mol (10^3)	W_{Ti-X} J/ mol(10^3)	W_{Cu-X} J/mol(10^3)	γ_{Ti-Cu} J/mol(10^4)	γ_{Ti-X} J/ mol(10^4)	γ_{Cu-X} J/mol (10^4)
None	-13.2399	–	–	-7.9439	–	–
Ag	-13.5212	-26.5546	3.1513	-8.1127	-15.9327	-1.8908
Au	-13.5212	-29.5164	14.2886	-8.1127	-17.7098	8.5731
Zn	-13.3861	-3.9898	-0.1907	-8.0317	-2.3939	-0.1144
Cd	-13.5023	-8.8691	-2.1499	-8.1014	-5.3215	-1.2899
Co	-13.3135	-0.6349	-2.2147	-7.9881	-0.3810	-1.3288
Hg	-13.5376	-9.2328	15.2698	-8.1225	-5.5397	9.1619
Sc	-13.4691	1.9929	-8.6149	-8.0815	1.1957	-5.1689
Y	-13.6148	11.8690	-6.5437	-8.1689	7.1214	-3.9262
La	-13.6932	15.8287	6.6936	-8.2159	9.4972	4.0162
Hf	-13.3235	34.4357	9.3534	-7.9941	20.6614	5.6121
V	-13.0779	-2.6114	-32.2390	-7.8467	-1.5668	-19.3434
Nb	-13.1510	32.1694	-15.1300	-7.8906	19.3017	-9.0780
Ta	-13.1510	28.6816	-16.4775	-7.8906	17.2090	-9.8865
Cr	-13.2326	3.9716	-7.0168	-7.9395	2.3829	-4.2101
Mo	-13.0158	50.2765	1.2438	-7.8095	30.1659	0.7463
W	-13.0164	57.6475	6.1320	-7.8098	34.5885	3.6792
Mn	-13.3345	-1.3239	-2.8556	-8.0007	-0.7943	-1.7134
Re	-12.9028	37.6946	-24.6762	-7.7417	22.6168	-14.8057
Fe	-13.2320	2.0953	-9.1168	-7.9392	1.2572	-5.4701
Ru	-13.1673	35.3994	2.7418	-7.9004	21.2396	1.6451
Os	-13.1758	34.0171	9.0713	-7.9055	20.4103	5.4428
Zr	-13.3424	36.1865	3.2015	-8.0054	21.7119	1.9209
Ir	-13.1778	33.9260	9.0685	-7.9067	20.3556	5.4411
Ni	-13.3104	-0.7037	-2.0938	-7.9862	-0.4222	-1.2563
Pd	-13.3803	35.4798	14.9374	-8.0282	21.2879	8.9624
Pt	-13.3861	-7.3242	18.6771	-8.0317	-4.3945	11.2063
Li	-13.5985	-12.4378	3.8334	-8.1591	-7.4627	2.3001
Be	-13.2567	5.8952	-1.4268	-7.9540	3.5371	-0.8561
Mg	-13.5312	9.3201	-8.9259	-8.1187	5.5920	-5.3555
Al	-13.3150	2.3885	-20.3147	-7.9890	1.4331	-12.1888
Ga	-13.3672	-4.5351	-6.7915	-8.0203	-2.7211	-4.0749
In	-13.4860	2.6782	11.7789	-8.0916	1.6069	7.0674
Si	-13.2798	-2.4949	-27.3036	-7.9679	-1.4970	-16.3822
Ge	-13.3261	0.8961	-17.6441	-7.9957	0.5377	-10.5865
Sn	-13.4071	15.3546	-5.6904	-8.0442	9.2128	-3.4142
Pb	-13.4644	23.5758	28.4315	-8.0787	14.1455	17.0589
As	-13.2125	11.076	4.3036	-7.9275	6.6457	2.5822
Sb	-13.3692	26.1992	5.8750	-8.0215	15.7195	3.5250
Bi	-13.4639	65.8925	79.7700	-8.0783	39.5355	47.8620
Te	-13.3366	16.6103	-21.6666	-8.0020	9.9662	-13.0000
B	-13.1478	27.9659	46.3431	-7.8887	16.7796	27.8059
C	-13.0217	10.7995	8.136	-7.8130	6.4797	4.8818

Table 2.6 ΔH^M , S^σ , ΔS^{ideal} , ΔS^M , $\Delta\eta/\eta_0$ and critical cooling rate for $Ti_{64}Cu_{35}X_1$ alloy (in SI units) [94].

X	ΔH^M J/mol (10^4)	S^σ J/mol.K	ΔS^{ideal} J/mol.K	ΔS^M J/mol.K	$\Delta\eta/\eta_0$	R_c K/s (10^5)
None	-1.8072	0.7044	5.3803	6.0847	1.6563	2.2140
Ag	-1.9126	0.7029	5.8096	6.5125	1.7529	1.3547
Au	-1.9006	0.7027	5.8096	6.5123	1.7419	1.3932
Zn	-1.8148	0.7017	5.8096	6.5113	1.6633	1.8267
Cd	-1.8533	0.7274	5.8096	6.5370	1.6985	1.5938
Co	-1.7964	0.7227	5.8096	6.5324	1.6464	1.9062
Hg	-1.8228	0.7119	5.8096	6.5215	1.6706	1.7497
Sc	-1.8207	0.7573	5.8096	6.5669	1.6687	1.7360
Y	-1.7980	0.8687	5.8096	6.6783	1.6479	1.7252
La	-1.7655	0.9466	5.8096	6.7562	1.6181	1.8025
Hf	-1.6388	0.7305	5.8096	6.5401	1.5020	3.0142
V	-1.8354	0.7089	5.8096	6.5186	1.6821	1.7114
Nb	-1.6757	0.7020	5.8096	6.5116	1.5358	2.7680
Cr	-1.7779	0.7232	5.8096	6.5329	1.6295	2.0158
Mo	-1.5537	0.7033	5.8096	6.5129	1.4239	3.9919
W	-1.5152	0.7030	5.8096	6.5126	1.3887	4.4469
Mn	-1.8032	0.7045	5.8096	6.5141	1.6527	1.8899
Re	-1.6412	0.7025	5.8096	6.5121	1.5042	3.0438
Fe	-1.7895	0.7254	5.8096	6.5350	1.6401	1.9437
Ru	-1.6280	0.7058	5.8096	6.5154	1.4921	3.1855
Os	-1.6211	0.7042	5.8096	6.5139	1.4858	3.2284
Zr	-1.6475	0.7399	5.8096	6.5496	1.5100	2.9421
Ir	-1.6218	0.7038	5.8096	6.5134	1.4864	3.2226
Ni	-1.7960	0.7241	5.8096	6.5337	1.6461	1.9070
Pd	-1.6307	0.7024	5.8096	6.5121	1.4945	3.1648
Pt	-1.7880	0.7019	5.8096	6.5115	1.6387	1.9563
Li	-1.8673	0.7139	5.8096	6.5235	1.7114	1.5562
Be	-1.7621	0.7658	5.8096	6.5755	1.6149	2.0666
Mg	-1.8015	0.7395	5.8096	6.5491	1.6511	1.8633
Al	-1.8230	0.7021	5.8096	6.5117	1.6708	1.7880
Ga	-1.8282	0.7017	5.8096	6.5114	1.6756	1.7537
In	-1.7775	0.7666	5.8096	6.5762	1.6291	1.9525
Si	-1.8517	0.7554	5.8096	6.5651	1.6971	1.5856
Ge	-1.8246	0.7257	5.8096	6.5353	1.6723	1.7455
Sn	-1.7549	0.7474	5.8096	6.5570	1.6084	2.1146
Pb	-1.6594	0.8256	5.8096	6.6352	1.5208	2.6610
Sb	-1.6839	0.7164	5.8096	6.5260	1.5433	2.6694
Te	-1.7742	0.7035	5.8096	6.5131	1.6260	2.0501
B	-1.5624	0.9458	5.8096	6.7554	1.4319	3.3630
C	-1.6916	0.9792	5.8096	6.7888	1.5503	2.2321

CHAPTER 3

EXPERIMENTAL PROCEDURE

3.1. Raw Materials

High purity elements were used in the sample production, since the impurity ratio is highly important in obtaining amorphous metallic glass. The purity percentages and forms of the elements used are listed below.

Table 3.1 *Form and purity levels of elements.*

Element	Form of Element	Purity Level (wt. %)
Ti	wire	99.90
Cu	shot	99.90
Ni	pieces	99.95
Al	shot	99.89
V	pieces	99.85
Si	lumps	99.85

3.2. Production of Alloys with Arc Melting

The designed alloy compositions were obtained by cutting and weighing of highly pure elements. The melting of solid mixtures was performed with arc melting under Ti-gettered argon atmosphere (Figure 3.1). During the experimental procedure, each composition was remelted several times to improve chemical homogeneity. When the chemically homogeneous mixture is obtained, molten alloy suck into water-cooled copper mold with the help of pressure difference between the copper mold and the melting chambers. At the end of the procedure, samples with 3mm in diameter and approximately 10cm in length are fabricated. Samples have two parts button and suction casting. The cooling rate at the suction part of sample is significantly faster than the cooling rate at the button part of sample.



Figure 3.1. *Edmund Bühler arc melting device equipped with water cooled copper mold suction casting unit and the copper mold.*

3.3. Metallographic Preparation

It is known that the Ti and its alloys are quite difficult to prepare for metallographic examination. For this reason, the sample preparation stages were very challenging, and a lot of time was spent on this. After many failed methods, perfect surface was achieved by the preparation stages listed below.

- Wet grinding with 220 grit SiC paper at 300 rpm for 3-4 minutes to obtain a cutting damage free surface.
- Wet grinding with 600, 800, 1200, 2000 and 2500 grit SiC paper at 300 rpm for 2-3 minutes for each.
- Polishing with 3 μ m aluminum oxide paste at 200 rpm for 10-15 minutes.
- Final polishing with colloidal silica suspension without any load.
- Etching for microscopic examination with a mixture of 5% HF, 10% HNO₃ and balance water for 20 seconds.

3.4. X-Ray Diffractometry

Phase analysis of all alloys were done by using Bruker D8 Advance XRD device under Cu K α radiation. The data were taken between 2 θ angles 20° and 100° with the scanning rate of 0.1°/minutes.

3.5. Scanning Electron Microscopy

Microstructural investigations of the samples were performed using FEI Quanta 400F field emission scanning electron microscope (FESEM) equipped with energy dispersive spectroscopy (EDS). EDS analysis were used to detect the composition of the differnt phases were presented in microstructure.

3.6. Differential Scanning Calorimetry

DSC analysis were performed to detect the transformation temperatures of alloy systems and also used for identification of glass transition and crystallization temperatures of any possible amorphous structure. These thermal analyses were carried out by using Setaram Setsys 16/18 DSC (Figure 3.2) which operates under high purity argon atmosphere. For analysis samples of 25-30 mg in weight were used. Samples, which were placed into yttrium oxide coated alumina crucible, were heated to 1350 °C with 40°/min heating rate and after that were cooled to the room temperature with the same rate.



Figure 3.2 Setaram Setsys–16/18 DSC used in the thermal analysis measurements.

3.7. Microhardness Measurement

All alloys were tested mechanically by using Shimadzu Micro Hardness Tester with the load of 0.2 kg. 15-20 points were taken from each sample to ensure enough sample size.

CHAPTER 4

RESULTS AND DISCUSSION

4.1. Selection of Alloy Compositions

The formation of metallic glass occurs during cooling of the metallic liquid phase to temperatures below the melting temperature, preventing the formation of all possible crystal phases. The lower the driving force required for solidification in a system, the higher the GFA will be. Likewise, GFA can be increased by identifying systems that contain stable liquid phase at much lower temperatures and contain complex transformations. As a result, searching for compositions with good GFA, phase diagrams can be used as a guideline [29].

Consequently, Ti-Cu binary system given in Figure 4.1, which includes eutectic point at 960 °C combined two intermetallics ($\text{Ti}_2\text{Cu}+\text{TiCu}$) and sequence of peritectic and eutectic reactions upon cooling, seems to be good candidate for high BGFA.

Table 4.1 *Eutectic reaction parameters for Ti-Cu binary and Ti-Cu-Ni ternary systems.*

Ti-Cu Binary System	Ti-Cu-Ni Ternary System
$\text{L} \leftrightarrow \text{Ti}_2\text{Cu} + \text{TiCu}$ eutectic reaction at 960°C	$\text{L} \leftrightarrow \text{TiCu} + \text{TiNi}$ pseudo-binary eutectic reaction at 924°C

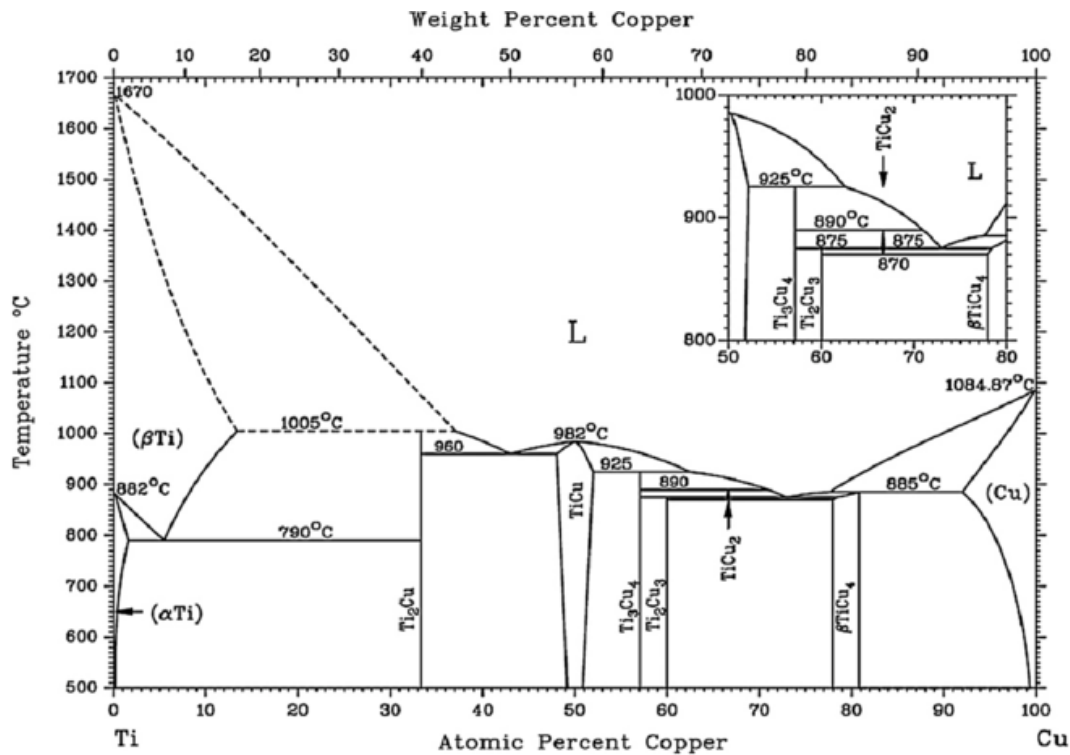


Figure 4.1 Ti-Cu binary phase diagram [95].

Ni is topologically and chemically similar to Cu. However, the resulting Ti–Cu–Ni ternary system includes a pseudo-binary eutectic ($L \rightarrow \text{TiCu} + \text{TiNi}$) which exhibits a eutectic reaction at 924 °C which is 26 K lower than the eutectic temperature of Ti–Cu binary system ($L \rightarrow \text{TiCu} + \text{Ti}_2\text{Cu}$). Figure 4.2 displays the vertical section of the ternary Ti–Cu–Ni phase diagram at the tie line between TiCu and TiNi. It can be seen from the Figure 4.2 that Ni has limited solubility in TiCu. In addition to that TiCu and TiNi intermetallics have very different crystal structures, tetragonal ($a = 0.3118 \text{ nm}$ and $c = 0.5921 \text{ nm}$) for TiCu [96] and CsCl type (B2, $a = 0.3015 \text{ nm}$) for TiNi [97], respectively. By using this Ti-Cu-Ni ternary phase diagram, BMGs with the critical diameter 1 mm to 1.5 mm were produced in the composition range between $\text{Ti}_{50}\text{Cu}_{50-x}\text{Ni}_x$ ($6 \leq x \leq 10$) [98].

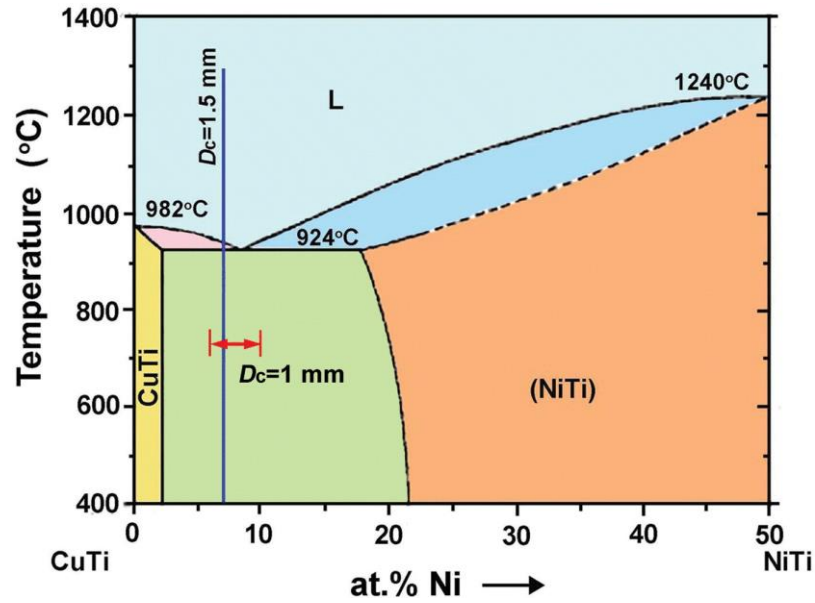


Figure 4.2 Vertical section of the ternary Ti-Cu-Ni phase diagram [98].

Based on criteria mentioned above and theoretical calculations explained before, for Ti-Cu binary system, Ni, Al, V and Si are decided to use for alloying. These elements decrease R_c and increase negative heat of mixing (ΔH_{mix}) according to the reference [99]. Calculated data were given in Table 4.2. Also, atomic size of the Al is close to that of Ti and the density of Al is lower than that of Ti which may increase the specific strength of Ti based BMGs.

Table 4.2 Calculated data of ΔH_{mix} and R_c [99].

$\text{Ti}_{64}\text{Cu}_{35}\text{X}_1$	$\Delta H_{\text{mix}} \text{ J/mol } (10^4)$	$R_c \text{ K/s } (10^5)$
None (binary)	-1.8072	2.2140
Si	-1.8517	1.5856
V	-1.8354	1.7114
Al	-1.8230	1.7880
Ni	-1.7960	1.9070

At first, Alloy 1 with the composition in atomic percentage $\text{Ti}_{48}\text{Cu}_{30}\text{Ni}_{10}\text{Al}_7\text{V}_5$ was selected to produce. Afterwards, effect of Si addition on Alloy 1, which decreases R_c and increases negative heat of mixing (ΔH_{mix}) according to the reference [99], was decided to examine as a minor alloying. Besides theoretical calculations, it was thought that due to their smaller atomic size compared to that of Ti could improve GFA. The reason behind this, GFA is also related to an increase of the short-range order which leads to an efficient packing in liquid. As a result, the formation of possible heterogeneous nucleation sites becomes difficult and better GFA can be obtained, Table 4.3.

Table 4.3 Atomic radii values of selected elements [100].

Element	Atomic Radii (nm)	R_{Ti}/R_x
Ti	0.1462	1
Cu	0.1278	1.144
Ni	0.1246	1.173
Al	0.1432	1.021
V	0.1316	1.111
Si	0.1153	1.249

Consequently, 3 alloy compositions given below in atomic percent were produced.

- Alloy 1: $\text{Ti}_{48}\text{Cu}_{30}\text{Ni}_{10}\text{Al}_7\text{V}_5$
- Alloy 2: $\text{Ti}_{47}\text{Cu}_{30}\text{Ni}_{10}\text{Al}_7\text{V}_5\text{Si}_1$
- Alloy 3: $(\text{Ti}_{48}\text{Cu}_{30}\text{Ni}_{10}\text{Al}_7\text{V}_5)_{97}\text{Si}_3$

Table 4.4 Codification of samples.

	Alloy 1	Alloy 2	Alloy 3
Slow cooling part of the alloy (a)	SC Alloy 1	SC Alloy 2	SC Alloy 3
Fast cooling part of the alloy (b)	FC Alloy 1	FC alloy 2	FC Alloy 3

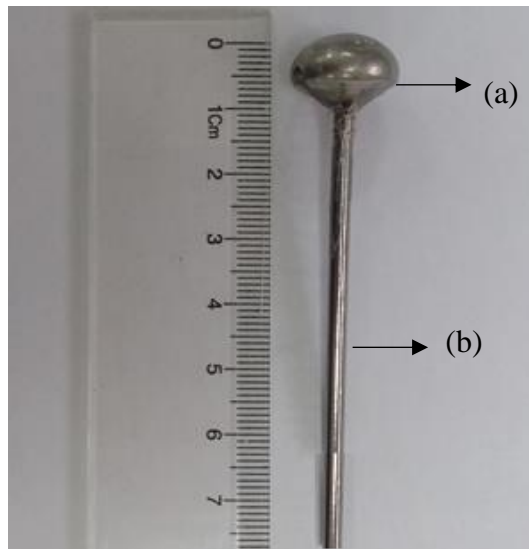


Figure 4.3 Sample produced with copper mold suction casting (a) slow cooling part, (b) fast cooling part.

Samples have two parts button and suction casting. The cooling rate at the suction part of sample is relatively faster than the cooling rate at the button part of sample, Figure 4.3.

4.2. Characterization of Alloy 1 ($\text{Ti}_{48}\text{Cu}_{30}\text{Ni}_{10}\text{Al}_7\text{V}_5$)

4.2.1. Slow Cooling Part of the Alloy 1

As seen from optical microscope images in different magnifications given in Figure 4.4. SC Alloy 1 was found to contain similar dendritic microstructure in every region. This solidification type points out that crystallization took place during solidification. For further microstructural investigation, sample was analyzed by using FESEM and EDS.

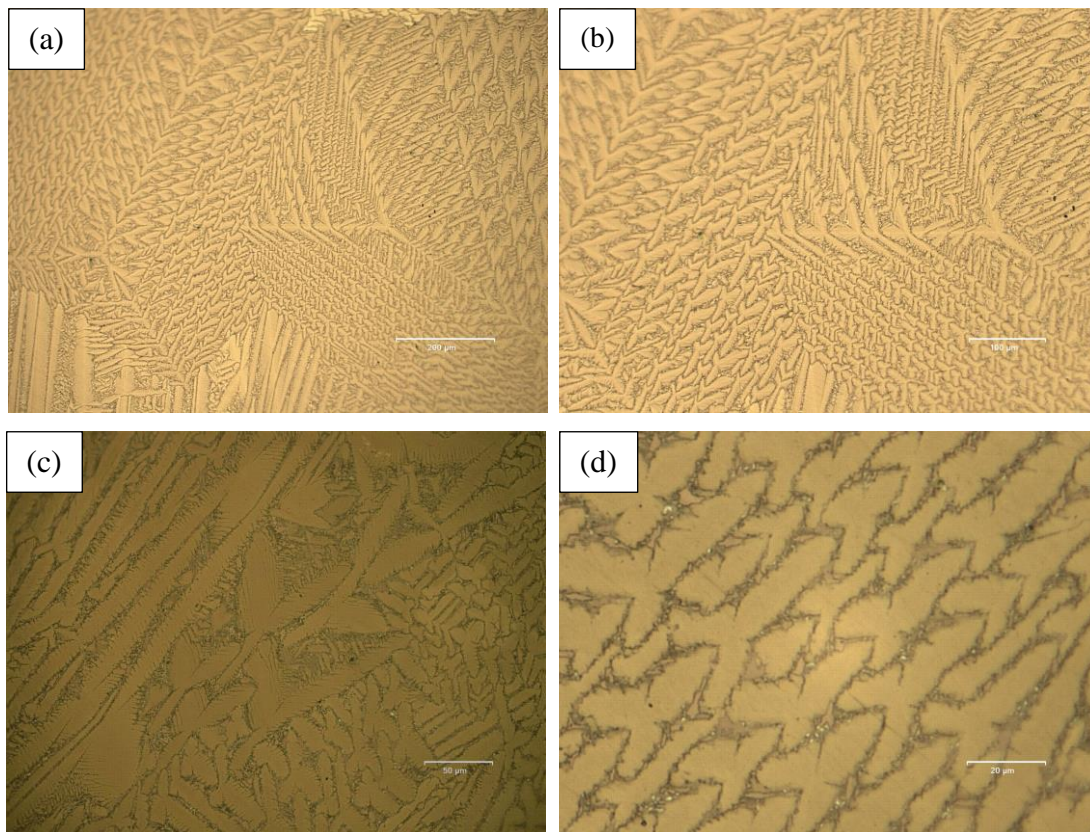


Figure 4.4 Optical microscope images of SC Alloy 1 with different scales (a) 200 μm , (b) 100 μm , (c) 50 μm , (d) 20 μm .

The microstructure of SC Alloy 1 contains dendritic primary phase with eutectic mixture containing intermetallic precipitates shown by yellow colored arrows 1, 2 and 3 respectively on Figure 4.5 (c). When Ti-Cu binary phase diagram given in Figure 4.1 examined together with the EDS results given in Table 4.5, it was found that eutectic structure could possibly be a mixture of Ti_2Cu and $TiCu$ phases. More detailed image of the eutectic region was shown in Figure 4.5 (d). Since the eutectic structure is very fine, detailed analysis could not be performed by means of FESEM analysis. On the other hand, primary dendritic structure is most probably Ti_2Cu phase containing Ni, Al, and V dissolved in it. The microstructure of SC Alloy 1 also comprises intermetallic phases as interdendritic particles which was analyzed as $TiAlCu_2$, indicated by arrow 3 in Figure 4.5 (c). Presence of this phase was also confirmed by XRD analysis. It was postulated that during solidification first L_{21} ordered $TiAlCu_2$ phase crystallized followed by hypoeutectic reaction [101].

The XRD result (Figure 4.6) shows that SC Alloy 1 contains three different phases as $\gamma TiCu$, Ti_2Cu and $TiAlCu_2$. These results are in agreement with the EDS (Table 4.5) analysis.

Table 4.5 EDS analysis for SC Alloy 1.

SC Alloy 1	at. % Ti	at. % Cu	at. % Ni	at. % Al	at. % V	Possible phase
Arrow 1	49.10	29.79	9.09	7.40	4.62	Primary Ti_2Cu
Arrow 2	47.62	38.17	8.54	4.42	1.25	$TiCu+Ti_2Cu$
Arrow 3	30.10	39.40	5.30	29.30	1.64	$TiAlCu_2$

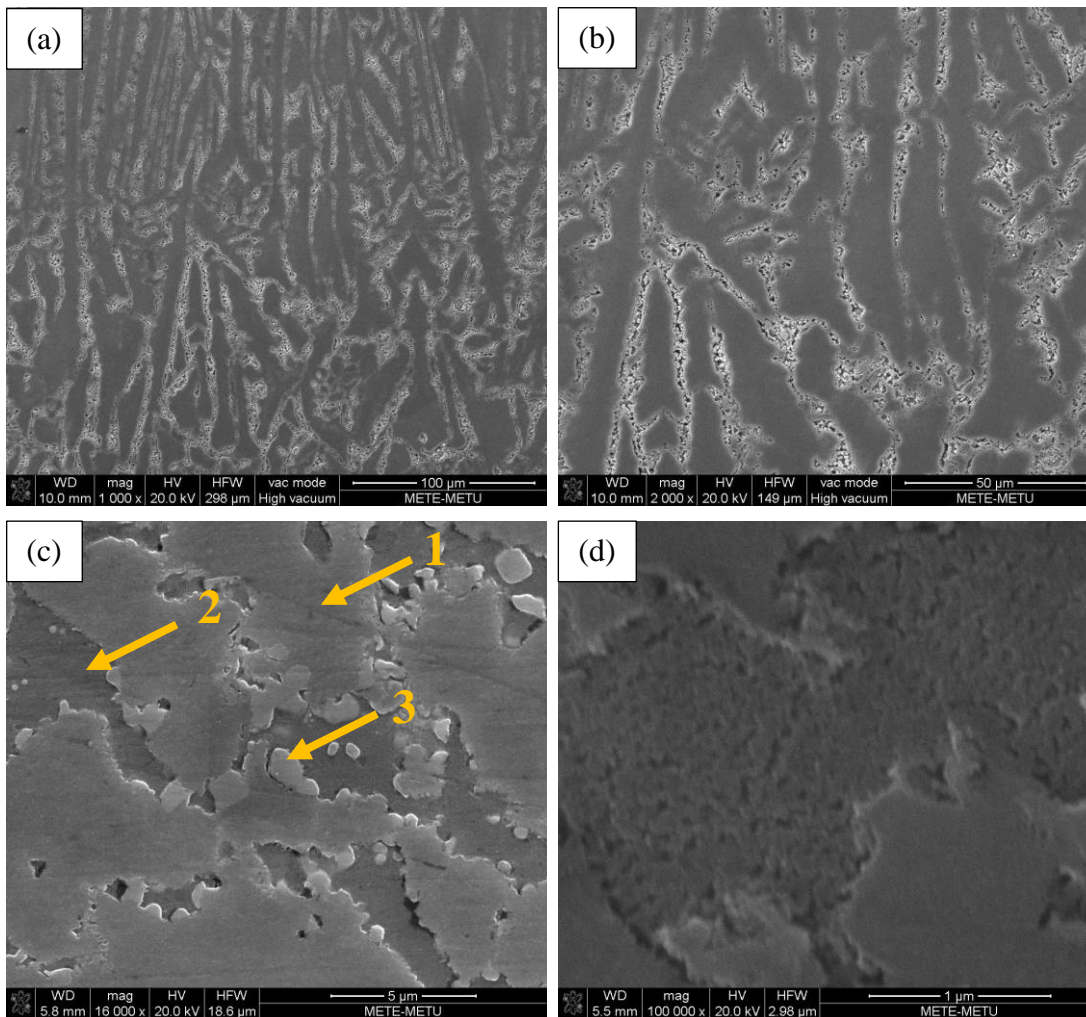


Figure 4.5 FESEM images of SC Alloy 1 in different magnifications (a) 1000x, (b) 2000x, (c) 16000x, (d) 100000x.

In addition to microstructural characterizations, thermal analysis was performed to investigate reactions as a result of heating. DSC heating curves are given in Figure 4.7. SC Alloy 1 contains a deep valley at 863°C which probably belong to melting at liquidus line. In addition to this, there are two exothermic peaks at 589°C and 693°C which may indicate a precipitation of some suppressed intermetallic phases during solidification. Solidification by arc melting process takes place under non-equilibrium conditions. Therefore, the second heating curve obtained after the first heating and

cooling cycle comprises reaction peaks different from the first heating curve. Second heating curve indicating that the sample melt through two endothermic reactions. Alloy start melting at 1034°C and finish the reaction around 1126°C

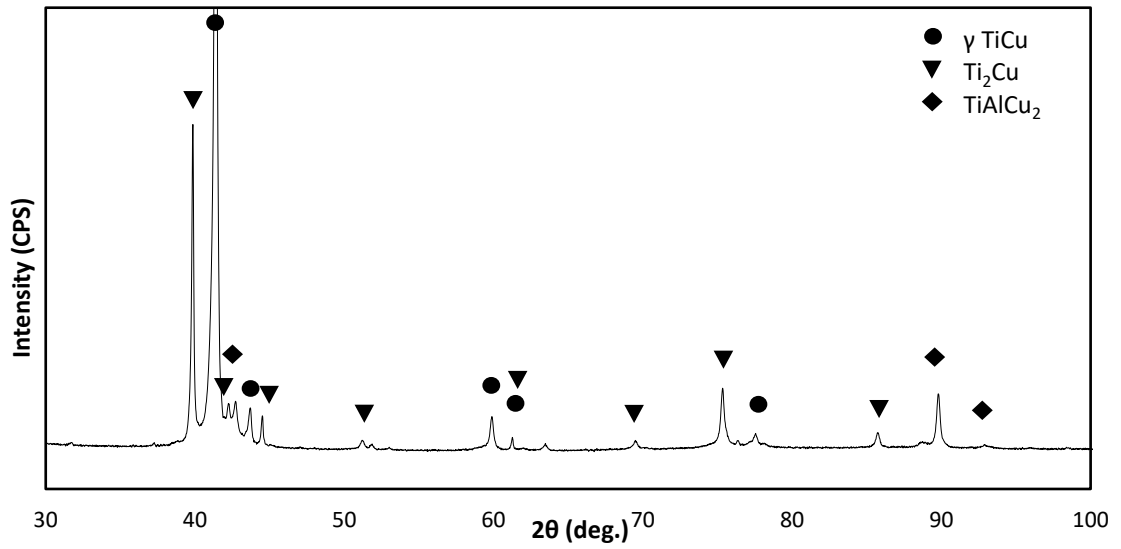


Figure 4.6 XRD pattern of SC Alloy 1.

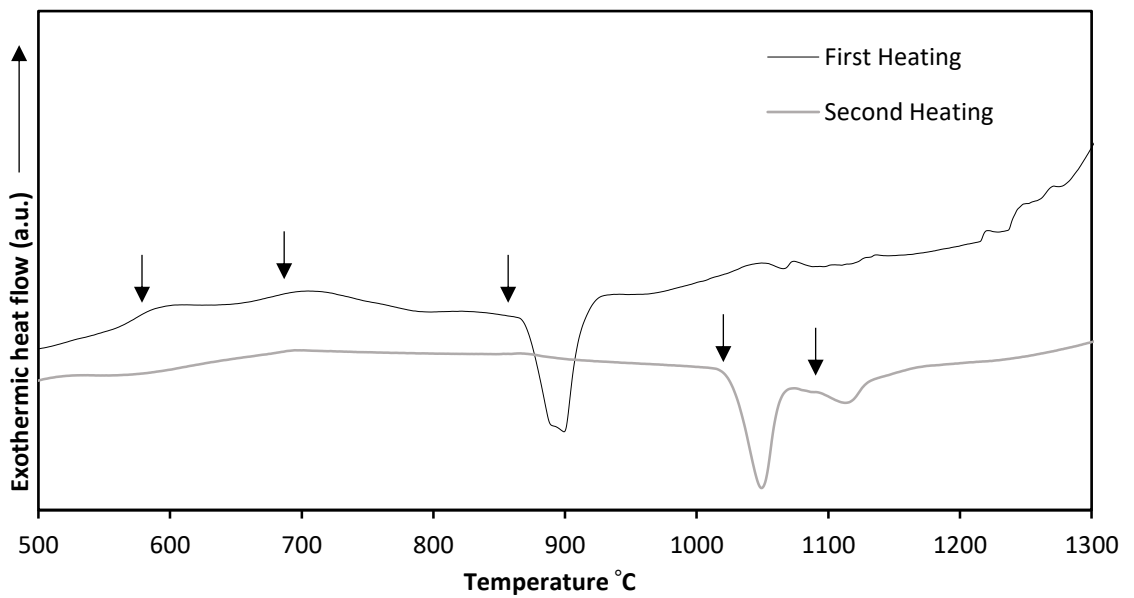


Figure 4.7 DSC heating curve of SC Alloy 1.

4.2.2. Fast Cooling Part of the Alloy 1

The solidification structure of FC Alloy 1 is different from that of the SC Alloy 1. Solidification starts as columnar growth at the outer zone of the sample where cooling rate is higher relative to the center of the sample. Subsequently, the solidification is completed by cellular growth mechanism. Detailed images of solidification are given in Figure 4.9 (a) and (b) where columnar and cellular dendritic solidification structures can be seen clearly. Furthermore, as can be seen from Backscattered-Electron (BSE) image of the sample (Figure 4.10 (b)), any compositional differences cannot be detected within the sample. That is to say, FC Alloy 1 consists of an only one phase. This is also confirmed by XRD results, solely γ TiCu phase can be identified from Figure 4.11. This implies that the Ti_2Cu and $TiAlCu_2$ were suppressed as the cooling rate was increased, Figure 4.12.

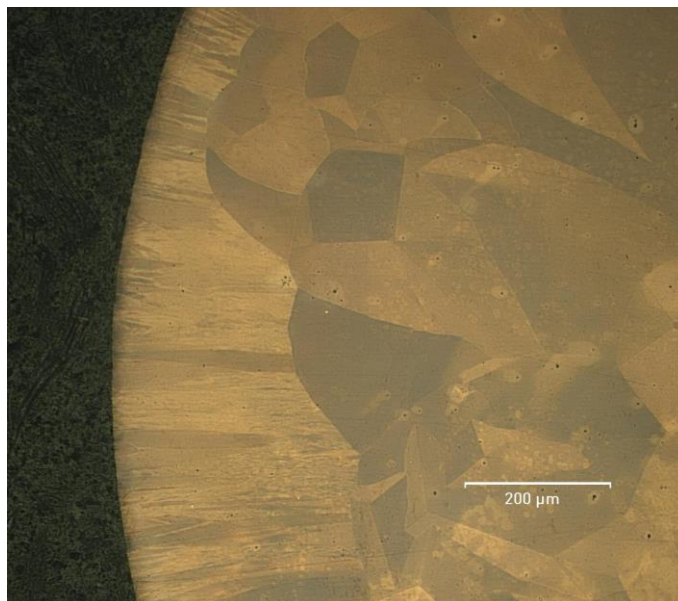


Figure 4.8 Optical microscope image of the FC Alloy 1.

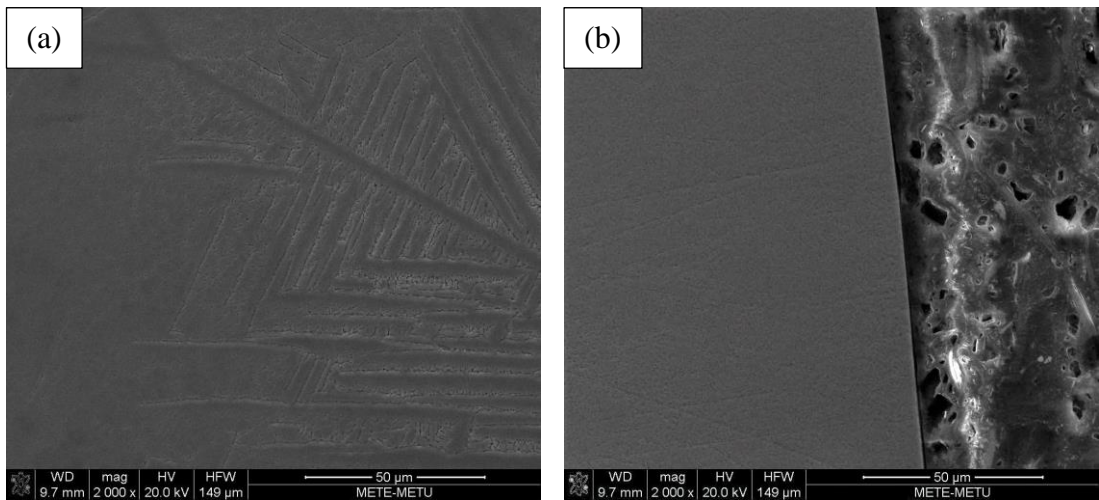


Figure 4.9 FESEM images of the FC Alloy 1, (a) center zone of the sample and (b) outer zone of the sample.

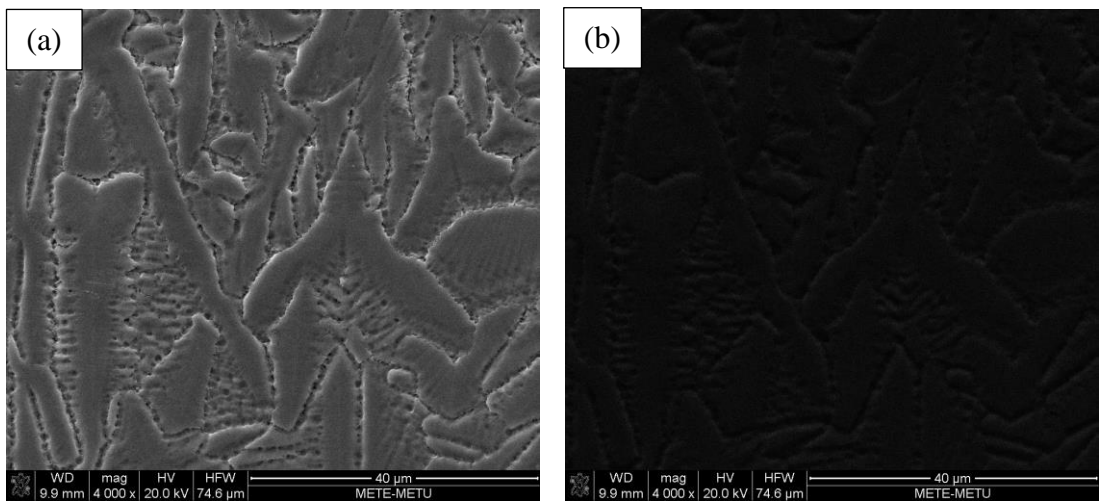


Figure 4.10 (a) Secondary-Electron image (SEI), (b) Backscattered-Electron (BSE) image of FC Alloy 1.

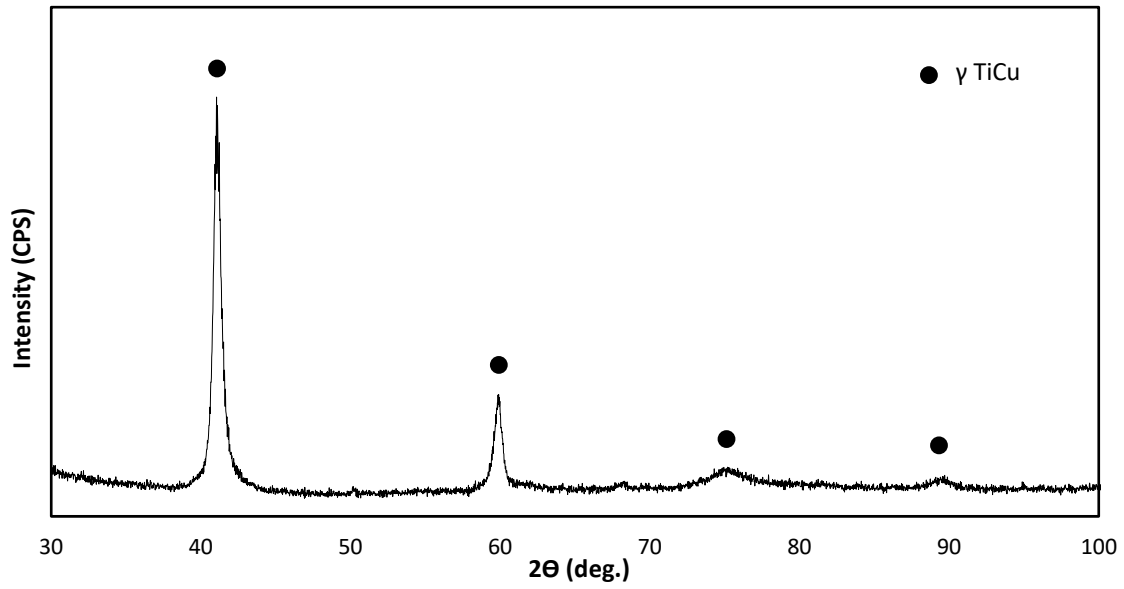


Figure 4.11 XRD pattern of FC Alloy 1.

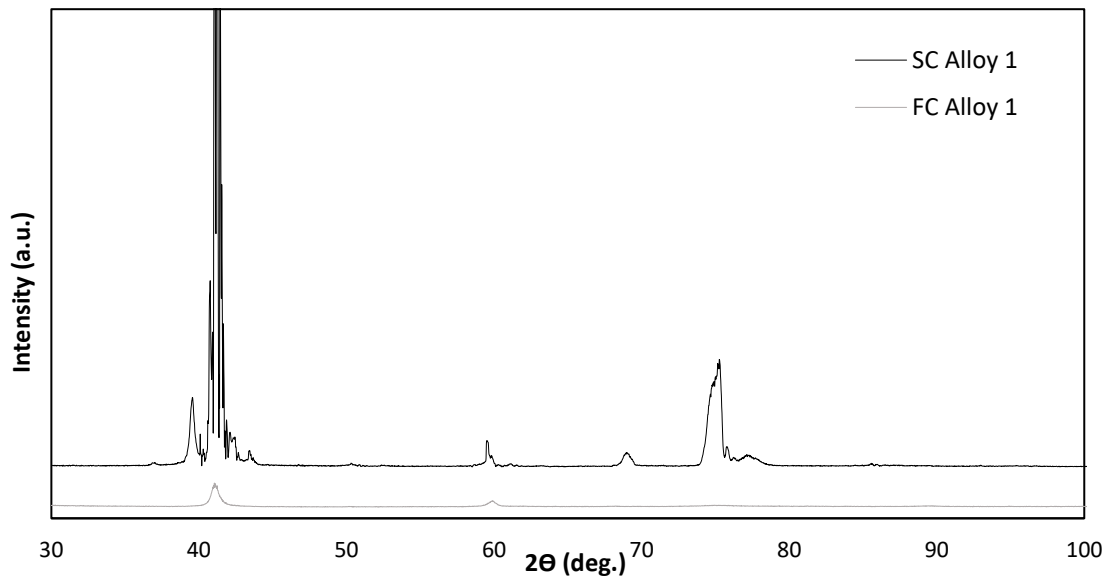


Figure 4.12 Comparative XRD pattern of FC Alloy 1 and SC Alloy 1.

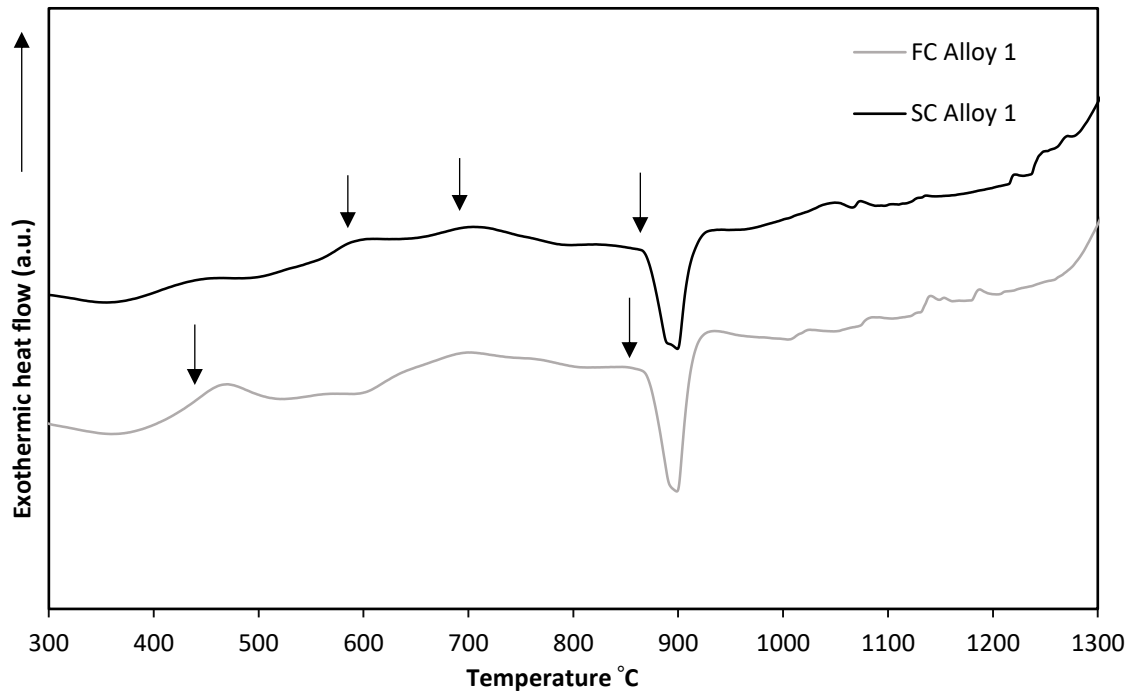


Figure 4.13 Comparative DSC heating curves for FC Alloy 1 and SC Alloy1.

Thermal analysis of SC Alloy 1 and FC Alloy 1 are given together in Figure 4.13. They were both found to contain endothermic peak at approximately the same temperature which most likely shows the melting. In addition to this peak, unlike SC Alloy 1, FC Alloy 1 contains an exothermic peak at 456 °C . This peak may belong to a precipitation reaction of suppressed phases due to higher cooling rate of the copper mold suction casting.

4.3. Characterization of Alloy 2 ($\text{Ti}_{47}\text{Cu}_{30}\text{Ni}_{10}\text{Al}_7\text{V}_5\text{Si}_1$)

4.3.1. Slow Cooling Part of the Alloy 2

Despite only atomic 1% of silicon content, microstructure of the SC Alloy 2 is noticeably different from that of the SC Alloy 1. In accordance with the optical microscope images given in Figure 4.14, the difference originates due to volume fraction of TiAlCu_2 phase. These intermetallic phases which were identified with EDS analysis can clearly be seen in Figure 4.14 (d) indicated with an arrow as light contrasted areas.

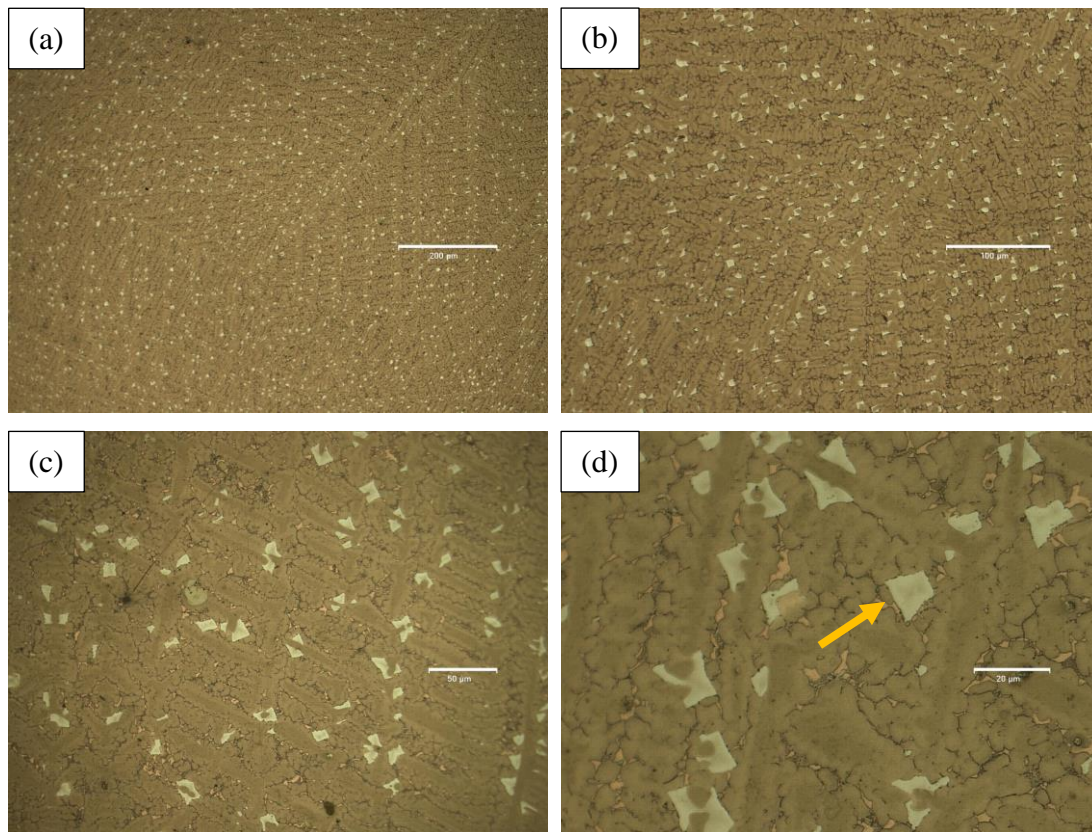


Figure 4.14 Optical microscope images of SC Alloy 2 with different scales (a) 200 μm, (b) 100 μm, (c) 50 μm, (d) 20 μm.

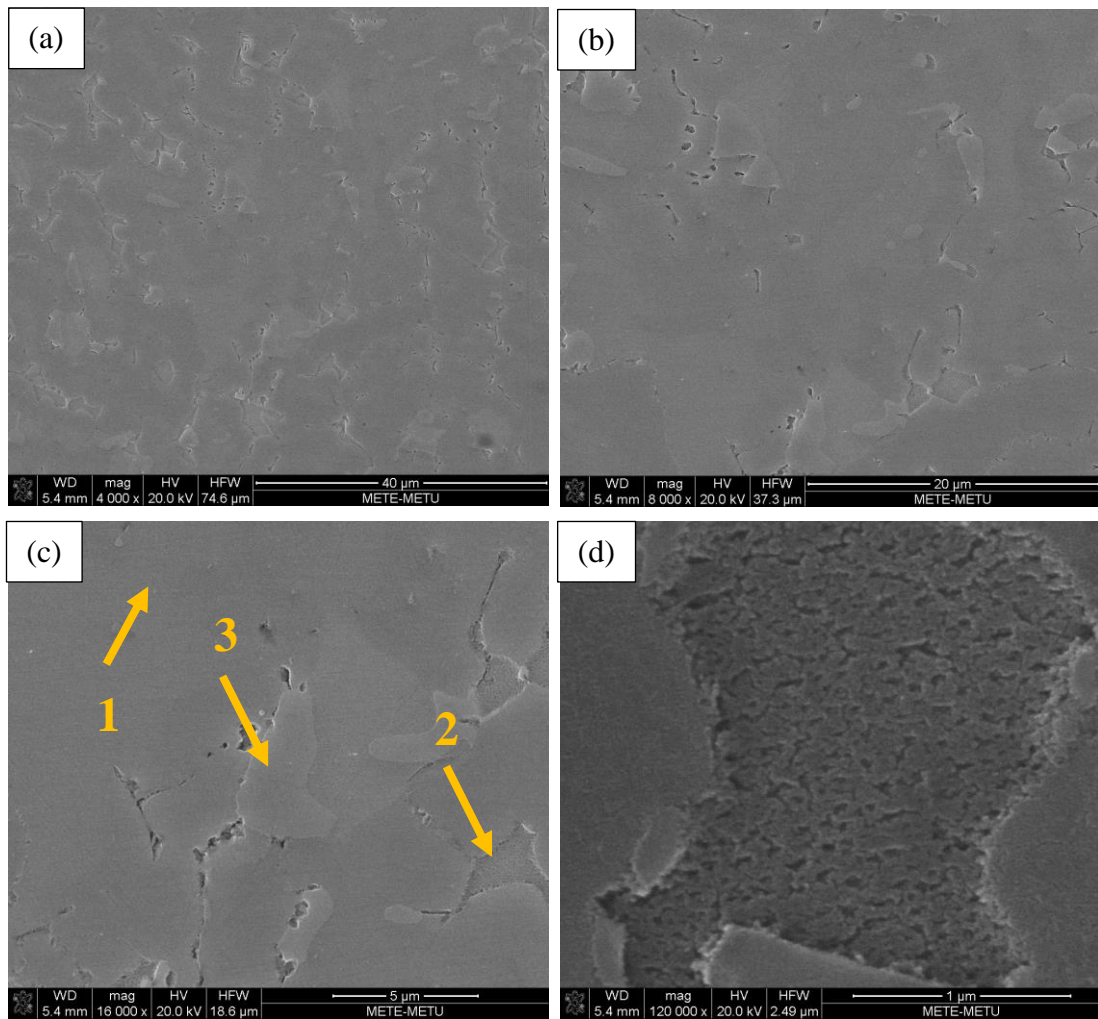


Figure 4.15 FESEM images of SC Alloy 2 in different magnifications (a) 4000x, (b) 8000x, (c) 16000x, (d) 120000x.

It is evident Figure 4.6 & Figure 4.16 that as SC Alloy 1 displays γ -TiCu, high intensity Ti_2Cu , and low intensity $TiAlCu_2$ peaks, while SC Alloy 1 shows γ -TiCu, low intensity Ti_2Cu and high intensity $TiAlCu_2$ peaks. This would tend to suggest that presence of Si favors the formation of large faceted $TiAlCu_2$ intermetallic particles indicated by arrow 3 in Figure 4.15 (c), distributed uniformly within the microstructure as shown in Figure 4.14. These intermetallic phases can also be

observed in SC Alloy 1 as fine interdendritic particles which were further identified by EDS analysis, Table 4.5.

Table 4.6 EDS analysis for SC Alloy 2.

SC Alloy 2	at. % Ti	at. % Cu	at. % Ni	at. % Al	at. % V	at. % Si	Possible phase
Arrow 1	32.63	41.19	7.45	6.55	4.11	1.16	Primary TiCu ₂
Arrow 2	53.46	40.76	4.36	5.57	1.77	1.43	TiCu+Ti ₂ Cu
Arrow 3	22.37	45.67	4.47	15.85	1.38	0.58	TiAlCu ₂

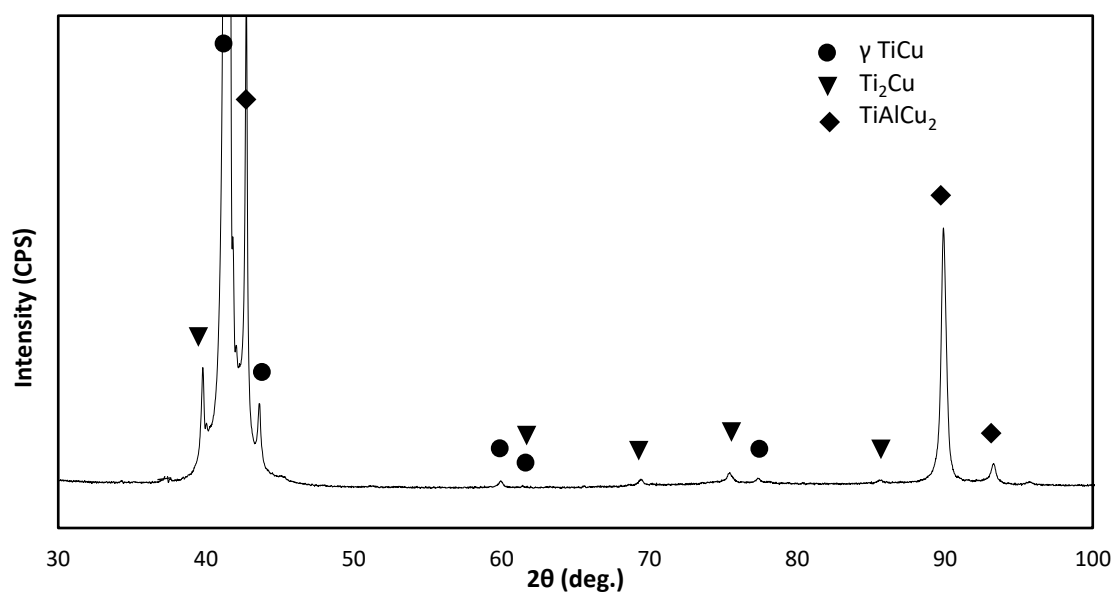


Figure 4.16 XRD pattern of SC Alloy 2.

4.3.2. Fast Cooling Part of the Alloy 2

Contrary to FC Alloy 1, presence of Si in the alloy composition leads to formation of approximately 40 μm in thickness amorphous phase at the surface of the suction casted rod where solidification rate significantly higher, Figure 4.17 Optical microscope image of FC Alloy 2. The cooling rate eventually decreases towards the center of the specimen and thus the variation of the cooling/solidification rate across the cross section of the specimen is accompanied by the structural transition from surface to center. The featureless zone implying the presence of the amorphous phase at the surface undergoes crystallization process at a certain thickness and display cellular growth morphology. Where the solidification starts is indicated by an arrow in Figure 4.18 (b). This plane growth solidification structures survive until the solid liquid interface is subjected to morphological instability where cellular and/or dendritic solidification is observed towards the center of the specimen.

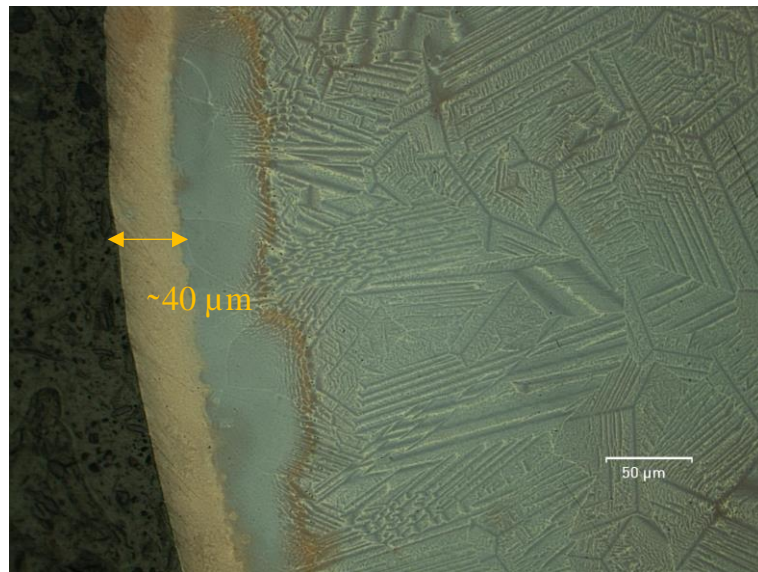


Figure 4.17 Optical microscope image of FC Alloy 2.

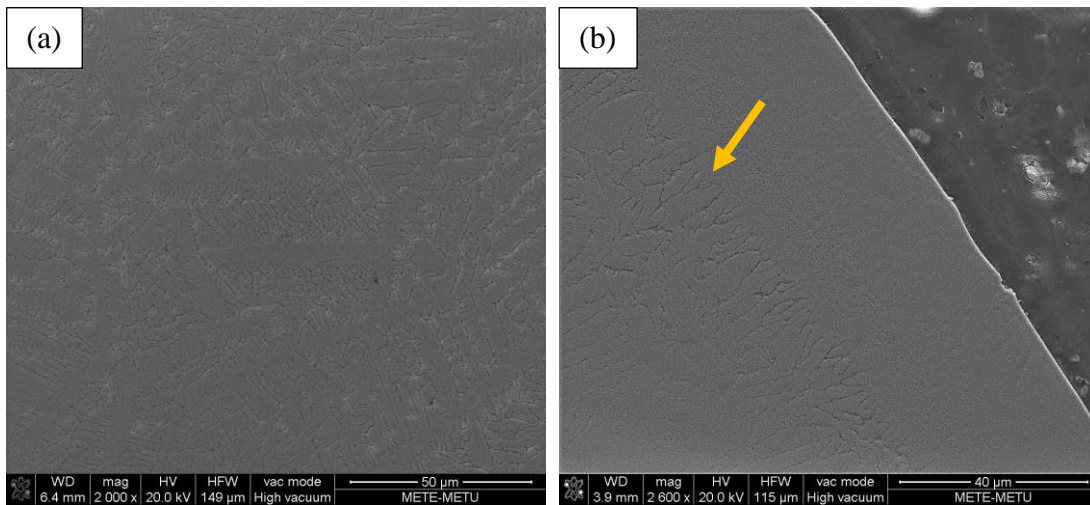


Figure 4.18 FESEM images of FC Alloy 2, (a) center zone of the sample and (b) outer zone of the sample.

Same as FC Alloy 1, FC Alloy 2 also was analyzed to comprise only one phase which is γ TiCu, Figure 4.19. In addition, the formation of the Ti_2Cu , and $TiAlCu_2$ phases were suppressed in the same manner as the FC Alloy 1, Figure 4.20.

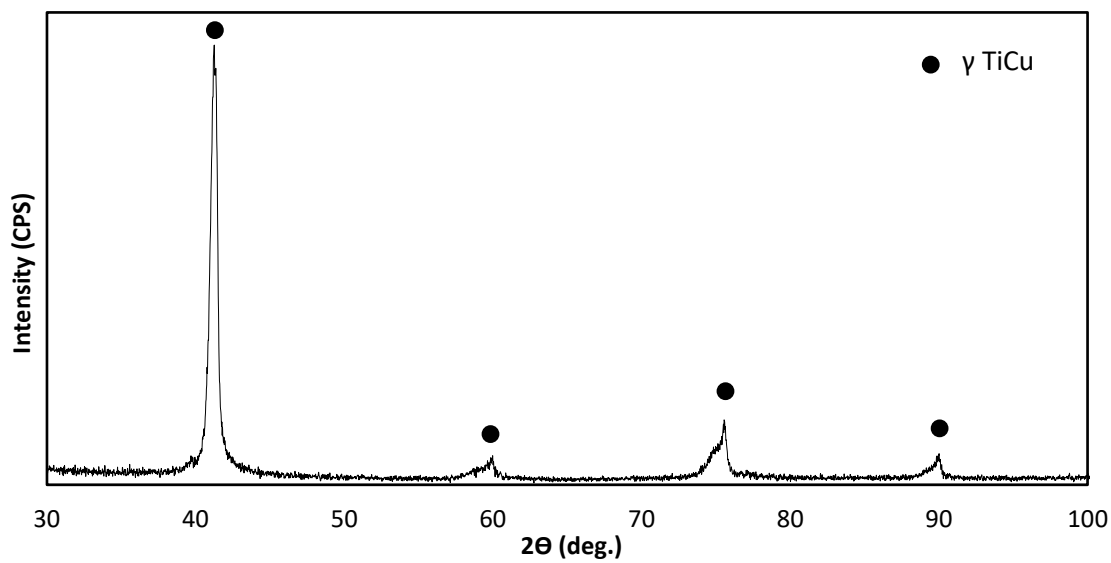


Figure 4.19 XRD pattern of FC Alloy 2.

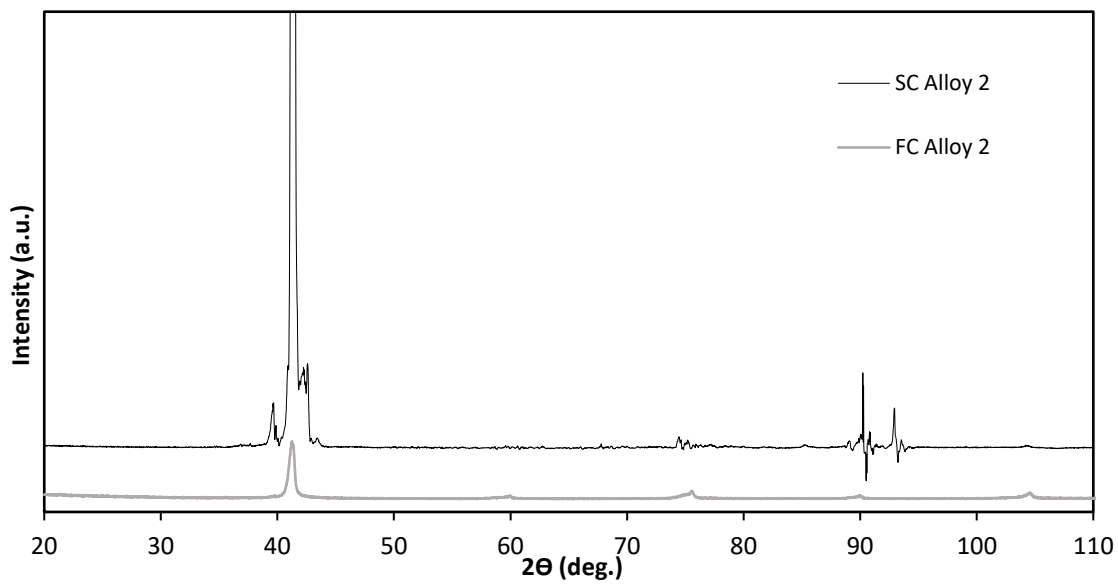


Figure 4.20 Comparative XRD pattern of FC Alloy 2 and SC Alloy 2.

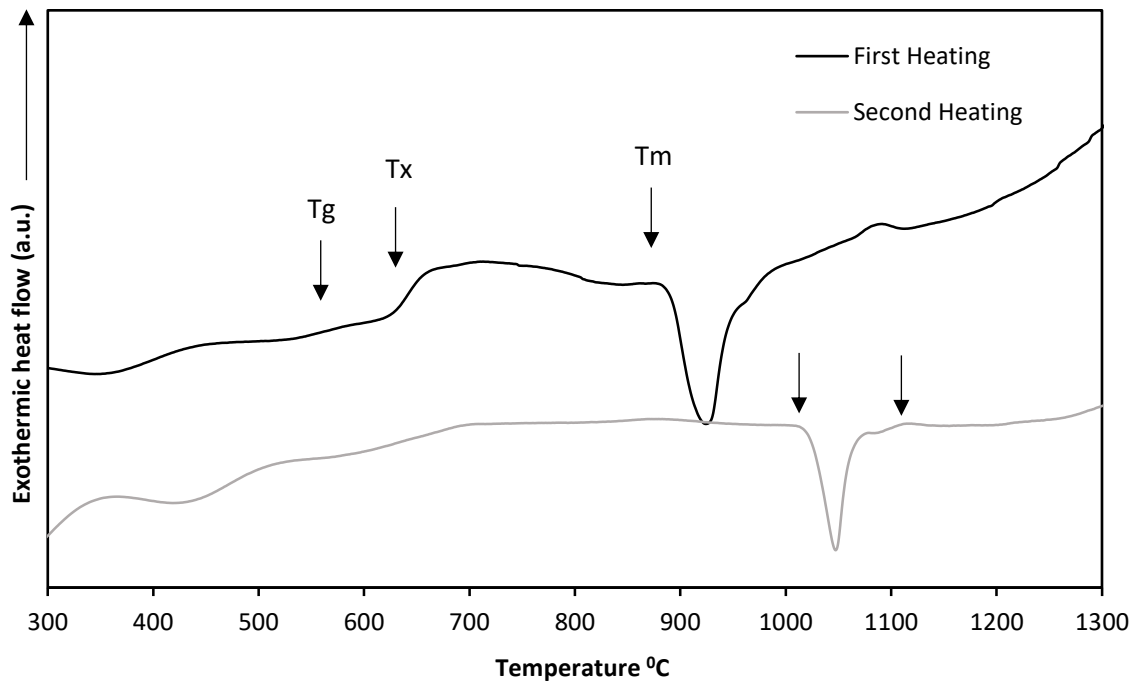


Figure 4.21 DSC heating curves for FC Alloy 2.

The amorphous nature of the outer zone of the FC Alloy 2 was further confirmed by thermal analysis. First heating curve of the sample is given in Figure 4.21 shows a glass transition and a crystallization reaction. The glass transition temperature and the crystallization temperature were found to be 591°C and 627°C, respectively. This would suggest that the alloy has a wide supercooled liquid region. First heating curve provides information about the glass transition and following crystallization of the amorphous structure while the second heating curve shows the melting of as-crystallized phases during first cooling. As-crystallized sample starts melting at 1024°C and finishes at 1110°C. Any glass transition or crystallization reactions were not observed during second heating due to the slower cooling rate of the first cooling stage.

4.4. Characterization of Alloy 3 ($\text{Ti}_{48}\text{Cu}_{30}\text{Ni}_{10}\text{Al}_7\text{V}_5$) $_{97}\text{Si}_3$

4.4.1. Slow Cooling Part of the Alloy 3

Alloy composition ($\text{Ti}_{48}\text{Cu}_{30}\text{Ni}_{10}\text{Al}_7\text{V}_5$) $_{97}\text{Si}_3$ was synthesized for the further investigation of Si addition. As clearly can be seen from optical microscope images given in Figure 4.22, microstructure of SC Alloy 3 is completely different from that of SC Alloy 1 and SC Alloy 2. The microstructure of SC Alloy 3 was analyzed to contain different crystal structures at different part of the samples. At the top of the spherical sample where solidification rate is relatively slower than the bottom of the sample, dendritic structures was observed. In addition to these, faceted intermetallic phases are found to evenly distributed within the sample.

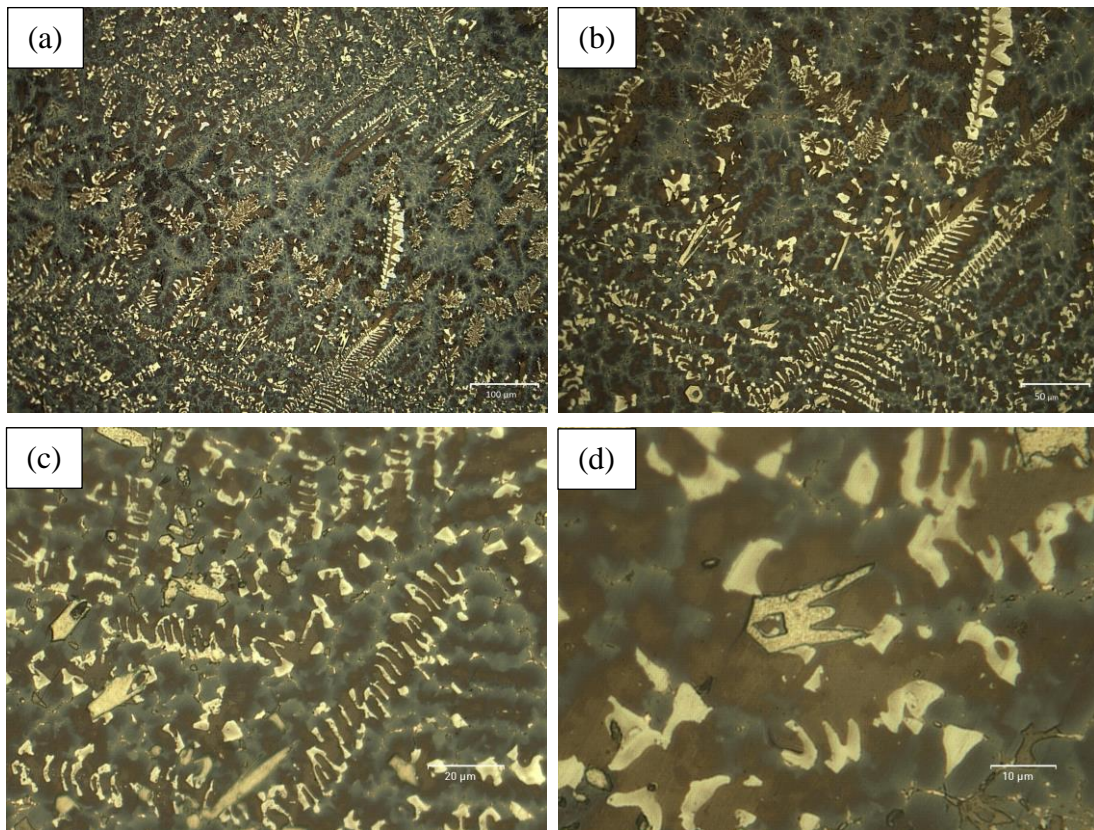


Figure 4.22 Optical microscope images of SC Alloy 3 with different scales (a) 100 μm , (b) 50 μm , (c) 20 μm , (d) 10 μm .

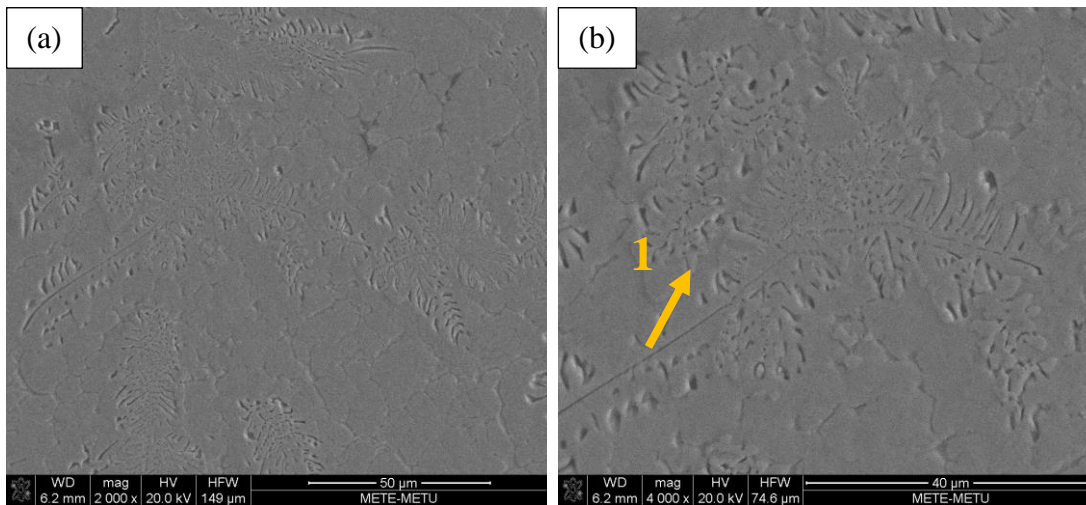


Figure 4.23 Chinese script structures found in SC Alloy 3.

After further investigation with FESEM and EDS analysis given in Figure 4.23 and Table 4.7 respectively, these Chinese script structures were suggested that may be a primary complex intermetallic of Ti, Cu, and Si. However, these intermetallics could not be detected with XRD analysis due to their low volume fraction. Apart from complex intermetallic of Ti, Cu, Si another different phase which was not found in Alloy 1 and Alloy 2 are detected. This hexagonal shaped phase given in Figure 4.24 (c) and detailed image of this phase is given in Figure 4.24 (d). As can be clearly seen from figures there are hexagonal shaped two-phase mixture and a white contrasted phase in the middle. This would suggest that this structure was formed by peritectic reaction which includes transformation of one solid phase and liquid phase into a different solid phase. Depending on the EDS analysis given in , when Ti-Cu-Si ternary system (Figure 4.26) is examined it is seen that pseudobinary peritectic reaction $L + Ti_2Cu \rightarrow Ti_5Si_3 + TiCu$ at $935^\circ C$ is likely to occur [102]. According to the peritectic reaction this would suggest that white contrasted phase which is Ti_2Cu considering Ti-Cu-Si ternary phase diagram, crystallized first and after that the liquid phase nearer to the Ti_2Cu crystallized into two phase mixture which are Ti_5Si_3 and $TiCu$ phases.

For further investigation of the structure, EDS mapping analysis was performed, Figure 4.27 and also Backscattered-Electron (BSE) image was taken, Figure 4.25.

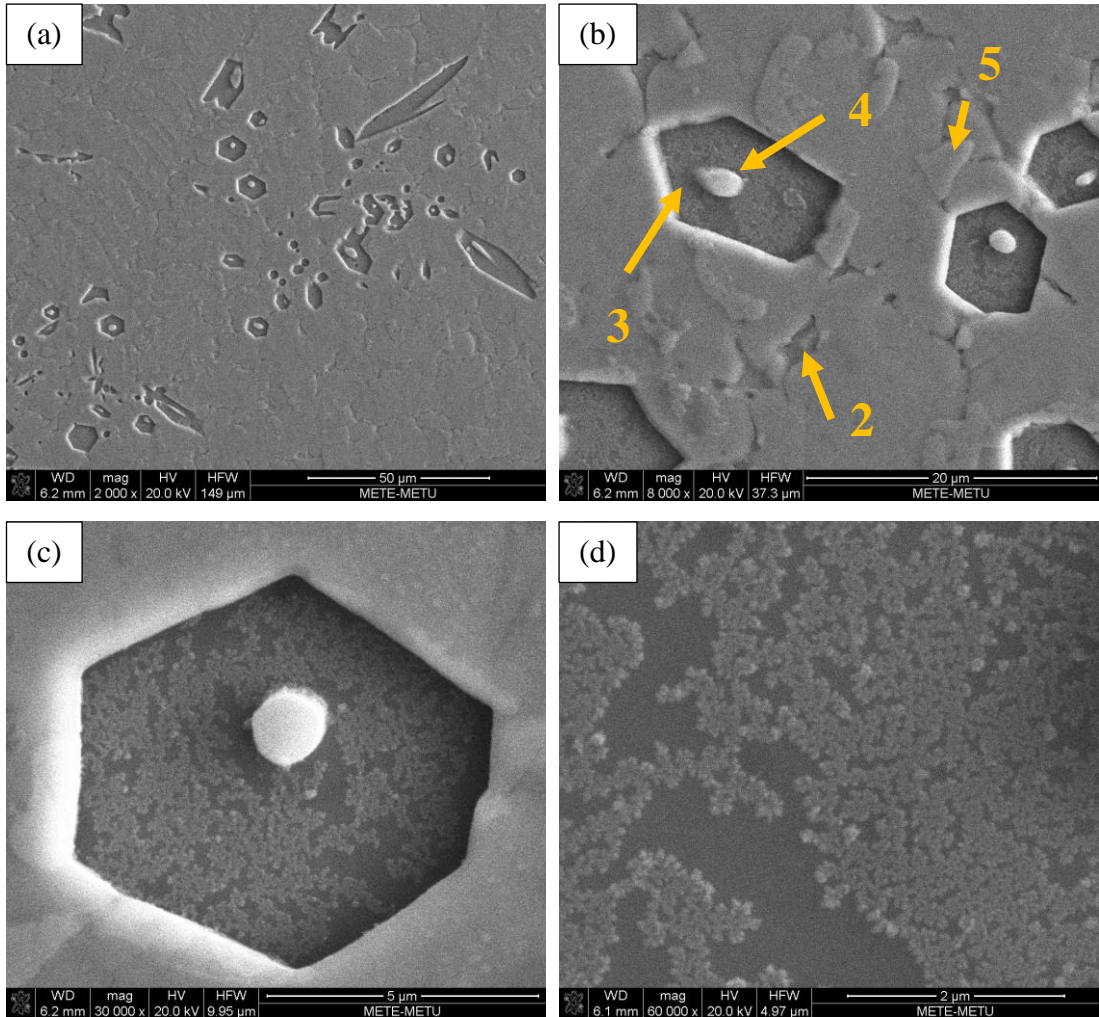


Figure 4.24 FESEM images of SC Alloy 3 in different magnifications (a) 50 μm , (b) 20 μm , (c) 5 μm , (d) 2 μm .

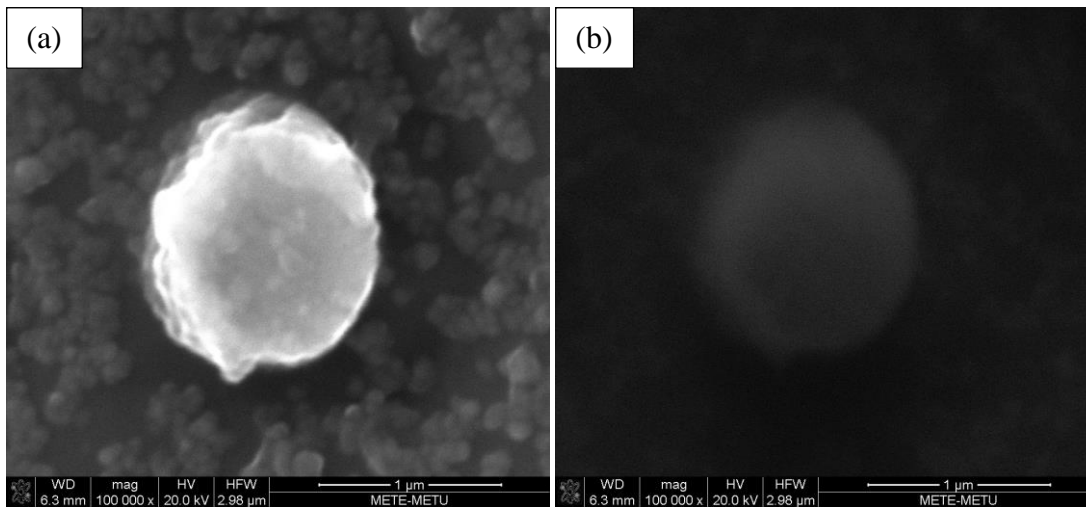


Figure 4.25 Secondary-Electron image (SEI), (b) Backscattered-Electron (BSE) image of SC Alloy 3.

Backscattered electron images confirm that white contrasted spheroidal phase and light grey areas in the two-phase structure are copper-rich phases. Due to copper's higher atomic number relative to the other alloying elements Ti_2Cu and $TiCu$ phases look brighter. In addition to this, eds mapping images given in Figure 4.27 also show that white contrasted spheroidal phase is rich in copper.

Table 4.7 EDS analysis for SC Alloy 3.

SC Alloy 3	at. % Ti	at. % Cu	at. % Ni	at. % Al	at. % V	at. % Si	Possible phase
Arrow 1	48.33	23.19	6.35	3.28	3.92	14.92	Complex Ti-Cu-Si intermetallics
Arrow 2	47.62	38.17	8.54	4.42	1.25	-	$TiCu+Ti_2Cu$
Arrow 3	51.05	4.81	1.53	2.18	6.34	34.09	$Ti_5Si_3 + TiCu$

Arrow 4	45.78	23.86	7.10	6.37	4.62	12.27	Ti ₂ Cu
Arrow 5	25.65	36.20	11.99	28.70	0.95	0.51	TiAlCu ₂

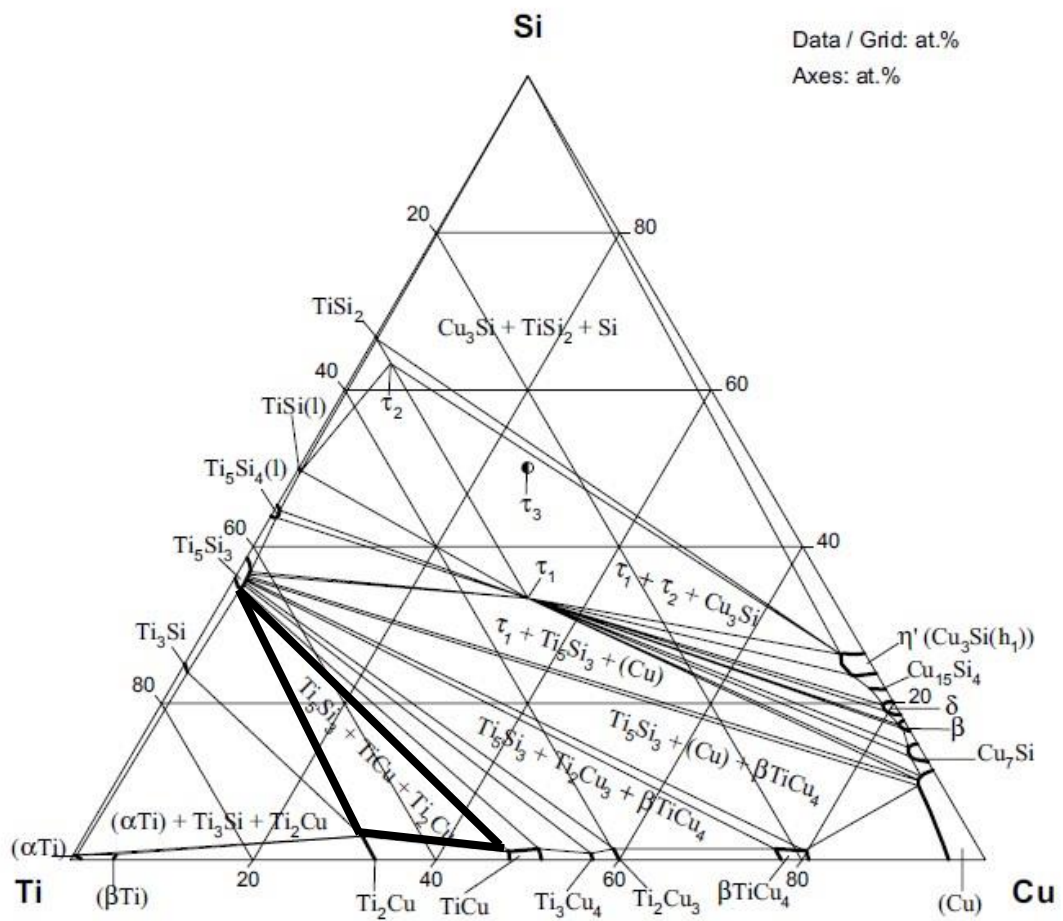


Figure 4.26 Ti-Cu-Si ternary phase diagram isothermal section at 800°C [103].

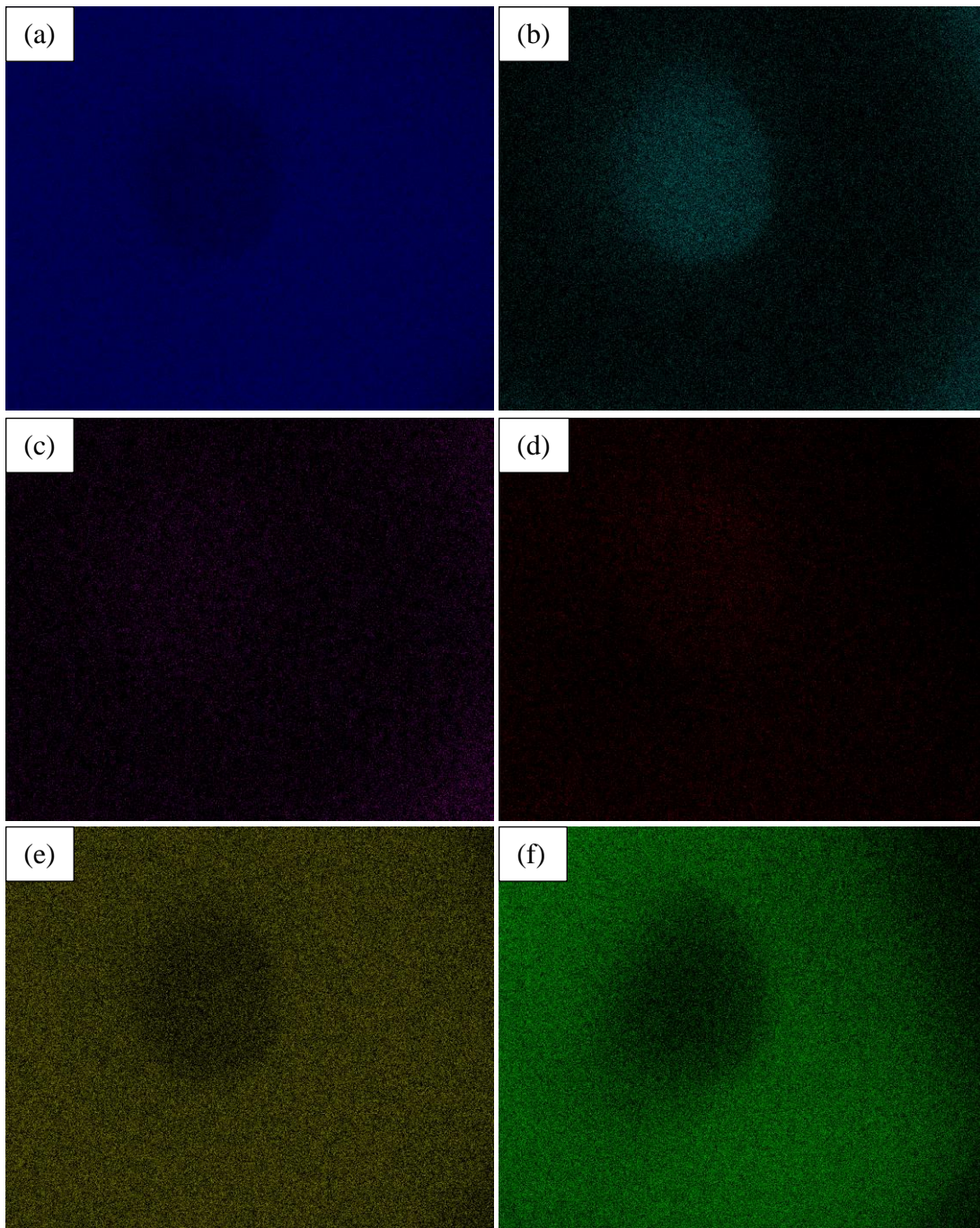


Figure 4.27 EDS mapping analysis of SC Alloy 3 showing elemental distribution of, (a) Ti, (b) Cu, (c) Ni, (d) Al, (e) V, and (f) Si.

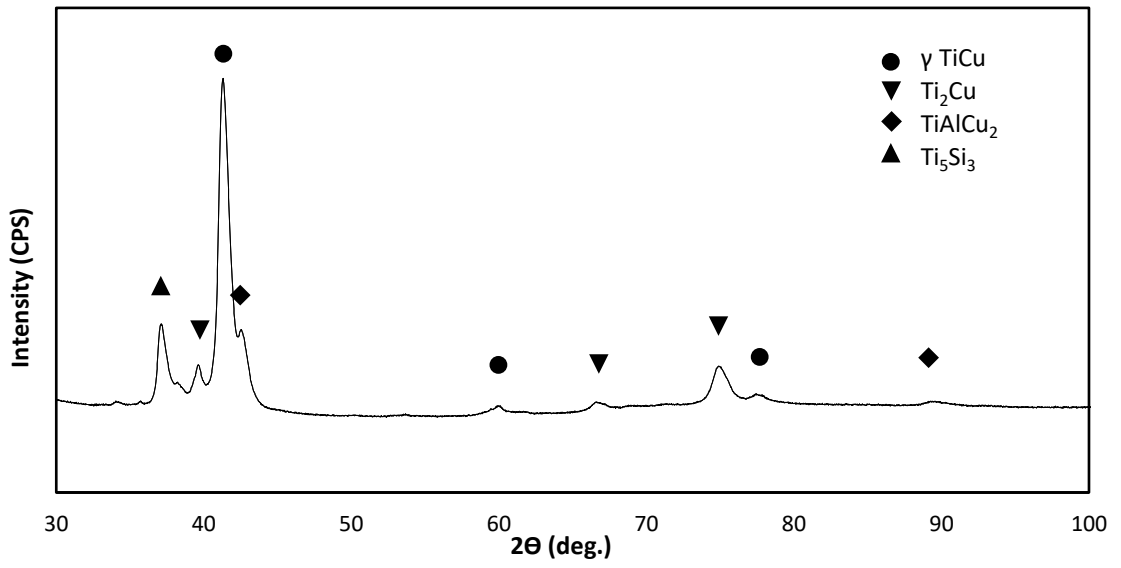


Figure 4.28 XRD pattern of SC Alloy 3.

4.4.2. Fast Cooling Part of the Alloy 3

When the optical microscope image given in Figure 4.29 is examined, it is seen that there is no structural difference in SC Alloy 3 from FC Alloy 3 except primary complex intermetallics of Ti, Cu, and Si. FC Alloy 3 has the same pseudobinary peritectic reaction ($L + \text{Ti}_2\text{Cu} \rightarrow \text{Ti}_5\text{Si}_3 + \text{TiCu}$) structure as can be clearly seen from Figure 4.30 and EDS analysis, Table 4.8. It is also another indication of the fact that the XRD analysis includes the same diffraction peaks for both samples which are γ TiCu, Ti_2Cu , TiAlCu_2 , and Ti_5Si_3 , (Figure 4.32). Crystallization was initiated at the outer region of the sample and TiAlCu_2 intermetallics together with peritectic reaction phases Ti_2Cu , TiCu, and Ti_5Si_3 are present as the intermetallic precipitate phase in the matrix. According to these results, it can be stated that the cooling rate did not provide amorphous formation in this composition.

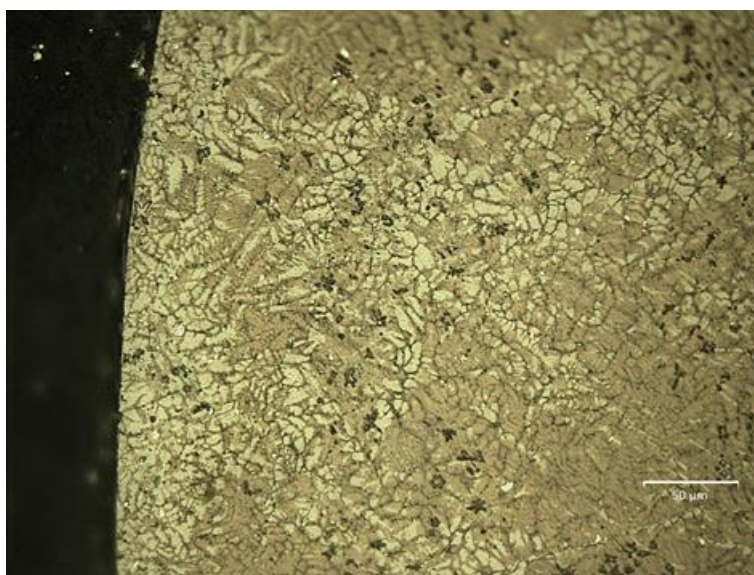


Figure 4.29 Optical microscope image of FC Alloy 3.

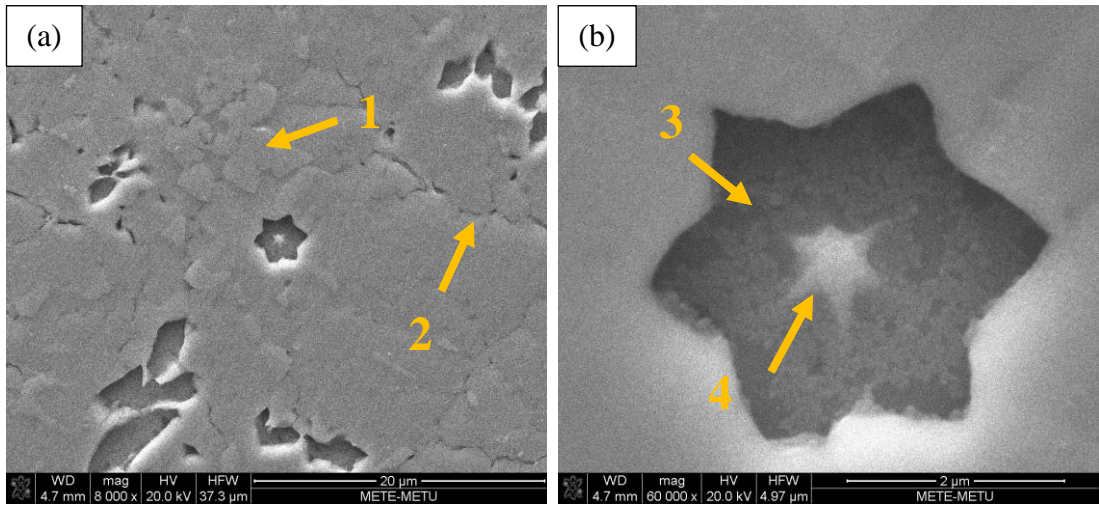


Figure 4.30 FESEM images of FC Alloy 3.

Table 4.8 EDS analysis for FC Alloy 3.

FC Alloy 3	at. % Ti	at. % Cu	at. % Ni	at. % Al	at. % V	at. % Si	Possible phase
Arrow 1	21.99	34.21	13.99	27.35	0.61	0.85	TiAlCu ₂
Arrow 2	48.92	39.20	8.51	4.32	1.38	-	TiCu+Ti ₂ Cu
Arrow 3	50.46	16.74	4.87	2.58	4.97	20.38	Ti ₅ Si ₃ +TiCu
Arrow 4	43.02	19.49	6.39	6.67	4.13	20.30	Ti ₂ Cu

The high enthalpy of mixing between Ti and Si (-49 kJ/mol [100]) induced the formation of Ti₅Si₃ phase, which was also detected by XRD analysis, Figure 4.31.

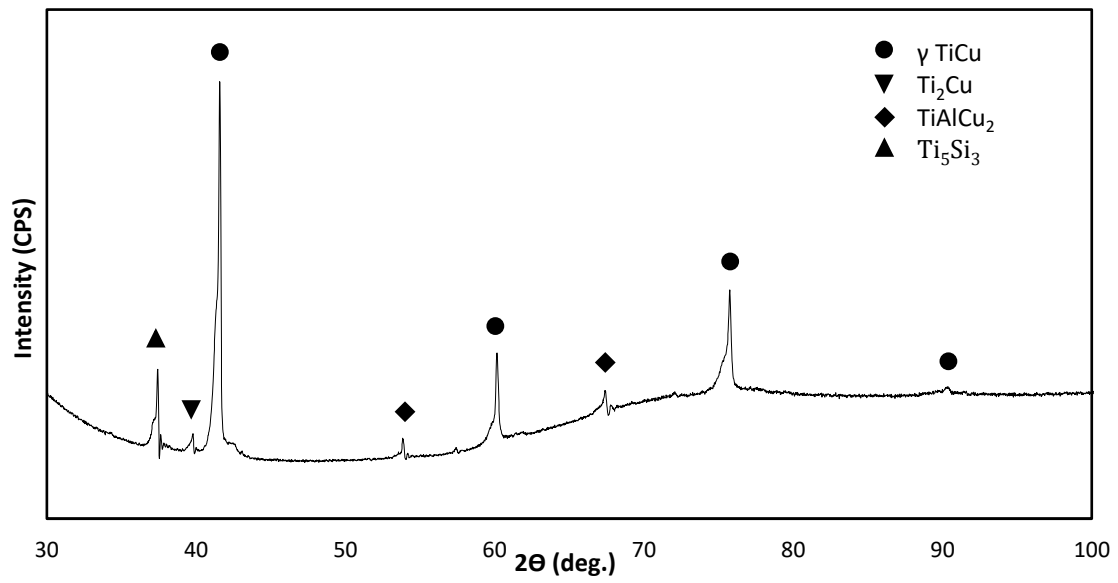


Figure 4.31 XRD pattern of FC Alloy 3.

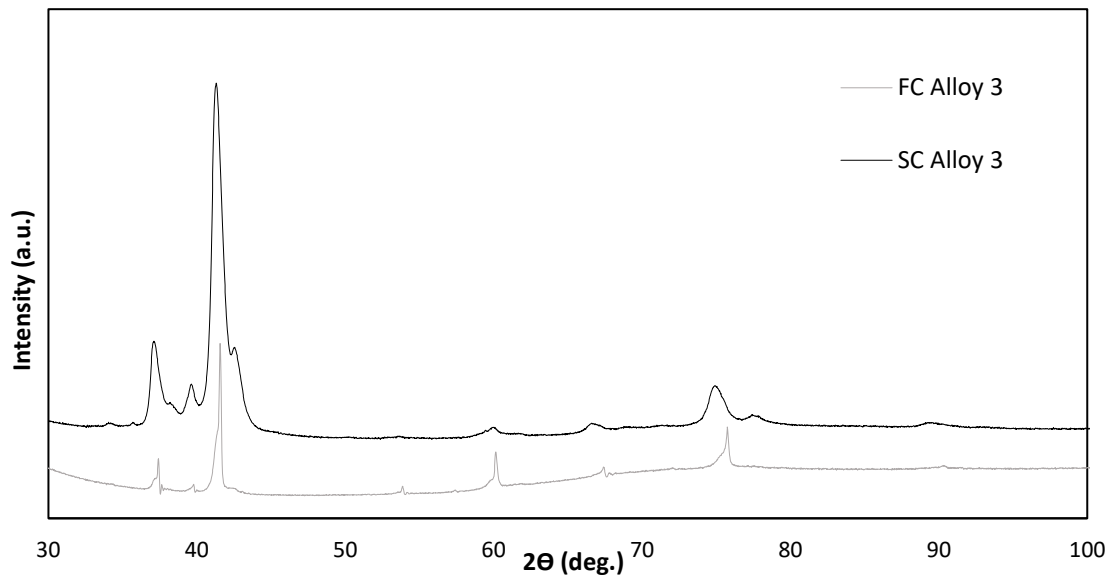


Figure 4.32 Comparative XRD pattern of fast cooling part of the Alloy 3 and Slow cooling part of the Alloy 3.

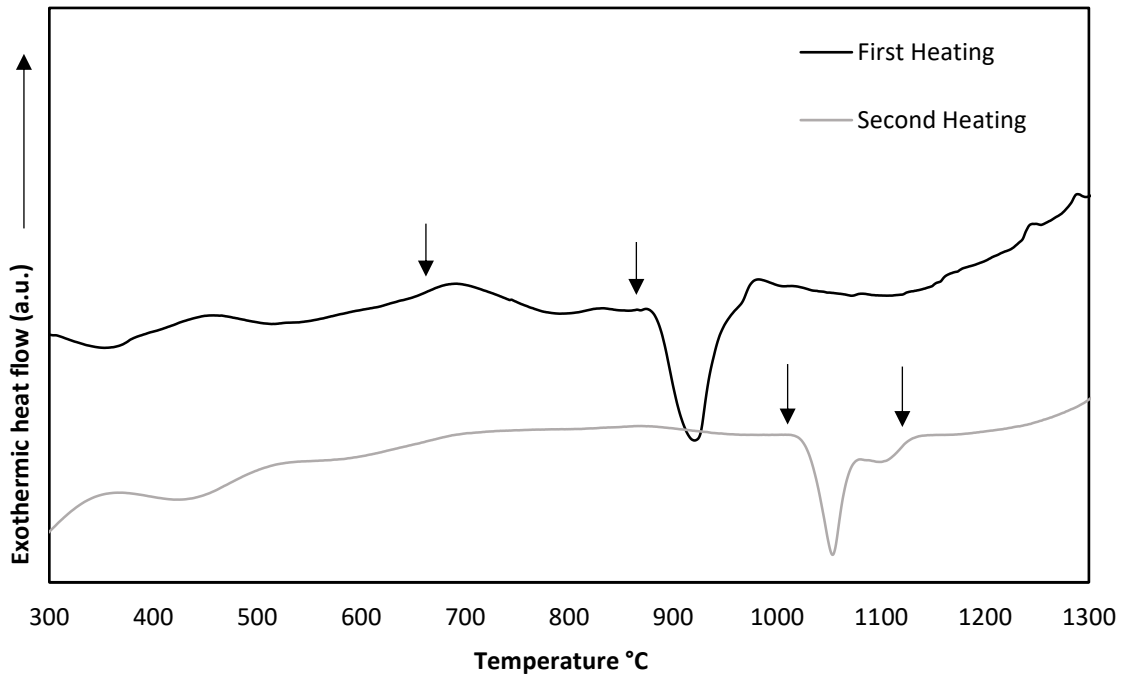


Figure 4.33 DSC Heating Curves for FC Alloy 3.

DSC heating curves of FC Alloy 3 are given in Figure 4.32. It was found to contain an endothermic peak at 932 °C which most likely belongs to the melting reaction. additionally, it contains an exothermic peak at 681 °C. And again, this peak may belong to a precipitation reaction of avoided phases during solidification. The only microstructural difference between SC Alloy 3 and FC Alloy 3 is the some complex intermetallics of Ti, Cu, and Si. Thus, this reaction may represent the precipitation reaction of these phases.

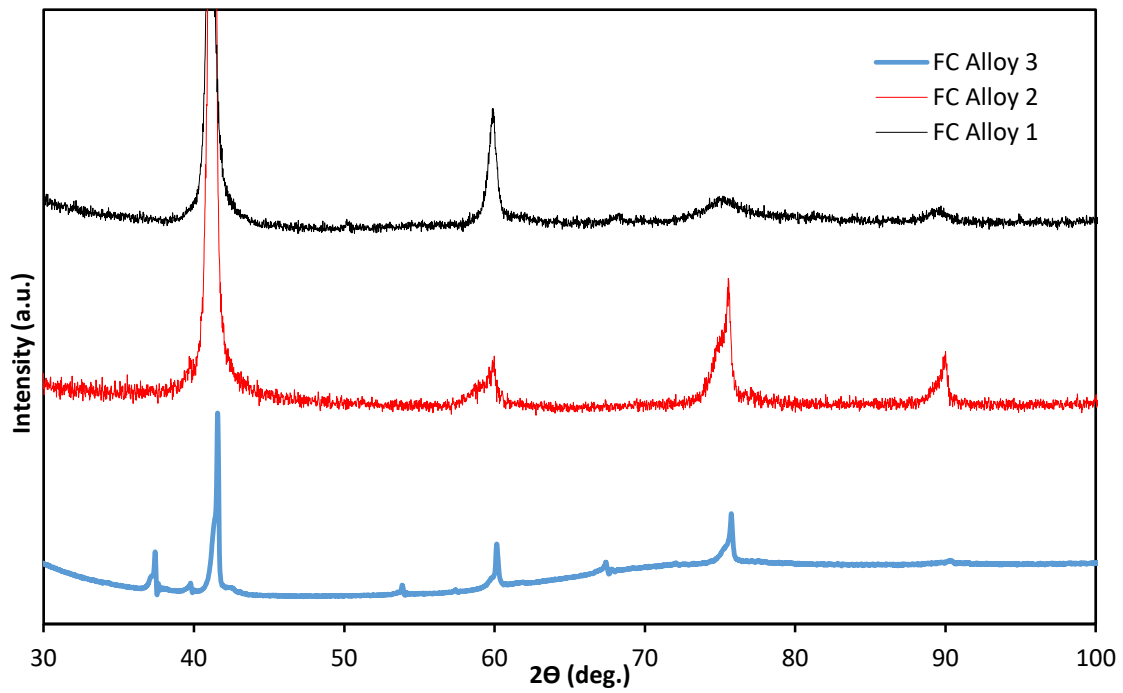


Figure 4.34 Comparative XRD patterns of fast cooling part of the Alloy 1, Alloy 2, and Alloy 3.

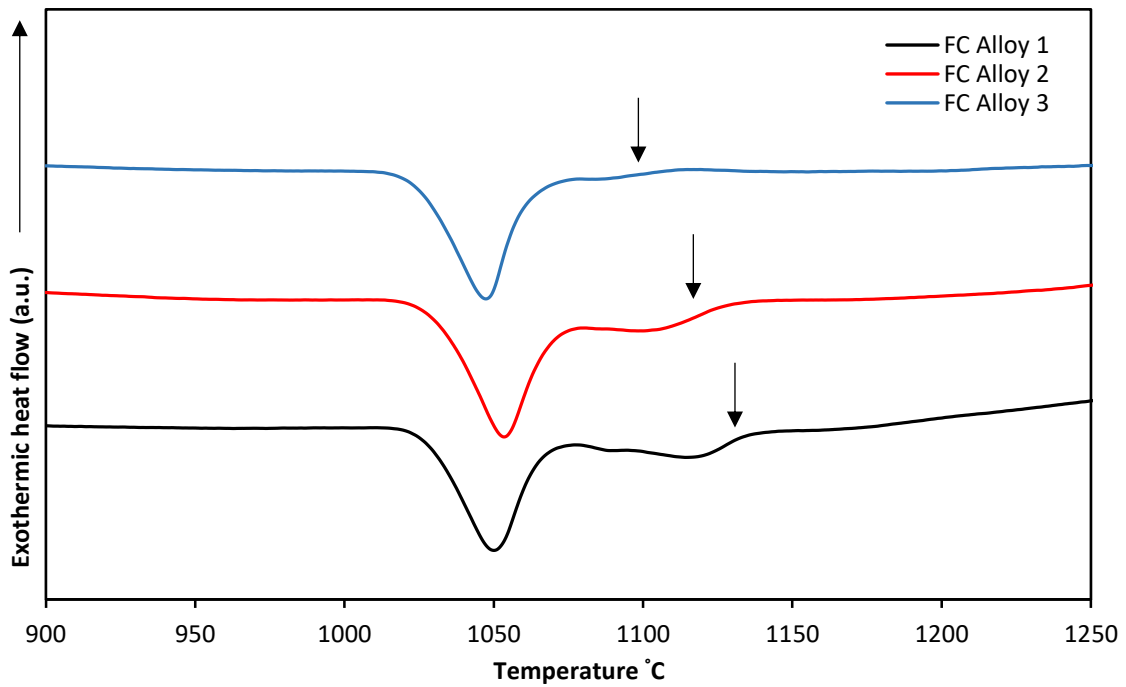


Figure 4.35 Comparative DSC heating curves of FC Alloy 1, Alloy 2, and Alloy 3.

Comparative DSC curves for three different alloy systems is given in Figure 4.35 and the liquidus temperature indicated by an arrow. As can be seen from the figure, the addition of Si lowered the melting temperatures, indicating higher liquid phase stability. This effect results from the large difference in atomic size of Si when compared with Ti, Table 4.3 [100]. This difference possibly improves the short-range order and provides a densely packed liquid structure, which may obstruct the crystallization and therefore increase the GFA. On the other hand, Si addition larger than 1 at. % induce the formation of Ti_5Si_3 intermetallic phases, Figure 4.34. Due to the higher liquidus temperature of Ti_5Si_3 , this phase first forms during solidification and acts nucleation sites and consequently triggers crystallization [102].

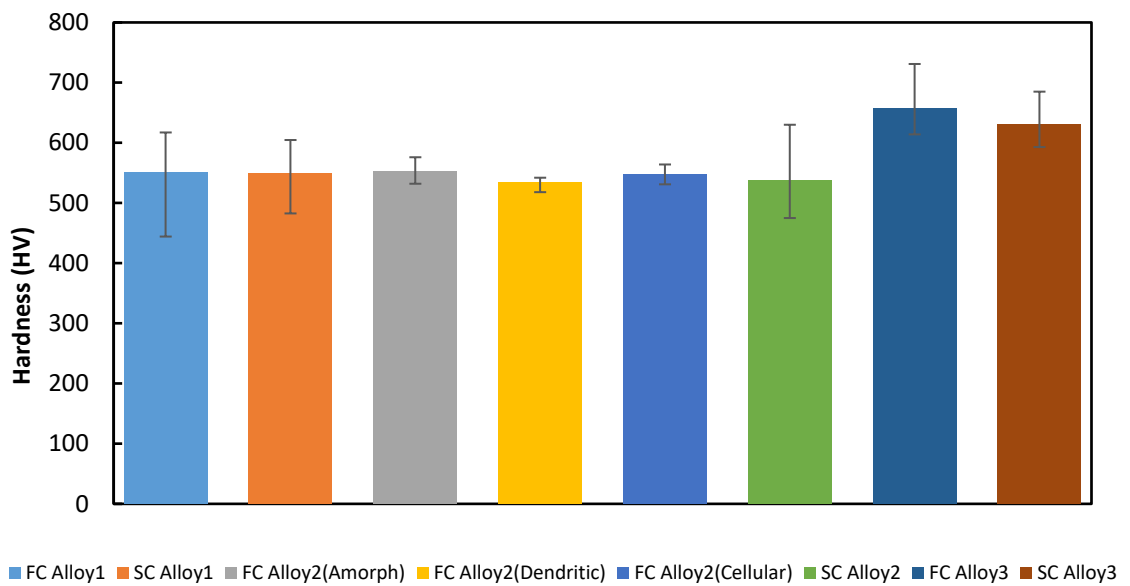


Figure 4.36 Micro-Hardness Comparison of Alloys.

Additionally, microhardness measurements were taken to compare mechanical properties of alloys and their different parts. Hardness values given in Figure 4.36 show negligible differences among Alloy 1 and Alloy 2. On the contrary, Alloy 3

display noticeable hardness increase compared to the other two alloy due to containing hard intermetallics namely Ti_5Si_3 . Hardness values of fast cooling parts are very close to the that of slow cooling parts of the Alloy 1 and Alloy 2. This would suggest that smaller crystalline size of the fast cooling parts of the samples has resulted in the same hardness values as the slow cooling parts of the samples which have intermetallic precipitates. One interesting phenomenon is that amorphous layer of the FC Alloy 2 has very similar hardness value with crystalline region of the sample. This is somewhat desirable feature where amorphous structure illustrate tough attribute.

CHAPTER 5

CONCLUSIONS AND FUTURE SUGGESTIONS

5.1. Conclusions

In this thesis study, BGFA was evaluated experimentally for Ti-based bulk metallic glasses by using previously calculated ΔH_{mix} (enthalpy of mixing) and R_c (critical cooling rate) parameters [99]. In addition to these theoretical computations, empirical rules such as solidification model [29] and deep eutectic rule [30] were used for alloy design. When both theoretical and empirical rules were boiled down to Ti-based binary systems, Cu becomes a promising pair due to having a consecutive peritectic and eutectic reactions that can crystallize into intermetallics for a Ti-Cu composition range. Moreover, Ni, Al, and V elements which increase negative ΔH_{mix} and decrease R_c according to reference [99] were utilized as alloying additions for Ti-Cu binary system and Alloy 1 with the composition $\text{Ti}_{48}\text{Cu}_{30}\text{Ni}_{10}\text{Al}_7\text{V}_5$ was produced and investigated with microstructural, thermal and mechanical analysis methods. To make the crystallization even harder, an element having relatively small atomic size (Si) was added to Alloy 1 as a minor alloying according to the theoretically calculated data. Its effects were investigated by producing alloys with the increasing amount of Si. For this purpose, Alloy 2 $\text{Ti}_{47}\text{Cu}_{30}\text{Ni}_{10}\text{Al}_7\text{V}_5\text{Si}_1$ and Alloy 3 $(\text{Ti}_{48}\text{Cu}_{30}\text{Ni}_{10}\text{Al}_7\text{V}_5)_{97}\text{Si}_3$ were produced and examined. The important points of the experimental studies can be summarized as follows:

- Copper mold suction casting resulted in significant changes in the properties of the Alloy 1 and Alloy 2. Microstructure of samples considerably changed by the copper mold suction casting process. Formation of Ti_2Cu and TiAlCu_2 intermetallic phases are inhibited and intensities of γ -TiCu phase decreased under non-equilibrium rapid cooling conditions for both compositions.

- Minor addition of silicon on Alloy 2 favored formation of approximately 40 μm in thickness amorphous structure at the outer zone of the FC Alloy 2.
- Further addition of Si on Alloy 3 has detrimental effects on glass formation ability. Even at non-equilibrium cooling condition amorphous structure was not observed and the crystallization could not be prevented by copper mold suction casting. Fast cooling part of the Alloy 3 contains the same phases as slow cooling part of the Alloy 3.
- Liquidus temperature of the fast cooling part of the Alloy 1, Alloy 2, and Alloy 3 decreases with the addition of Si, which indicates the higher stability of the metallic liquid after minor Si addition which may lead to amorphous structure formation.

5.2. Future Suggestions

- The other alloying elements were listed in reference [98] which were found to decrease the enthalpy of mixing (Ag, Au, Li, Cd, P, Si, V, Ga, Ge, Al, Hg, Sc and Zn) and decrease the critical cooling rate (Ag, Au, P, Li, Si, Cd, V, Y, Sc, Ge, Hg, Ga, Al, La, Zn, Mg, Mn, Co, Ni, Fe, In, Pt, Cr, Te, Be and Sn) found to be highly similar to the candidate alloying elements determined by theoretical studies in the literature. Therefore, these elements should be examined as other alloying element in the composition Alloy 2 for further increase in the thickness of the amorphous structure.
- Especially Zr and Sn addition together with the Si should be considered due to the good effects on glass forming ability [54].
- Alloy 2 should be reproduced to assess reproducibility of the amorphous structure.

REFERENCES

1. Jun, W.K., R. Willens, and P. Duwez, Non-crystalline structure in solidified gold–silicon alloys. *Nature*, 1960. **187**(4740): p. 869.
2. Chen, H. and D. Turnbull, Formation, stability and structure of palladium-silicon based alloy glasses. *Acta metallurgica*, 1969. **17**(8): p. 1021-1031.
3. Chen, H., Thermodynamic considerations on the formation and stability of metallic glasses. *Acta Metallurgica*, 1974. **22**(12): p. 1505-1511.
4. Lee, M.C., J.M. Kendall, and W.L. Johnson, Spheres of the metallic glass Au₅₅Pb₂₂.₅Sb₂₂.₅ and their surface characteristics. *Applied Physics Letters*, 1982. **40**(5): p. 382-384.
5. Kui, H., A.L. Greer, and D. Turnbull, Formation of bulk metallic glass by fluxing. *Applied Physics Letters*, 1984. **45**(6): p. 615-616.
6. Inoue, A., T. Zhang, and T. Masumoto, Al–La–Ni amorphous alloys with a wide supercooled liquid region. *Materials transactions, JIM*, 1989. **30**(12): p. 965-972.
7. Inoue, A., et al., Mg–Cu–Y amorphous alloys with high mechanical strengths produced by a metallic mold casting method. *Materials transactions, JIM*, 1991. **32**(7): p. 609-616.
8. Zhang, T., A. Inoue, and T. Masumoto, Amorphous Zr–Al–TM (TM= Co, Ni, Cu) alloys with significant supercooled liquid region of over 100 K. *Materials Transactions, JIM*, 1991. **32**(11): p. 1005-1010.
9. Peker, A. and W.L. Johnson, A highly processable metallic glass: Zr₄₁.₂Ti₁₃.₈Cu₁₂.₅Ni₁₀.₀Be₂₂.₅. *Applied Physics Letters*, 1993. **63**(17): p. 2342-2344.
10. Inoue, A., N. Nishiyama, and H. Kimura, Preparation and thermal stability of bulk amorphous Pd₄₀Cu₃₀Ni₁₀P₂₀ alloy cylinder of 72 mm in diameter. *Materials Transactions, JIM*, 1997. **38**(2): p. 179-183.
11. Chen, L., et al., Free-volume-induced enhancement of plasticity in a monolithic bulk metallic glass at room temperature. *Scripta Materialia*, 2008. **59**(1): p. 75-78.
12. Hofmann, D.C., Bulk metallic glasses and their composites: a brief history of diverging fields. *Journal of Materials*, 2013. **2013**.
13. Inoue, A., et al., Cobalt-based bulk glassy alloy with ultrahigh strength and soft magnetic properties. *Nature materials*, 2003. **2**(10): p. 661.
14. Wang, J., et al., Co-based ternary bulk metallic glasses with ultrahigh strength and plasticity. *Journal of Materials Research*, 2011. **26**(16): p. 2072-2079.
15. Inoue, A., Stabilization of metallic supercooled liquid and bulk amorphous alloys. *Acta materialia*, 2000. **48**(1): p. 279-306.
16. Khan, M.M., et al., Recent advancements in bulk metallic glasses and their applications: A review. *Critical Reviews in Solid State and Materials Sciences*, 2018. **43**(3): p. 233-268.
17. Makino, A., A. Inoue, and T. Mizushima, Soft magnetic properties of Fe-based bulk amorphous alloys. *Materials transactions, JIM*, 2000. **41**(11): p. 1471-1477.

18. Inoue, A., T. Zhang, and A. Takeuchi. Ferrous and nonferrous bulk amorphous alloys. in *Materials Science Forum*. 1998. Trans Tech Publ.
19. Nieh, T. and J. Wadsworth, Homogeneous deformation of bulk metallic glasses. *Scripta Materialia*, 2006. **54**(3): p. 387-392.
20. Masumoto, T. and K. Hashimoto, Chemical properties of amorphous metals. *Annual Review of Materials Science*, 1978. **8**(1): p. 215-233.
21. Gebert, A., et al., Corrosion behaviour of Mg₆₅Cu₇. 5Ni₇. 5Ag₅Zn₅Gd₅Y₅ bulk metallic glass in aqueous environments. *Electrochimica Acta*, 2008. **53**(8): p. 3403-3411.
22. Wang, W.-H., C. Dong, and C. Shek, Bulk metallic glasses. *Materials Science and Engineering: R: Reports*, 2004. **44**(2-3): p. 45-89.
23. Gao, Q., et al., Crystallization kinetics of the Cu₅₀Zr₅₀ metallic glass under isothermal conditions. *Journal of Solid State Chemistry*, 2016. **244**: p. 116-119.
24. Zhang, L.-C., Thermodynamic approach for amorphous alloys from binary to multicomponent systems, in *Thermodynamics-Kinetics of Dynamic Systems*. 2011, IntechOpen.
25. Turnbull, D., Under what conditions can a glass be formed? *Contemporary physics*, 1969. **10**(5): p. 473-488.
26. Yu, C., et al., Atomistic approach to predict the glass-forming ability in Zr–Cu–Al ternary metallic glasses. *Journal of Alloys and Compounds*, 2015. **627**: p. 48-53.
27. Cheng, Y. and E. Ma, Atomic-level structure and structure–property relationship in metallic glasses. *Progress in materials science*, 2011. **56**(4): p. 379-473.
28. Takeuchi, A. and A. Inoue, Calculations of mixing enthalpy and mismatch entropy for ternary amorphous alloys. *Materials transactions, JIM*, 2000. **41**(11): p. 1372-1378.
29. Akdeniz, M.V., A.O. Mekhrabov, and M.K. Pehlivanoglu, Solidification behaviour of bulk glass-forming alloy systems. *Journal of alloys and compounds*, 2005. **386**(1-2): p. 185-191.
30. Turnbull, D., A. Structure Information amorphous Solid Formation And Interstitial Solution Behavior In Metallic Alloy Systems. *Le Journal de Physique Colloques*, 1974. **35**(C4): p. C4-1-C4-10.
31. Davies, H. and B. Lewis, A generalised kinetic approach to metallic glass formation. *Scripta Metallurgica*, 1975. **9**(10): p. 1107-1112.
32. Mondal, K. and B. Murty, On the parameters to assess the glass forming ability of liquids. *Journal of non-crystalline solids*, 2005. **351**(16-17): p. 1366-1371.
33. Lu, Z. and C. Liu, A new glass-forming ability criterion for bulk metallic glasses. *Acta materialia*, 2002. **50**(13): p. 3501-3512.
34. Ray, C.S., et al., A new DTA method for measuring critical cooling rate for glass formation. *Journal of non-crystalline solids*, 2005. **351**(16-17): p. 1350-1358.

35. Mattern, N., Structure formation in liquid and amorphous metallic alloys. *Journal of non-crystalline solids*, 2007. **353**(18-21): p. 1723-1731.
36. Tanner, L. and R. Ray, Physical properties of Ti₅₀Be₄₀Zr₁₀ glass. *Scripta Metallurgica*, 1977. **11**(9): p. 783-789.
37. Peker, A. and W.L. Johnson, Beryllium bearing amorphous metallic alloys formed by low cooling rates. 1994, Google Patents.
38. Zhang, T. and A. Inoue, Thermal and mechanical properties of Ti–Ni–Cu–Sn amorphous alloys with a wide supercooled liquid region before crystallization. *Materials transactions, JIM*, 1998. **39**(10): p. 1001-1006.
39. He, G., J. Eckert, and M. Hagiwara, Glass-forming ability and crystallization behavior of Ti–Cu–Ni–Sn–M (M= Zr, Mo, and Ta) metallic glasses. *Journal of applied physics*, 2004. **95**(4): p. 1816-1821.
40. Xie, K.-F., K.-F. Yao, and T.-Y. Huang, A Ti-based bulk glassy alloy with high strength and good glass forming ability. *Intermetallics*, 2010. **18**(10): p. 1837-1841.
41. Wu, X., et al., Bulk metallic glass formation in a ternary Ti–Cu–Ni alloy system. *Journal of Alloys and Compounds*, 2008. **452**(2): p. 268-272.
42. Wang, Y.-L. and J. Xu, Ti (Zr)-Cu-Ni bulk metallic glasses with optimal glass-forming ability and their compressive properties. *Metallurgical and Materials Transactions A*, 2008. **39**(12): p. 2990.
43. Wiest, A., et al., Zr–Ti-based Be-bearing glasses optimized for high thermal stability and thermoplastic formability. *Acta Materialia*, 2008. **56**(11): p. 2625-2630.
44. Nagahama, D., T. Ohkubo, and K. Hono, Crystallization of Ti₃₆Zr₂₄Be₄₀ metallic glass. *Scripta materialia*, 2003. **49**(7): p. 729-734.
45. Kim, Y., W. Kim, and D. Kim, A development of Ti-based bulk metallic glass. *Materials Science and Engineering: A*, 2004. **375**: p. 127-135.
46. Liu, Y., et al., Formation and properties of Ti-based Ti–Zr–Cu–Fe–Sn–Si bulk metallic glasses with different (Ti+ Zr)/Cu ratios for biomedical application. *Intermetallics*, 2016. **72**: p. 36-43.
47. Pang, S., et al., New Ti-based Ti–Cu–Zr–Fe–Sn–Si–Ag bulk metallic glass for biomedical applications. *Journal of Alloys and Compounds*, 2015. **625**: p. 323-327.
48. Liu, Y., et al., TiCuZrFeSnSiSc bulk metallic glasses with good mechanical properties for biomedical applications. *Journal of Alloys and Compounds*, 2016. **679**: p. 341-349.
49. Huang, Y., et al., A new Ti–Zr–Hf–Cu–Ni–Si–Sn bulk amorphous alloy with high glass-forming ability. *Journal of Alloys and Compounds*, 2007. **427**(1-2): p. 171-175.
50. Zhu, S., et al., Glass-forming ability and thermal stability of Ti–Zr–Cu–Pd–Si bulk glassy alloys for biomedical applications. *Materials transactions*, 2007. **48**(2): p. 163-166.
51. Tang, M., et al., TiZr-base bulk metallic glass with over 50 mm in diameter. *Journal of Materials Science & Technology*, 2010. **26**(6): p. 481-486.

52. Zhang, L., et al., Compressive plastic metallic glasses with exceptional glass forming ability in the Ti–Zr–Cu–Fe–Be alloy system. *Journal of Alloys and Compounds*, 2015. **638**: p. 349-355.
53. Zhang, T. and A. Inoue, Preparation of Ti–Cu–Ni–Si–B amorphous alloys with a large supercooled liquid region. *Materials transactions, JIM*, 1999. **40**(4): p. 301-306.
54. Zhang, T. and A. Inoue, Ti-based amorphous alloys with a large supercooled liquid region. *Materials Science and Engineering: A*, 2001. **304**: p. 771-774.
55. Kim, Y., et al., Glass forming ability and crystallization behavior of Ti-based amorphous alloys with high specific strength. *Journal of non-crystalline solids*, 2003. **325**(1-3): p. 242-250.
56. Ma, C., et al., New Ti-based bulk glassy alloys with high glass-forming ability and superior mechanical properties. *Materials transactions*, 2004. **45**(11): p. 3223-3227.
57. Ma, C., et al., Formation of new Ti-based metallic glassy alloys. *Materials transactions*, 2004. **45**(5): p. 1802-1806.
58. Guo, F., et al., Ductile titanium-based glassy alloy ingots. *Applied Physics Letters*, 2005. **86**(9): p. 091907.
59. Men, H., et al., New Ti-based bulk metallic glasses with significant plasticity. *Materials transactions*, 2005. **46**(10): p. 2218-2220.
60. Xia, M.-x., et al., Thermal stability and glass-forming ability of new Ti-based bulk metallic glasses. *Journal of non-crystalline solids*, 2005. **351**(49-51): p. 3747-3751.
61. Xia, M.X., et al., Preparation and crystallization of Ti₅₃Cu₂₇Ni₁₂Zr₃Al₇Si₃B₁ bulk metallic glass with wide supercooled liquid region. *Materials Science and Engineering: A*, 2005. **390**(1-2): p. 372-375.
62. Hao, G., et al., Bulk metallic glass formation of Ti-based alloys from low purity elements. *Materials Letters*, 2006. **60**(9-10): p. 1256-1260.
63. Zhu, S., et al., A new Ti-based bulk glassy alloy with potential for biomedical application. *Materials Science and Engineering: A*, 2007. **459**(1-2): p. 233-237.
64. Huang, Y., J. Shen, and J. Sun, Formation, thermal stability and mechanical properties of Ti 42.5 Zr 7.5 Cu 40 Ni 5 Sn 5 bulk metallic glass. *Science in China Series G: Physics, Mechanics and Astronomy*, 2008. **51**(4): p. 372-378.
65. Jian, L.Y.X., Optimized Compositions Of Ti-(Cu, Ni)-Sn Alloy For Metallic Glass Formation And Their Correlation With Eutectic Reaction. *Acta Metall Sin*, 2008. **44**(12): p. 1424-1430.
66. Zhu, S., X. Wang, and A. Inoue, Glass-forming ability and mechanical properties of Ti-based bulk glassy alloys with large diameters of up to 1 cm. *Intermetallics*, 2008. **16**(8): p. 1031-1035.
67. Hao, G., et al., Ti–Zr–Be ternary bulk metallic glasses correlated with binary eutectic clusters. *Materials Science and Engineering: A*, 2010. **527**(23): p. 6248-6250.

68. Yin, E., et al., Formation of Ti–Zr–Cu–Ni–Sn–Si bulk metallic glasses with good plasticity. *Journal of Alloys and Compounds*, 2010. **504**: p. S10-S13.
69. Zhang, Y., et al., Glass-Forming Ability and Competitive Crystalline Phases for Lightweight Ti–Be–Based Alloys. *Metallurgical and Materials Transactions A*, 2010. **41**(7): p. 1670-1676.
70. Khalifa, H.E. and K.S. Vecchio, Thermal stability and crystallization phenomena of low cost Ti-based bulk metallic glass. *Journal of Non-Crystalline Solids*, 2011. **357**(19-20): p. 3393-3398.
71. Gong, P., K. Yao, and Y. Shao, Effects of Fe addition on glass-forming ability and mechanical properties of Ti–Zr–Be bulk metallic glass. *Journal of Alloys and Compounds*, 2012. **536**: p. 26-29.
72. Gong, P., K. Yao, and Y. Shao, Lightweight Ti–Zr–Be–Al bulk metallic glasses with improved glass-forming ability and compressive plasticity. *Journal of Non-Crystalline Solids*, 2012. **358**(18-19): p. 2620-2625.
73. Gong, P., et al., Centimeter-sized Ti-based bulk metallic glass with high specific strength. *Progress in Natural Science: Materials International*, 2012. **22**(5): p. 401-406.
74. Gong, P., et al., A New Centimeter-Sized Ti-Based Quaternary Bulk Metallic Glass with Good Mechanical Properties. *Advanced Engineering Materials*, 2013. **15**(8): p. 691-696.
75. Gong, P., et al., Ti-Zr-Be-Fe quaternary bulk metallic glasses designed by Fe alloying. *Science China Physics, Mechanics and Astronomy*, 2013. **56**(11): p. 2090-2097.
76. Gong, P., et al., A Ti–Zr–Be–Fe–Cu bulk metallic glass with superior glass-forming ability and high specific strength. *Intermetallics*, 2013. **43**: p. 177-181.
77. Wang, Z., et al., Ti-based glassy alloys in Ti–Cu–Zr–Sn system. *Science China Physics, Mechanics and Astronomy*, 2013. **56**(7): p. 1419-1422.
78. Zhang, L., et al., A Ti₃₆. 2Zr₃₀. 3Cu₈. 3Fe₄Be₂₁. 2 bulk metallic glass with exceptional glass forming ability and remarkable compressive plasticity. *Journal of Alloys and Compounds*, 2013. **562**: p. 205-210.
79. Li, P., et al., Glass forming ability, thermodynamics and mechanical properties of novel Ti–Cu–Ni–Zr–Hf bulk metallic glasses. *Materials & Design*, 2014. **53**: p. 145-151.
80. Zhao, S., et al., A centimeter-sized quaternary Ti-Zr-Be-Ag bulk metallic glass. *Advances in Materials Science and Engineering*, 2014. **2014**.
81. Wang, T., et al., Novel Ti-based bulk metallic glasses with superior plastic yielding strength and corrosion resistance. *Materials Science and Engineering: A*, 2015. **642**: p. 297-303.
82. Zhao, S., et al., Quaternary Ti–Zr–Be–Ni bulk metallic glasses with large glass-forming ability. *Materials & Design*, 2015. **85**: p. 564-573.
83. Zhao, S., et al., Centimeter-Sized Quaternary Ti-Based Bulk Metallic Glasses with High Ti Content of 50 at%. *Advanced Engineering Materials*, 2016. **18**(2): p. 231-235.

84. Gu, J., et al., Centimeter-sized Ti-rich bulk metallic glasses with superior specific strength and corrosion resistance. *Journal of Non-Crystalline Solids*, 2019.
85. Kuball, A., et al., Development and characterization of titanium-based bulk metallic glasses. *Journal of Alloys and Compounds*, 2019.
86. Park, J.M., et al., Ti-based bulk metallic glasses with high specific strength. *Materials Transactions*, 2004. **45**(2): p. 595-598.
87. Park, J., et al., Enhancement of plasticity in Ti-rich Ti–Zr–Be–Cu–Ni bulk metallic glasses. *Scripta Materialia*, 2005. **53**(1): p. 1-6.
88. Park, J., et al., Ductile Ti-based bulk metallic glasses with high specific strength. *Metallurgical and Materials Transactions A*, 2011. **42**(6): p. 1456-1462.
89. Yao, K.-F., Y.-Q. Yang, and N. Chen, Mechanical properties of Pd–Cu–Si bulk metallic glass. *Intermetallics*, 2007. **15**(5-6): p. 639-643.
90. Yang, B., et al., Al-rich bulk metallic glasses with plasticity and ultrahigh specific strength. *Scripta Materialia*, 2009. **61**(4): p. 423-426.
91. Jiang, J.Z., et al., Low-Density High-Strength Bulk Metallic Glasses and Their Composites: A Review. *Advanced Engineering Materials*, 2015. **17**(6): p. 761-780.
92. Li, H. and Y. Zheng, Recent advances in bulk metallic glasses for biomedical applications. *Acta biomaterialia*, 2016. **36**: p. 1-20.
93. Calin, M., et al., Designing biocompatible Ti-based metallic glasses for implant applications. *Materials Science and Engineering: C*, 2013. **33**(2): p. 875-883.
94. Suer, S., Investigations On Bulk Glass Forming Ability Of Titanium Based Multicomponent Alloys. 2008, Middle East Technical University. p. 156.
95. Murray, J.L., Phase diagrams of binary titanium alloys. 1987.
96. Karlsson, N., An x-ray study of the phases in the copper-titanium system. *J Inst Met*, 1951. **79**: p. 391-405.
97. Knowles, K. and D. Smith, The crystallography of the martensitic transformation in equiatomic nickel-titanium. *Acta Metallurgica*, 1981. **29**(1): p. 101-110.
98. Wang, Y.-L., E. Ma, and J. Xu, Bulk metallic glass formation near the TiCu–TiNi pseudo-binary eutectic composition. *Philosophical Magazine Letters*, 2008. **88**(5): p. 319-325.
99. Suer, S., A.O. Mekhrabov, and M.V. Akdeniz, Theoretical prediction of bulk glass forming ability (BGFA) of Ti–Cu based multicomponent alloys. *Journal of Non-Crystalline Solids*, 2009. **355**(6): p. 373-378.
100. Takeuchi, A. and A. Inoue, Classification of bulk metallic glasses by atomic size difference, heat of mixing and period of constituent elements and its application to characterization of the main alloying element. *Materials Transactions*, 2005. **46**(12): p. 2817-2829.

101. Al-Cu-Ti (Aluminium - Copper - Titanium), in Light Metal Systems. Part 2: Selected Systems from Al-Cu-Fe to Al-Fe-Ti, G. Effenberg and S. Ilyenko, Editors. 2005, Springer Berlin Heidelberg: Berlin, Heidelberg. p. 1-18.
102. Cu-Si-Ti (Copper - Silicon - Titanium), in Light Metal Systems. Part 4: Selected Systems from Al-Si-Ti to Ni-Si-Ti, G. Effenberg and S. Ilyenko, Editors. 2006, Springer Berlin Heidelberg: Berlin, Heidelberg. p. 1-15.
103. Ghosh, G., Ternary Alloy Systems: Phase Diagrams, Crystallographic and Thermodynamic Data critically evaluated by MSIT: Non-ferrous metal systems, Vol. C Part 3, G. Effenberg and S. Ilyenko, eds. 2007, Springer.

